

UNIVERSITY OF OKLAHOMA

GRADUATE COLLEGE

FISCHER-TROPSCH SYNTHESIS ON CARBON NANOTUBE-SUPPORTED
CATALYSTS IN WATER-IN-OIL EMULSION

A DISSERTATION

SUBMITTED TO THE GRADUATE FACULTY

in partial fulfillment of the requirements for the

Degree of

DOCTOR OF PHILOSOPHY

By

DACHUAN SHI
Norman, Oklahoma

FISCHER-TROPSCH SYNTHESIS ON CARBON NANOTUBE-SUPPORTED
CATALYSTS IN WATER-IN-OIL EMULSION

A DISSERTATION APPROVED FOR THE
SCHOOL OF CHEMICAL, BIOLOGICAL AND MATERIALS ENGINEERING

BY

Dr. Daniel E. Resasco, Chair

Dr. Richard G. Mallinson

Dr. Lance L. Lobban

Dr. Steven P. Crossley

Dr. Daniel T. Glatzhofer

© Copyright by DACHUAN SHI 2013
All Rights Reserved.

To my parents, Meng Shi and Qinghua Sun. Your wholehearted love and support to me have made possible my journey to becoming a PhD and a better person.

To the loving memory of my grandma, my best childhood friend. Every now and then your heartwarming smile comes to me and I know you have never left.

Acknowledgements

I would like to thank my advisor, Dr. Daniel E. Resasco. The spectacular view of the catalysis world has unfolded in front of me with his inspiration. He has mentored me not only on specific projects but also on being a better researcher and thinker. It is my great privilege to be his student. I am grateful to have Dr. Mallinson, Dr. Lobban, Dr. Crossley and Dr. Glatzhofer in my committee, who have given me valuable advices and suggestions that I've learned and benefited a lot from. I appreciate Dr. Friederike Jentoft, Dr. Schmidtke, Dr. Johnson and Dr. McCann for letting me use their instruments that greatly extended the span of my projects. Dr. Rolf Jentoft has helped tremendously on instrumentation that was indispensable to my research. Special thanks go to Dr. Silvy, Dr. Tan, David Arthur at SouthWest Nanotechnologies, Inc. for generously donating nanohybrid materials and providing technical supports, as well as my wonderful learning experience from the internship. The department staff has been patiently assisting me on a daily basis, which helped me to concentrate more on research. Greg and Preston at the Samuel Roberts Noble Microscopy Laboratory of OU have been very helpful on electron microscopy characterizations and instructions. I've learned, and obtained a lot of help from my senior and current coworkers of the group. Working and discussing with them have greatly extended my technical knowledge and cultural perspectives. It's been my great fortune to have Tu's company and there are so many reasons for me to appreciate her. Finally, this work wouldn't be possible without the financial support from the funding agencies, including NSF/EPSCOR, DOE/EPSCOR, DOE/Basic Energy Sciences and Oklahoma State Regents for Higher Education.

Table of Contents

Acknowledgements	iv
List of Tables	viii
List of Figures.....	ix
Abstract.....	xvii
1. Fischer–Tropsch synthesis using carbon nanotube-supported catalysts at the water/oil interface in an emulsion system	1
1.1 Introduction	1
1.1.1 Fischer-Tropsch synthesis	1
1.1.2 Carbon nanotubes as catalyst support.....	10
1.1.3 Research objectives	12
1.2 Experimental.....	13
1.3 Results and Discussion	17
1.3.1 Stabilization of emulsions by catalytic nanohybrids	17
1.3.2 Fischer Tropsch Synthesis (FTS) in the emulsion system.....	18
1.4 Summary.....	33
2. Liquid-phase Fischer-Tropsch synthesis: the rationale behind the choice of catalyst supports toward better productivity and selectivity.....	35
2.1 Introduction	35
2.1.1 Water effects in FTS.....	35
2.1.2 Research objectives	39
2.2 Experimental.....	41
2.3 Results and Discussion	42

2.4 Summary.....	64
3. Synthesis of single-walled carbon nanotubes on planar supports and their applications	66
3.1 Introduction	66
3.1.1 Synthesis, catalysts and growth mechanisms of carbon nanotubes.....	66
3.1.2 Applications of carbon nanotubes	71
3.1.3 Objectives of this study	75
3.2 Experimental.....	83
3.2.1 Surface-guided growth of horizontally aligned SWCNTs on quartz	83
3.2.2 Growth of conductive SWCNT films with ultra-high transparency	84
3.2.3 Synthesis of graphene.....	85
3.2.4 Fabrication of thin film transistors and device measurements	85
3.3 Results and discussion.....	86
3.3.1 Surface-guided growth of horizontally aligned SWCNTs on quartz	86
3.3.2 Growth of conductive SWCNT films with ultra-high transparency	96
3.3.3 Graphene synthesized on copper foils.....	108
3.3.4 Application of the synthesized SWCNT films and graphene in FETs....	108
3.4 Summary.....	115
4. Conclusions and future directions	117
5. References	120
Appendix A: Pd nanoclusters dispersed onto pristine and functionalized single-wall carbon nanotubes as a partial justification for the use of carbon nanotubes as catalyst supports.	141

Appendix B. The use of activated carbon as catalyst support in aqueous-phase ketonization of acetic acid	152
Appendix C. Calculation and fitting in Chapter 1	155
Appendix D. Kinetic fitting of FTS in water and emulsion phases.....	158
Appendix E. GC chromatographs.....	160
Appendix F. Optoelectronic performance of CNT films reported in the literature	162
Appendix G. References for Appendix	163

List of Tables

Table 1 Major reactions in FTS process	3
Table 2 Characteristics of common FTS catalysts (from F. Morales, B.M. Weckhuysen, J. Catal. 19 (2006) 1).	4
Table 3 Selectivity variation by process and catalyst conditions (from M. Roper, in Catalysis in C1 Chemistry (W. Keim, ed.), Reidel, Dordrecht, 1983).....	8
Table 4 Characteristics of the two catalysts investigated	14
Table 5 Conversions and chain growth probability (α) values in some FTS reactions in this study.....	26
Table 6 Partition of pyridine and its derivatives in decalin and water phase after reaction (Syngas ratio = 4, reaction time = 12 h)	29
Table 7 Mass transfer parameters of H_2S and NH_3 in decalin and water phase.	32
Table 8 C1-C4 hydrocarbon fractions at low conversions	49
Table 9 Data of 2-h FTS reactions with different catalyst pretreatments.....	52
Table 10 σ_{op}/σ_{dc} values of the samples from this study.....	106
Table 11 Optoelectronic performance of films reported in the literature.....	107
Table 12 Characteristics of the SWCNT-TFT and graphene-TFT.....	111

List of Figures

- Figure 1** FTS product distribution predicted by ASF model. 9
- Figure 2** TEM images of Pd nanoclusters dispersed on functionalized (a) and pristine SWCNTs (b). The corresponding SWCNTs before Pd deposition are shown as reference in (c) and (d), respectively; Raman spectra of pristine (dashed black line) and functionalized (red solid line) SWCNTs (e); Raman spectrum of pristine MWCNTs (f). 11
- Figure 3** Process flow diagram employed to simulate the separation and reaction process during the conversion of bio-syngas via Fischer-Tropsch in a water-decalin biphasic system. The thermodynamic methods employed for the distribution of the species in the flash and liquid-liquid separator were NRTL and UNIFAC, respectively. 16
- Figure 4** (a) Optical microscopy image of an emulsion formed by stirring a 1:1 mixture of decalin and water in the presence of Ru/CNT nanohybrid, (b) optical image of the emulsion system, (c) TEM image of Catalyst #1 (prepared without a reduction step) and (d) Catalyst #2 (prepared with a reduction step). 18
- Figure 5** Representative sections of GC chromatographs for products in decalin phase obtained with syngas ratio (H_2/CO) of 1.2 over a 6-h reaction (a) and with syngas ratio of 3.5 over a 12-h reaction (b). 19
- Figure 6** Weight distribution of hydrocarbon products obtained with Catalyst #1: (a) overall and (c) liquid phase, with dotted line denotes fittings by ASF distribution equation; and Catalyst #2: (b) overall and (d) liquid phase. Reactions were carried out with $H_2/CO = 3.5$ at 200°C over 12 h. 21
- Figure 7** Representative section of GC chromatograph for products at shorter run. ... 21

Figure 8 Whole-range GC chromatographs for FTS products obtained in emulsion-run (a) and in decalin-run (b). Dichloromethane was used as external standard. Catalyst #2 was used for both runs. Syngas ratio was 4 and reaction time was 12 h.	23
Figure 9 (a) Liquid phase product yields at different H ₂ /CO ratios. (b) Representative sections of GC chromatographs for products in decalin and water phase obtained with syngas ratio = 5.4 over reaction time of 12 h.	24
Figure 10 Weight distribution of hydrocarbon products obtained on Catalyst #2 with and without HCl. (a,b) overall; (c,d) liquid phase. Syngas ratio = 4, reaction time = 12 h.	28
Figure 11 Representative sections of GC chromatographs for products in decalin (a) and water phase (b) from reaction in the presence of HCl.	28
Figure 12 Representative sections of GC chromatographs for products from the run of decalin single-phase without pyridine (a), decalin single-phase with pyridine (b) and emulsion phase with pyridine (c).	29
Figure 13 Distribution of hydrogen sulfide (left) and ammonia (right) in the three phases (organic, aqueous and gas phase) at 150 °C (a,d), 200 °C (c,e), and 250 °C (b,f).	31
Figure 14 Partition of H ₂ S between organic and aqueous phases at different reaction conditions.	31
Figure 15 CO conversions with syngas ratio of 4 over 12 h in an oil/water mixture (1:1 ratio) using carbon nanotubes (CNTs) and nanohybrid as supports.	33
Figure 16 (A) DFT-derived energy diagram for vacancy generation and direct CO* activation on (111) terraces of Ru ₂₀₁ (1.55 ML CO*). The apparent activation energy	

(ΔE_{app}) for the direct path is a sum of the energy required to generate a vacancy $(-\Delta H_1)$ from a CO^* -covered surface (a) and the intrinsic activation energy (ΔE_6) for direct activation of CO^* by a surface vacancy (b) to form chemisorbed C^* and O^* species (c). (B) DFT-calculated energy diagram for H-assisted CO^* activation path on the (111) terrace of Ru_{201} (1.55 ML CO^*). The apparent activation energy for the H^* -assisted path is a sum of the energy required to generate a vacancy $(-\Delta H_1)$ from a CO^* -covered surface (a), the enthalpy of H_2 adsorption $(\Delta H_2; (b) \text{ to } (c))$, the enthalpy of H^* addition to CO^* $(\Delta H_3; (c) \text{ to } (d))$, and the activation barrier for H^* addition to HCO^* $(\Delta E_4, (d) \text{ to } (e))$. The barrier for the dissociation reaction of $HCOH^*$ to $CH^* + OH^*$ $((e) \text{ to } (f))$ is shown to justify the irreversibility of HCO^* hydrogenation.

Transition-state energies are denoted by double daggers (from Reference 40). 38

Figure 17 CO consumption rate, selectivity to CH_4 , and selectivity to C_{5+} products as a function of the average H_2O partial pressure on a 5 wt% Ru/SiO_2 catalyst. (Open symbols) Space velocity runs; (Closed symbols) H_2O -addition runs (from Reference 39). 39

Figure 18 Evolution of TOF and methanation as a function of initial amount of liquid water added into decalin, keeping a total of 30 mL of solvent(s). Data obtained with syngas ratio of 2 at a low conversion of below 20% over 2 h reaction time..... 43

Figure 19 Turnover frequency of nanohybrid-supported catalyst in different solvents over four reaction cycles, each cycle being 2 h. Between cycles, the reactor was cooled down to room temperature, gas phase was sampled and released from the reactor vessel, then fresh syngas was introduced to the vessel to the initial pressure of 600 psi. 45

Figure 20 Alkane/alkene/alcohol fraction for C ₆ , C ₁₂ and C ₁₈ products in decalin (a), emulsion (b) and water (c) at a conversion ≈ 65%.	46
Figure 21 GC chromatographs of products from FTS with nanohybrid-supported catalyst in emulsion phase at a conversion of 64.7% before hydrogenation (a), after hydrogenation (b) and at a conversion of 91.0% without hydrogenation (c).	47
Figure 22 Product distribution at a conversion ≈ 65% in decalin, water and emulsion (Syngas ratio = 3.5, 150 mg catalyst, reaction temperature = 200°C).	48
Figure 23 Product distribution at different conversions in emulsion (a) and water single-phase (b); Gas phase hydrocarbon fraction vs. conversion with different catalysts in different solvents (c) (Syngas ratio = 3.5, 150 mg catalyst, reaction temperature = 200°C).	51
Figure 24 CO conversion vs. reaction time in emulsion and water phase, with each data point from a separate run (a), and CO conversion rate vs. conversion in emulsion and water phase, analytically obtained from the plot of CO conversion vs. reaction time (b).	51
Figure 25 Evolution of catalyst TOF during recycle tests and after 6-h reaction (Syngas ratio = 3.5, 100 mg catalyst for recycle tests, and 150 mg catalyst for 6 h-2 h test, reaction temperature = 200°C).	53
Figure 26 TEM images of fresh Ru catalyst (a), spent catalyst in emulsion for 8 h (b) and spent catalyst in water for 8 h (c). (Syngas ratio = 3.5, 150 mg catalyst for 8 h reaction at 200°C. Scale bar is 10 nm).	56
Figure 27 Hydrogenolysis test in emulsion (a) and water single-phase (b) using dodecane as the probe compound. Insets: schematics of the extraction of hydrocarbon	

<i>products in emulsion (a), and formation of hydrocarbon film coating on catalyst particles in water single-phase (b).</i>	57
Figure 28 <i>TEM images of Ru supported on nanohybrid (a), activated carbon (b) and silica (c) and optical images of the corresponding support in decalin/water mixture. Scale bar is 10 nm.</i>	58
Figure 29 <i>(a) A typical calculated Ru particle, with an average diameter of 2.9 nm. Atoms that belong to active B₅ sites are shown in red. (b) Density of active sites as a function of particle diameter, as calculated through analysis of the atomistic Wulff construction (adapted from Reference 164).</i>	61
Figure 30 <i>TOF of Ru catalysts on different supports in different solvents.</i>	62
Figure 31 <i>Conversions of FTS with three catalysts in different solvents at 2 h and 8 h reaction time.</i>	62
Figure 32 <i>Alkane, alkene and alcohol fractions of C₆, C₁₂ and C₁₈ products with silica-supported catalyst in water single-phase at a conversion of 80.2%: before (a) and after (b)hydrogenation, and with silica-supported catalyst in decalin single-phase at a conversion of 33.5% before hydrogenation (c).</i>	63
Figure 33 <i>Horizontal CVD system used in our group.</i>	68
Figure 34 <i>Radom networks (a) and aligned CNT arrays (b) obtained via CVD method in this research. Inset: interaction energy profiles between CNTs and substrates, adapted from Reference 165.</i>	69
Figure 35 <i>SEM of graphene obtained by CVD growth in this research.</i>	71
Figure 36 <i>(A) Wrapping a graphene sheet into a CNT. The wrapping and the resulting nanotube are characterized by the chirality vector $C = na_1 + ma_2 \equiv (n,m)$, where a_1 and</i>	

a_2 are the unit vectors of the hexagonal lattice. In the example shown here, point B is brought over point A, resulting in a tube with a circumference $C = 5a_1 + 2a_2$. (B) Top: Band-structure of graphene. Bottom: The first Brillouin zone of graphene. (Adapted from Reference 238). 72

Figure 37 Optical image of a transparent, conductive SWCNT film on a sapphire substrate (a), and optical image of an array of ‘‘all-tube’’ flexible transparent thin film transistors (TTFTs) on a plastic substrate, with arrow indicating the S/D structures(b). (Adapted from Reference 1)..... 74

Figure 38 Schematic structure of a top-gated CNTFET (left) and output electrical characteristics of a top-gated CNTFET (right). (Adapted from Reference 238). 75

Figure 39 SEM images of HA-SWCNTs grown with pure ethanol (A and B) and AFM image (C); corresponding images with 1% of water mixed with ethanol in the bubbler (D, E and F)..... 87

Figure 40 SEM images of HA-SWCNTs grown with bubbler with ethanol mixed with 1% of water, showing high density. 88

Figure 41 SEM and AFM images showing the hockey stick termination of tube growth. 88

Figure 42 SEM images of HA-SWCNTs grown with pure ethanol (A) and the zoom-in view of the center part (C); with ethanol and 1% of water (B) and the zoom-in view of the center part (D). 90

Figure 43 SEM images of HA-SWCNTs grown with ethanol and 3% of water (A); with ethanol and 5% of water (B). 90

Figure 44 SEM images of samples grown with ethanol and 3% of water (A) and the zoom in view (C); re-grown with ethanol and 1% of water (B) and the zoom-in view (D).....	94
Figure 45 SEM images of samples after water injection for 5 min.	95
Figure 46 Optical photo showing quartz substrates without (left) and with a SWCNT film (right). The black dot on the bottom left corner of the right substrate was used as a marker for the side with the film.....	96
Figure 47 SEM images of the SWCNT film at magnifications of x15 000 (A), x50 000 (B) and x100 000 (C).....	97
Figure 48 Raman spectrum of the SWCNT showing the D and G band.	98
Figure 49 Sheet resistance and transmittance (at 550 nm) as a function of anneal time.	99
Figure 50 SEM images of SWCNT films obtained with annealing time of 0 min (A), 10 min (B), 20 min (C), 30 min (D), 45 min (E) and 60 min (F).	101
Figure 51 Higher-magnification SEM images of SWCNT films obtained with annealing time of 20 min (A), 30 min (B), 45 min (C) and 60 min (D).	102
Figure 52 Sheet resistance and transmittance (at 550 nm) as a function of ferritin concentration and their corresponding SEM images. The samples were annealed for 60 min and reaction lasted for 30 min.....	104
Figure 53 Transmittance vs. sheet resistance in this study and literature.	107
Figure 54 SEM images of graphen synthesized on copper foils.	108
Figure 55 Raman spectrum of the synthesized graphene.	108

Figure 56 (a) Schematic of the fabrication procedure: spin coating PMMA onto source substrate, transferring PMMA/SWCNT layer onto target substrate with pre-printed source and drain, printing gate electrode on top of PMMA. (b) optical image taken by the camera of the printer showing source (S), drain (D), gate (G) and PMMA layer. The length of the image corresponds to ~ 1.6 mm. (c) a complete three-transistor array device on PET substrate. 109

Figure 57 SEM images of SWCNT film transferred to polyimide (a) and glass (b) 109

Figure 58 Plot of resistance versus channel length for calculating the specific contact resistance of (a) electrode-graphene and (b) electrode-SWCNT film. Insets show schematics of electrodes used for this measurements. 110

Figure 59 Electrical measurements of the SWCNT TFT device. (a) I_{ds}/V_{ds} characteristics at various V_g . (b) transfer characteristics of the device, inset: SEM image of the SWCNT film on source substrate. (c) I_{ds}/V_{ds} characteristics of a SWCNT TFT device reported in Reference 204. 110

Figure 60 Electrical measurements of the graphene TFT device. (a) I_{ds}/V_{ds} characteristics at various V_g . (b) transfer characteristics of the device. Inset: SEM image of the graphene on source substrate. (c) I_{ds}/V_{ds} characteristics of a graphene TFT device reported in Reference 111

Figure 61 Electrical measurements of a SWCNT TFT on a glass slide. (a) I_{ds}/V_{ds} characteristics at various V_g . (b) transfer characteristics of the device. (c) a complete three-transistor array device. 114

Abstract

Fischer-Tropsch synthesis (FTS) is an important gas-to-liquids technology in the modern energy industry. The current trend is to carry it out in liquid reaction media in order to take advantage of good heat transfer, high catalyst efficiency, convenience for catalyst regeneration/reloading and lower costs, due to either the use of liquid media or the associated reactor designs. Adding water vapor to FTS has been proven to promote the reaction in many catalyst systems, but there was no attempt prior to this point to add liquid water in organic media. The choice of catalyst supports would be critical from multiple perspectives. First of all, the co-existence of both water and oil necessitates a support that could maximize the liquid interface for better mass transfer as well as dispersion of the catalyst. The product-support interaction is another important issue, especially for FTS product in liquid phase where secondary reaction happens when primary products re-adsorb onto catalysts. And finally, as with any catalyst, the metal-support interaction greatly affects the catalyst particle sizes and reactivity.

We chose Ru catalyst supported on a multi-walled carbon nanotube/MgO-Al₂O₃ hybrid as the catalyst support for biphasic FTS, and carried out systematic studies that rationalized the choice of the support in terms of catalyst activity, deactivation, production selectivity as well as product separation. As it turned out, the amphiphilic properties of the nanohybrid-supported catalyst and the thus formed emulsion system were among the essential factors in the successful implement of the concept. A comprehensive interpretation of the results and a comparative investigation with some other catalyst supports have revealed the importance of choosing the right catalyst

support, as well as given a better understanding of the FTS mechanism that incorporates recent progress reported in literature.

We then went on to study the synthesis of carbon nanotubes (CNTs) in the effort to find optimal conditions for their production. In addition, sharing similarities in mechanistic pathways in a broad sense, but with much heavier molecular weight, CNTs have stronger interaction with catalyst supports than FTS products and were therefore a more typical model to study and demonstrate the product-support interaction as well. On the planar substrate support, depending on the isotropy/anisotropy of the CNT-support interaction, either random networks or aligned arrays of CNT films were synthesized on the corresponding support. Here another important continuation from the study of FTS was the promoting effects of water. We've concluded that water facilitates CNT growth in the second step, i.e., the step where monomeric C units condense into CNTs, while in the case of FTS, water plays a role mostly in the first step of CO dissociating into the monomeric CH species. Finally, a novel method to fabricate devices of the CNT films were presented that tested the merits of using planar supports for CNT growth in actual applications.

1. Fischer–Tropsch synthesis using carbon nanotube-supported catalysts at the water/oil interface in an emulsion system

1.1 Introduction

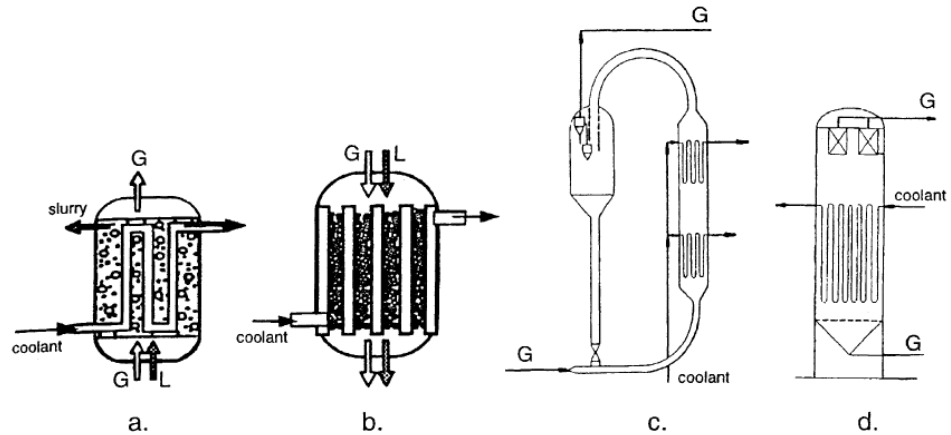
1.1.1 Fischer-Tropsch synthesis

1.1.1.1 Fischer-Tropsch synthesis process

Fischer-Tropsch synthesis (FTS), a long established gas-to-liquids technology where hydrogenation of carbon monoxide produces products of predominately aliphatic straight-chain hydrocarbons, has been gaining ever-growing interests both scientifically and commercially in recent decades. There are two major driving forces behind this renewed attention. The first is the exploration for alternatives to conventional oil production, since crude oil reserves world-wide are finite and it is only a matter of time for their extinction. The second driving force is the increasing concern about environment. In comparison to conventionally produced oil, FT oil contains very little aromatics and no sulfur. Its fuel range products have higher cetane numbers and therefore lead to lower emissions. The feed gas of H₂ and CO (so called “syngas”) is from gasification of coal, steam reforming of natural gas, or gasification of biomass.

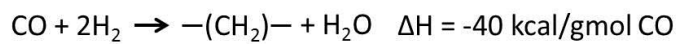
Commercial FTS is performed in three major reactor types: fluidized-bed, fixed-bed and slurry bubble columns, with the latter two involving organic solvents as reaction media [1]. Multiphase reactors involving gas (syngas), liquid (reaction media and products) and solid (catalysts) are considered most promising [2]. For example, slurry bubble columns have the advantages of good heat transfer, high catalyst efficiency, convenience for catalyst reloading/regeneration and low costs [3,4]. Sasol uses slurry bubble column reactors for the production of middle distillates in the C₁₀-C₂₀

range [5], while Shell uses multi tubular fixed bed reactors for this process [6]. Improvement on liquid medium-based FTS is thus practically and industrially appealing.



Schematic 1 Reactors for commercial FTS: Slurry bubble column reactor (a), multi-tubular trickle bed and circulating reactor (fixed-bed, b and c) and fluidized-bed reactor (d) (Adapted from Reference 1).

FTS is a highly exothermic polymerization process [7,8]:



with a number of reactions as summarized in Table 1.

Table 1 Major reactions in FTS process

Main reactions	
Alkanes	$n\text{CO} + (2n + 1)\text{H}_2 \rightarrow \text{C}_n\text{H}_{2n+2} + n\text{H}_2\text{O}$
Alkenes	$n\text{CO} + 2n\text{H}_2 \rightarrow \text{C}_n\text{H}_{2n} + n\text{H}_2\text{O}$
Alcohols	$n\text{CO} + 2n\text{H}_2 \rightarrow \text{C}_n\text{H}_{2n+1}\text{OH} + (n - 1)\text{H}_2\text{O}$
Side reactions	
Water-gas shift	$\text{CO} + \text{H}_2\text{O} \leftrightarrow \text{CO}_2 + \text{H}_2$
Boudouard reaction	$\text{CO} + \text{CO} \rightarrow \text{C} + \text{CO}_2$
Carbonaceous species	$\left(x + \left(\frac{y}{2}\right)\right)\text{H}_2 + x\text{CO} \rightarrow \text{C}_x\text{H}_y + x\text{H}_2\text{O}$
Bulk carbide	$y\text{C} + x\text{M} \leftrightarrow \text{M}_x\text{C}_y$
Hydrogenolysis (Demethylation)	$\text{C}_n\text{H}_{2n+2} + \text{H}_2 \leftrightarrow \text{C}_{n-1}\text{H}_{2n} + \text{CH}_4$

Typical synthesis conditions are temperatures in the range of 200-300°C and pressures of 10-60 bar [8]. Group VIII metals, especially Ru, Fe, Ni and Co (in the order of decreasing activity), are the most common catalysts. Co catalysts have the advantages of giving the highest yields, longest lifetime and producing predominately linear alkanes, and are usually designed for heavy products [9-11]. This is attributed to the strong alkene re-adsorption on Co [12,13]. In addition, Co is not subject to inhibition by water and therefore exhibits higher productivity at a higher syngas conversion [14]. Fe has high WGS activity and selectivity to alkenes [15]. It is used together with alkali and/or Cu. The former acts to enhance activity by increasing the electron density in Fe to increase CO adsorption [16,17], and the latter helps the reduction of Fe [18]. Different from other FTS catalysts, the active species of Fe-based catalysts are not only pure metal. The identified forms include metallic iron (α -Fe), iron oxides (hematite, α -Fe₂O₃; magnetite Fe₃O₄, and Fe_xO), and five different forms of iron

carbides, O-carbides (carbides with carbon atoms in octahedral interstices, ϵ -Fe₂C, ϵ -Fe_{2.2}C, and Fe_xC), and TP carbides (carbides with carbon atoms in trigonal prismatic interstices, χ -Fe_{2.5}C and Fe₃C) [19-22]. Ru is the most active [23] and gives the highest molecular weight products [24] without any promoters. Thus it is a catalyst of high scientific value in exploring the fundamentals of FTS, and it has been spurring increasing interest for its potential of producing clean FTS bio-fuels [25-33]. In addition, Ru has shown high resistance against oxidation of water, which is a concomitant product of FTS [34].

Table 2 Characteristics of common FTS catalysts (from F. Morales, B.M. Weckhuysen, *J. Catal.* 19 (2006) 1).

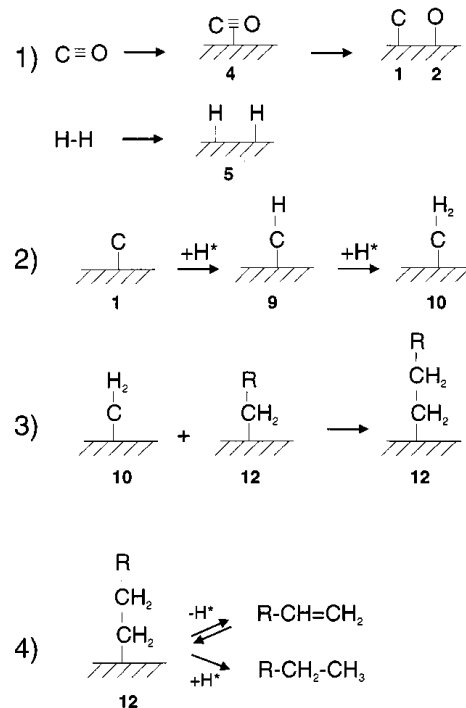
<i>Active metal</i>	<i>Price</i>	<i>FT activity</i>	<i>WGS activity</i>	<i>Hydrogenation activity</i>
Ni	++++	+	+/-	+++++
Fe	+	+	+++	+
Co	+++	+++	+/-	+++
Ru	+++++	+++++	+/-	+++

1.1.1.2 Reaction mechanism

Many mechanisms have been proposed over the years but the complex nature of FTS makes it difficult to reach to an explicit conclusion. Following is a brief introduction of some major mechanisms.

Carbide mechanism

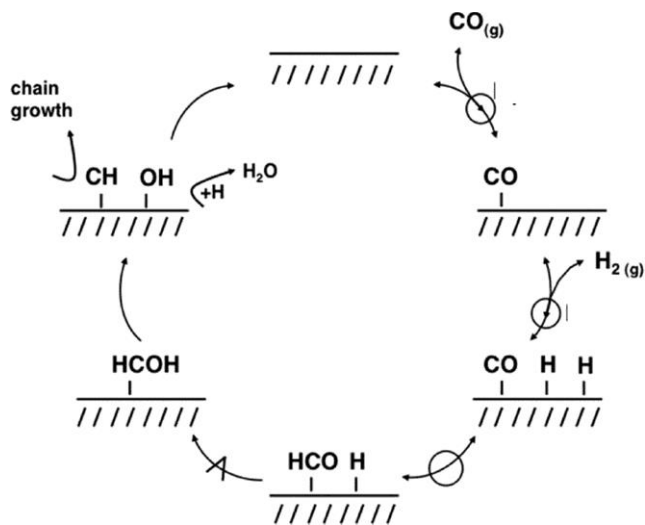
The most adopted mechanism is surface carbide mechanism by CH₂ insertion [18,35,36]. It assumes dissociative adsorption of CO and H₂ on catalyst surface to form CH₂ (along with CH and CH₃) as the building block, which couples to each other to propagate to long hydrocarbon chains. Termination happens via addition of hydrogen or CH₃ to form alkanes, hydrogen abstraction to form alkenes, or with oxygen containing surface species to form alcohols [37].



Schematic 2 FTS via surface carbide mechanism (adapted from A.T. Bell, *Catal. Rev.—Sci. Eng.* 23 (1981)203 and B. Sarup, B.W. Wojciechowski, *Can. J. Chem. Eng.* 67 (1989) 62).

Enolic mechanism

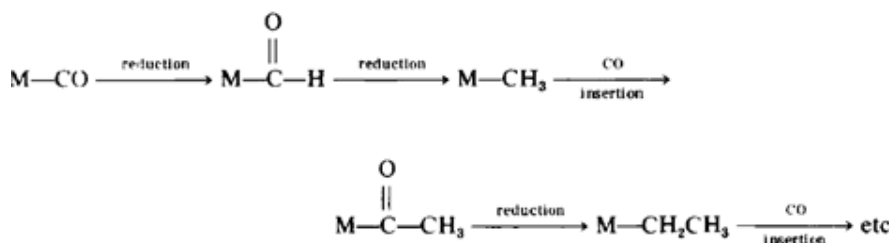
Another important mechanism is hydrogen-assisted CO dissociation (enolic mechanism) [17,36,38], in which hydrogen reacts with non-dissociatively adsorbed CO to form an enolic (HCOH) species, which then couples with each other and hydrogen to remove oxygen in the form of water to form CH₂ species for chain propagation, with similar termination steps as in the carbide mechanism. This mechanism has been gaining more attention as recent theoretical work has provided further support. Iglesia et al. showed that the energy barrier for hydrogen-assisted CO dissociation is much lower than that for direct CO dissociation, and therefore it is the predominant path for CO dissociation [39,40].



Schematic 3 Elementary steps of H^{*}- assisted CO^{*} activation on Ru surface. Quasi-equilibrated steps are denoted by reaction arrows overlaid with a circle; the kinetically-relevant step is denoted with a reaction arrow overlaid with a carrot symbol. (adapted from Reference 40).

CO insertion mechanism

In this mechanism, metal-CO bond is reduced to aldehyde, which is further reduced to form metal-CH₃. At this point CO insertion takes place as shown in Schematic 4.



Schematic 4 CO insertion mechanism (adapted from C. Masters, *Adv. Organomet. Chem.* 17 (1979) 61).

1.1.1.3 Product selectivity

The process conditions exert strong influence on the product selectivity. Increase in temperature leads to higher selectivity toward products of lower carbon number [18]. Increase in total pressure or CO/H₂ ratio results in heavier products, while the former gives more oxygenates and the latter gives higher alkene content [18,41,42]. With increase in space velocity (decrease in conversion), increase in alkene/alkane ratio [43-45] and decrease in average molecular weight were observed [45]. Selectivity variation by process and catalyst conditions is listed in Table 3.

Table 3 Selectivity variation by process and catalyst conditions (from M. Roper, in *Catalysis in C1 Chemistry* (W. Keim, ed.), Reidel, Dordrecht, 1983)

Parameter	Chain length	Chain branching	Olefin selectivity	Alcohol selectivity	Carbon deposition	Methane selectivity
Temperature	↓	↑	*	↓	↑	↑
Pressure	↑	↓	*	↑	*	↓
H ₂ /CO	↓	↑	↓	↓	↓	↑
Conversion	*	*	↓	↓	↑	↑
Space velocity	*	*	↑	↑	*	↓
Alkali content iron catalyst	↑	↓	↑	↑	↑	↓

Note: Increase with increasing parameter: ↑. Decrease with increasing parameter: ↓. Complex relation: *.

In spite of the complexity of the process and sensitivity to reaction conditions, FTS product distribution shows strong regularities and can be essentially described by Anderson-Schulz-Flory (ASF) equation [46], where m_n is the mole fraction of the product with chain length of n :

$$m_n = (1 - \alpha) \alpha^{n-1}$$

It can also be expressed in terms of weight fraction w_n :

$$w_n = n(1 - \alpha)^2 \alpha^{n-1}$$

α in the above equations is considered independent of n . It is the chain growth probability and calculated by the following equation:

$$\alpha = \frac{R_p}{R_p + R_t}$$

where R_p and R_t are the rates of propagation and termination, respectively. Typical ranges of α on Ru, Co and Fe are 0.85 – 0.95, 0.70 – 0.80 and 0.50 – 0.70, respectively.

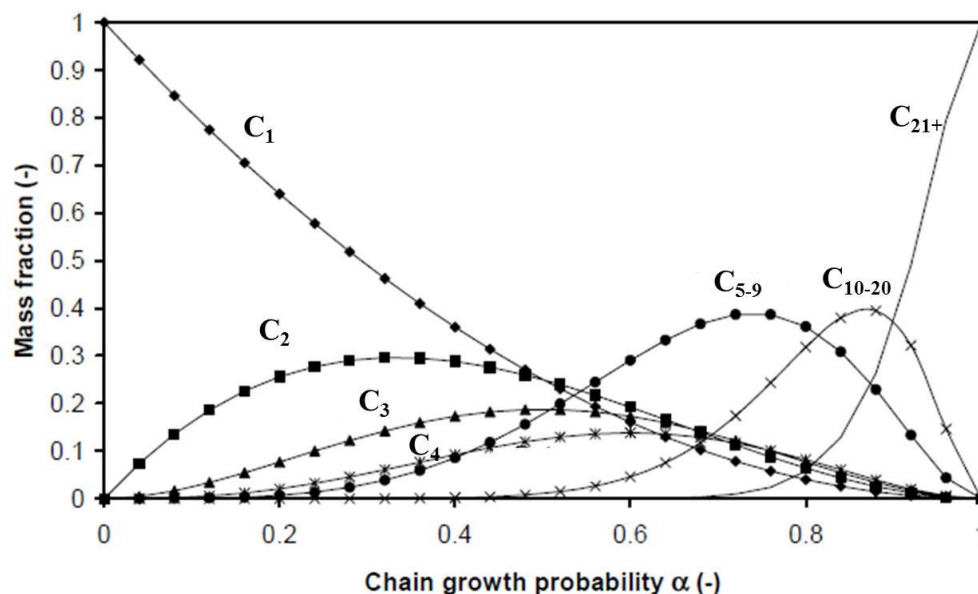


Figure 1 FTS product distribution predicted by ASF model.

However, significant deviations from ASF distribution are a common observation, and there are several causes. One cause is the relatively high methane yield in comparison to the rest of the products, and it can be attributed to high termination probability of C_1 precursors [47], a different site for methanation [48], heat- and mass-transfer limitations [49], or hydrogenolysis (demethylation) [50]. Another reason responsible for the deviation is secondary reactions, including reinsertion, hydrogenolysis and isomerization [44,51-53]. Although secondary hydrogenation was also considered to contribute to the deviation [54], our own study showed that this is not the case. A third reason is changes in chain growth probability (α) with respect to carbon number (n). Three effects were proposed to cause the changes: 1) n -dependent diffusion limitations [45,55,56], 2) n -dependent solubility in heavy FTS products [44,52,57,58], and 3) n -dependent physisorption strength [44,50,52].

1.1.1.4 Catalyst deactivation

Several causes can lead to catalyst deactivation, and they strongly depend on the catalyst. For Co, sintering, carbon deposition and surface reconstruction [59] have been identified. Fe- and Co-based catalysts are subject to water-induced oxidation [60]. Ru, as mentioned above, has demonstrated high resistance against oxidizing environment under FTS conditions. It has been found, however, that volatile Ru-carbonyl species could form and cause loss of catalyst during FTS [61], or lead to larger aggregates [62]. Formation and deposition of inactive species on catalyst surface is an important deactivation mechanism, which leads to blocking of active sites and hindrance to CO chemisorption [60,63-65]. On Ru, carbon deposition, carbidic carbon as well as alkyl chains have been recognized [66-68].

1.1.2 Carbon nanotubes as catalyst support

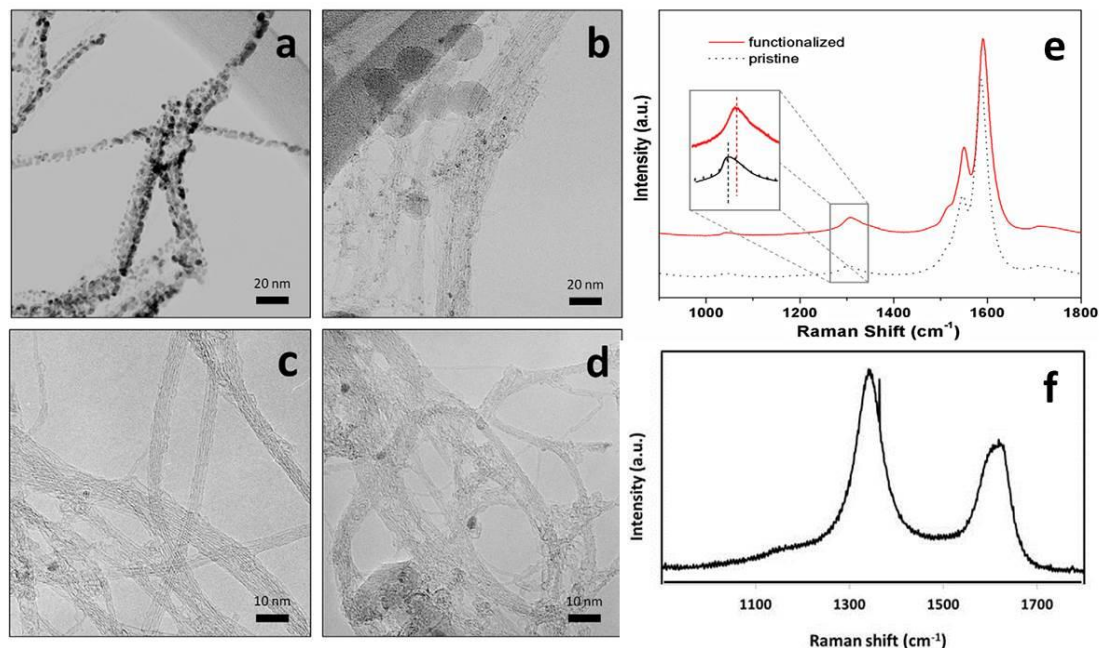
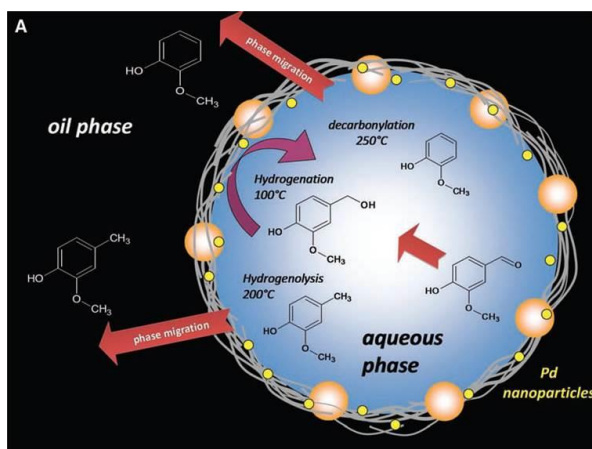


Figure 2 TEM images of Pd nanoclusters dispersed on functionalized (a) and pristine SWCNTs (b). The corresponding SWCNTs before Pd deposition are shown as reference in (c) and (d), respectively; Raman spectra of pristine (dashed black line) and functionalized (red solid line) SWCNTs (e); Raman spectrum of pristine MWCNTs (f).

With high surface area, chemical inertness and good mechanical strength, carbon nanomaterials have demonstrated to be excellent catalyst supports in FTS [69] as well as in other reactions [70-73]. For single-walled carbon nanotubes (SWCNTs), we have shown that their ability to anchor catalyst particles can be further enhanced by creating defects on the nanotube walls, which lead to a stronger metal-support interaction [74]. Multi-walled carbon nanotubes, even at their pristine (without any treatment) state, possess much more defects and functional groups such as $-\text{COOH}$ and $-\text{OH}$, as evidenced by the much stronger D-band of their Raman spectrum [75]. Therefore they have a stronger effect on the electronic structures of metal catalyst and are an even better choice as catalyst support for their outstanding metal particle

dispersing and stabilizing capabilities [76]. Furthermore, carbon nanotubes have been proposed to increase catalyst activity probably due to H₂ adsorption and spillover effects [77]. Our group has recently reported a novel reaction system [78] in which metal-doped carbon nanotube-inorganic oxide hybrids simultaneously stabilize emulsion due to their amphiphilic nature and catalyze reactions at water/oil interface.



Schematic 5 Reactions at water/oil interface in an emulsion system using metal-on-nanohybrid catalyst. Depending on the reaction temperature, the prevailing reactions are hydrogenation, hydrogenolysis, or decarbonylation, and depending on the relative solubilities, the products remain in the aqueous phase or migrate to the oil phase. (adapted from Reference 78).

1.1.3 Research objectives

Here, we explored the application of the emulsion reaction system in FTS, in which both water and decalin are present as the reaction media. A Ru catalyst supported on multi-walled carbon nanotube/MgO-Al₂O₃ hybrid was used as catalyst. Hydrocarbon and short alcoholic products spontaneously separated into decalin and water phase, respectively, fulfilling the initial objective of product separation. Much higher CO

conversion rates than decalin single-phase reactions, along with other intriguing observations in products were analyzed and multiple benefits of emulsion phase FTS were assigned and further envisioned. To investigate and extend its multi-phase based potential advantage, FTS reactions were conducted in the presence of hydrochloric acid pyridine, respectively, which did not affect the activity severely as could be expected in a typical FTS process with such common bio-syngas impurities. Relevant calculations were carried out for additional theoretical support. The preliminary results indicate higher impurity tolerance in emulsion phase FTS, and imply great potential for industrial applications.

1.2 Experimental

Ru on CNT hybrid was prepared via incipient wetness impregnation method. Ruthenium (III) chloride hydrate (99.98%, Sigma-Aldrich), used as the metal precursor, was dissolved in water and impregnated drop-wise onto a determined amount of CNT hybrid (~70wt% carbon nanotubes and balance of MgO-Al₂O₃ support [79], kindly donated by Southwest Nanotechnologies Inc). The sample was then dried for approximately 12 h in a vacuum oven at 80°C and subsequently annealed in flowing He at 400°C for 3 h, followed by calcination at 200°C in a conventional furnace for 2 h and another He annealing session for 5 h. In an alternative method, the first annealing step was replaced by reduction in a H₂/He (10% H₂) flow. The two catalysts are denoted as Catalyst #1 and Catalyst #2, respectively. Their surface areas were determined by BET (Micromeritics, ASAP 2000) and Ru loadings by inductively coupled plasma (ICP, Galbraith Laboratories), along with the mean particle sizes based on transmission

electron microscope (TEM, JEOL 2000-FX). The FTS reaction was performed in a 100-mL stainless steel autoclave batch reactor from Parr Instruments. In a typical experiment, 200 mg of catalyst, 15 mL decalin (mixture of cis + trans, anhydrous, \geq 99% purity, Sigma-Aldrich) and an equal volume of water (HPLC grade, Fischer Scientific), which would emulsify upon stirring, were added to the reactor vessel. The reactor was sealed, purged and pressurized with H₂ to 400 psi for a reduction period of 12 h at 250°C. After reduction, the reactor was cooled to room temperature and purged with H₂ again. Finally, H₂ and CO were introduced at the desired ratio until a total pressure of 600 psi was reached. The actual composition was determined by thermal conductivity on a GC/TCD (Carle 400 AGC). The reaction was conducted at 200°C for 12 h at a constant stirring rate of 700 rpm. Same as the reduction step, the vessel was a closed and isolated system during the reaction. Conversion was monitored at different times by the pressure change observed during the reaction. The gas phase products were measured on the GC/TCD, while the liquid phase products were analyzed after filtration using gas chromatography mass spectrometer (GCMS-QP2010S, Shimadzu) and GC (Agilent 6890). Two immiscible layers of clear liquid were obtained after filtration and were analyzed separately.

Table 4 Characteristics of the two catalysts investigated

Catalyst	Distinctive post-impregnation step	Mean size	Surface area (m ² /g)	Ru loading
#1	Annealed in He	4 nm	268.4	3.7%
#2	Reduced in H ₂ /He	1.5 nm	260.6	3.5%

Calculation of the distribution of the H_2S and NH_3 between water and decalin phases was conducted in the emulsion reaction system at reaction temperatures and pressures that vary from 150 to 250°C and 600 to 1200 psi, respectively. These estimations were performed in ASPEN Plus employing as feedstock a bio-syngas composition similar to that reported in the Biomass Gasification Technology Assessment published by NREL in 2012 [80]. The process flow diagram utilized to simulate the emulsion reaction process is depicted in Figure 3. Here, the bio-syngas is fed in combination with make-up H_2 to achieve a ratio of 2:1 (H_2 :CO) in the feed stream of the FT reactor. In addition, water and decalin were fed to the FT reactor in order to simulate the operation condition of the emulsion reactor. The products of the FT reaction and the unreacted fraction of the feedstock are then separated in a flash that is at the same operating conditions employed in the FT reactor. This process unit was simulated using a NRTL thermodynamic method. In this way we can obtain the fraction of H_2S and NH_3 that would leave the reactor as vapors in the real operation. Then, the liquid fractions are sent to a liquid-liquid separator where the organic phase is separated from the aqueous phase at the same pressure and temperature used in the FT reactor. This enables us to determine the fraction of the impurities that would partition in each one of the phases inside the emulsion FT reactor. In this case, the partition was calculated using the UNIFAC thermodynamic method.

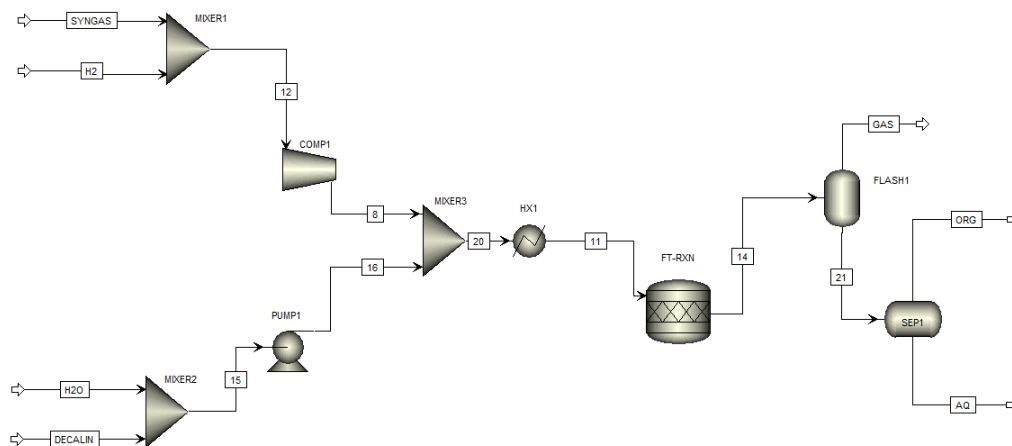


Figure 3 Process flow diagram employed to simulate the separation and reaction process during the conversion of bio-syngas via Fischer-Tropsch in a water-decalin biphasic system. The thermodynamic methods employed for the distribution of the species in the flash and liquid-liquid separator were NRTL and UNIFAC, respectively.

Mass transport calculations were performed to determine the rates of transport of H_2S and NH_3 in the aqueous phase and organic phase (i.e. decalin). The mass transport coefficients and mass transport rates were calculated in using the Fick's Law and the Frössling equation, respectively. The molecular diffusivity estimated employing the Chang et al. correlation at 1200 psi and 250 psi. The viscosity of the cis-decalin and water was determined using the correlation published by Lucas at high pressure and low temperature (1200 psi and 298K) and then extrapolated to higher temperatures (523 K) employing the approximation of Lewis-Squires, which is based on the empirical fact that the sensitivity of viscosity to temperature variations appears to depend primarily upon the value of the viscosity. The density at low temperature was estimated using the Rackett equation. The initial concentrations of the H_2S and NH_3 were assumed to be equal to the equilibrium concentrations obtained in the simulations performed in ASPEN plus.

1.3 Results and Discussion

1.3.1 Stabilization of emulsions by catalytic nanohybrids

Fig. 4a shows an optical microscopy image of the emulsion formed upon stirring the mixture mentioned in the experimental part. The microscopy image shows droplet sizes in the range of 1 to 10 μm . An optical image of the mixture is displayed in Fig. 4b, in which the dark top part consists of water-in-oil emulsion [81] with oil as the continuous phase, while the clear bottom part is the free aqueous phase. In previous studies of our group, the emulsion was prepared by ultrasound sonication, which resulted in very stable emulsions that remained almost unaltered for more than 10 days [78,81]. Without ultrasound sonication, the emulsion can be sustained under constant stirring, but when left standing, the droplets collapse as denoted by the emergence and gradual enlargement of a clear top oil phase and gradual enlargement of the bottom water phase. This situation is desirable in easily breaking the emulsion, separating the products from the different phases, and recovering the catalyst. It should be noted that, despite the elevated temperatures during reduction and reaction, majority of the water present inside the vessel was in liquid form.

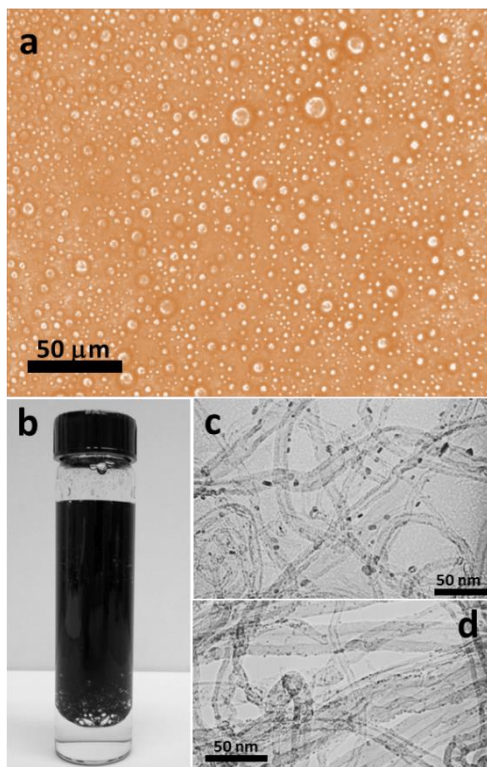


Figure 4 (a) Optical microscopy image of an emulsion formed by stirring a 1:1 mixture of decalin and water in the presence of Ru/CNT nanohybrid, (b) optical image of the emulsion system, (c) TEM image of Catalyst #1 (prepared without a reduction step) and (d) Catalyst #2 (prepared with a reduction step).

Fig. 4c and d show TEM images of the catalytic nanohybrids used in this system. Catalyst #1 (Fig. 4c), which contained Ru particles with a size range of 2 to 6 nm uniformly deposited onto carbon nanotubes, was used for most of the catalytic experiments described below, unless specified otherwise. Catalyst #2 (Fig. 4d) had smaller and more uniform particles (1 to 2 nm range).

1.3.2 Fischer Tropsch Synthesis (FTS) in the emulsion system

When a low H_2/CO ratio of 1.2, which is close to bio-syngas composition [82,83], was used, a complex variety of products, consisting of alkanes, alkenes, and long-chain alcohols, were obtained (Fig. 5a), with CO conversion of 38.1% over 6 h.

Therefore, to saturate hydrocarbon products and simplify analysis, a high H_2/CO ratio of 3.5 was adopted (Fig. 5b). After an FTS period of 12 h, the total pressure decreased from 600 to 290 psi (both measured at room temperature). Liquid products were found to be predominantly alkanes that partitioned in decalin. A small amount of isopropanol, the only oxygenated product, was detected in water phase.

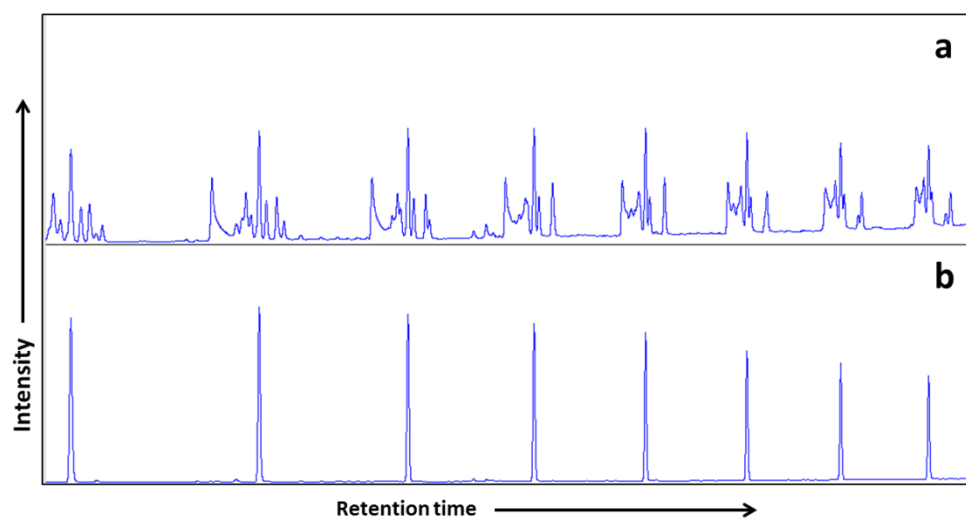


Figure 5 Representative sections of GC chromatographs for products in decalin phase obtained with syngas ratio (H_2/CO) of 1.2 over a 6-h reaction (a) and with syngas ratio of 3.5 over a 12-h reaction (b).

The hydrocarbon product distribution is summarized in Fig. 6a and 6c. It can be seen that the liquid hydrocarbons follow a trend that highly resembles Anderson-Schulz-Flory (ASF) distribution typical of FTS products [84]. Fitting with the ASF equation (Fig. 6c) resulted in a chain growth probability of 84%, which is typical of Ru catalysts [49]. It should be noted that, at shorter reaction time (lower conversion), products (mainly alkenes) other than alkanes were also obtained, indicating that part of the alkane products at high conversions were from re-insertion and secondary

hydrogenation of alkenes. Liquid hydrocarbons represent more than 80 wt% of the total hydrocarbon products. Gas products consisted of mainly methane and negligible amount of C₂-C₄ fraction due to the relatively high H₂/CO ratio and reaction temperature [85]. Gas phase analysis also indicated that only 3% of the initial CO was converted to CO₂ via water-gas shift (WGS) reaction in spite of the presence of extensive amounts of water. At the end of the 12 h run, the CO conversion was determined to be 96%. The initial CO conversion rate was determined to be 28.1 mol CO (mol Ru)⁻¹h⁻¹, which corresponds to a turn over frequency (TOF) of 0.0282 s⁻¹, assuming a Ru dispersion based on TEM observations of 0.33. These values are in the upper range among those reported for Ru catalysts [86-88]. Catalyst #2, with much smaller and uniform particles (1 to 2 nm), had much higher activity of 73.9 mol(mol Ru)⁻¹h⁻¹ with a corresponding initial TOF of 0.0149 s⁻¹. This dispersion-dependent difference in TOF agrees well with studies on both Ru [89] and Co [90] catalysts and is ascribed to large domain or fraction of sites present on planar surfaces needed for high FTS activity. As will be discussed in Chapter 2, we proposed a new explanation for the particle size effect on catalyst activity that takes into account a recently developed FTS catalytic model. The product distributions (overall and liquid products) were similar to those obtained on the first catalyst as summarized in Fig 6b and 6d, respectively.

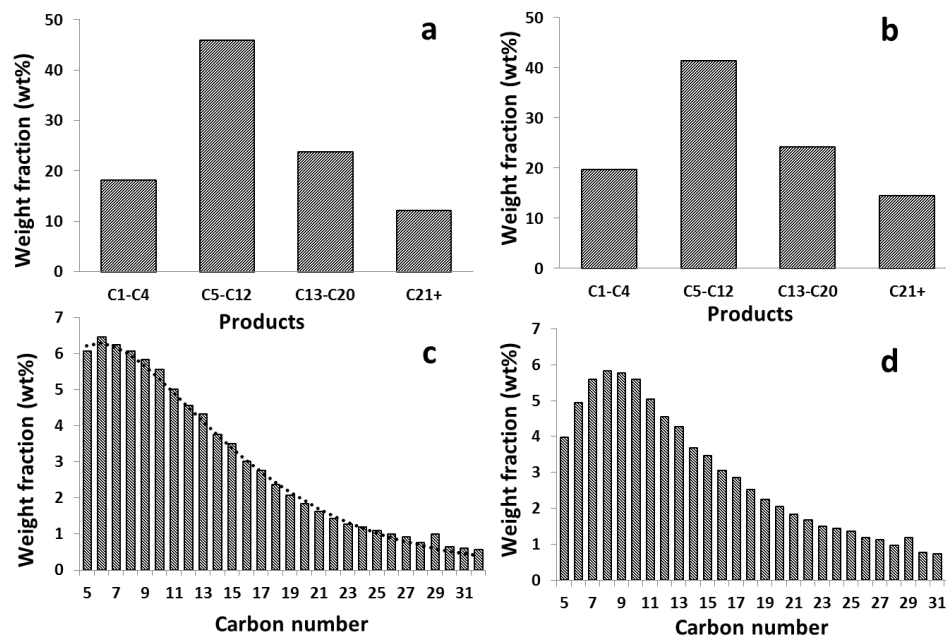


Figure 6 Weight distribution of hydrocarbon products obtained with Catalyst #1: (a) overall and (c) liquid phase, with dotted line denotes fittings by ASF distribution equation; and Catalyst #2: (b) overall and (d) liquid phase. Reactions were carried out with $H_2/CO = 3.5$ at 200°C over 12 h.

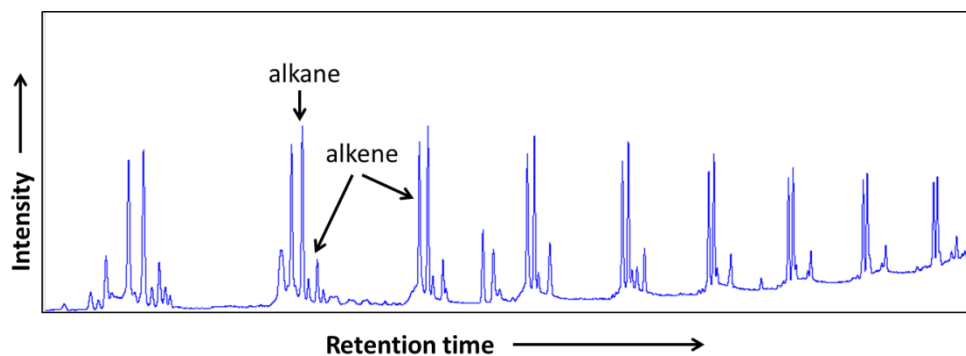


Figure 7 Representative section of GC chromatograph for products at shorter run.

Decalin single phase reaction was conducted under otherwise exactly the same conditions. In comparison to emulsion run, CO conversion was drastically lower, only 34.1%, with almost no hydrocarbon products larger than C_{10} . The results agree well with FTS studies on adding small amounts of water vapor in syngas, which generally

showed enhanced conversion rates and higher products selectivity towards longer chain hydrocarbons [91-93]. Various mechanisms regarding water effects have been proposed, including assisted intra-particle transport of syngas and hydrocarbons [94], and assisted transport of hydrogen [39]. In our case, in addition to the “intrinsic” promotion effects of water, advantages unique to emulsions are expected to further contribute to the pronounced improvement over oil single phase FTS. The formation of small droplets of water-in-oil dramatically increases particle dispersion and interfacial surface areas between the organic and aqueous phases. This results in improved contact between catalysts and reactants, and much better mass transport between the two phases. As a result, as produced molecules can be continuously removed from the reacting emulsion phase to other phases based on their differences in solubility (see results below) [78]. Besides easy product collection, this feature of spontaneous product migration could help to create “clean” catalyst surfaces. This could not only drive the FTS reaction equilibrium forward, but also keep the catalyst from fast deactivation.

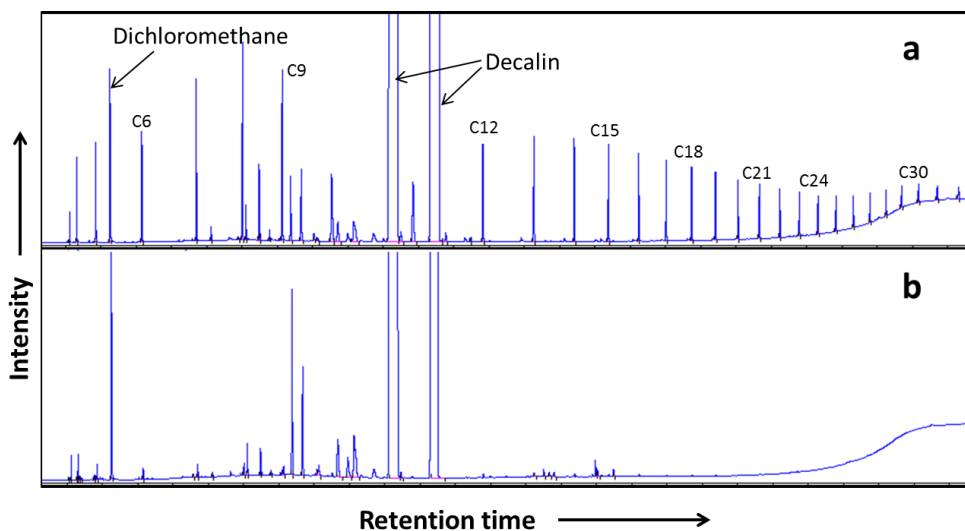


Figure 8 Whole-range GC chromatographs for FTS products obtained in emulsion-run (a) and in decalin-run (b). Dichloromethane was used as external standard. Catalyst #2 was used for both runs. Syngas ratio was 4 and reaction time was 12 h.

The production of short alcohols was found to increase as the syngas composition deviated from the H_2/CO ratio of 4 (Fig. 9a). These results can be used to illustrate the reaction/separation advantages of this system. Representative sections of GC chromatographs of decalin and water phase from the reaction with a syngas ratio of 5.4 are presented in Fig. 9b. As demonstrated, alcohol and hydrocarbon products were collected in the respective phases in which they were soluble, without any detectable crossover to the other phase. Longer alcohols would partition more into the oil phase, but current commercial interest exists towards the $C_1 - C_4$ alcohol range from FTS [95], and can be conveniently separated and collected in the aqueous phase. Besides alkanes, alkenes and alcohols as target products, a variety of undesirable products, including aldehydes, ketones, acids, esters and carbon, are typically obtained in industrial FTS. These products are known to deactivate the catalysts and foul and/or etch the system. The oil/emulsion/water structure is an effective system to deal with this issue.

Undesirable water-soluble products could migrate into the aqueous phase, leaving the reaction zone in the middle emulsion phase less affected and thus less severe catalyst deactivation.

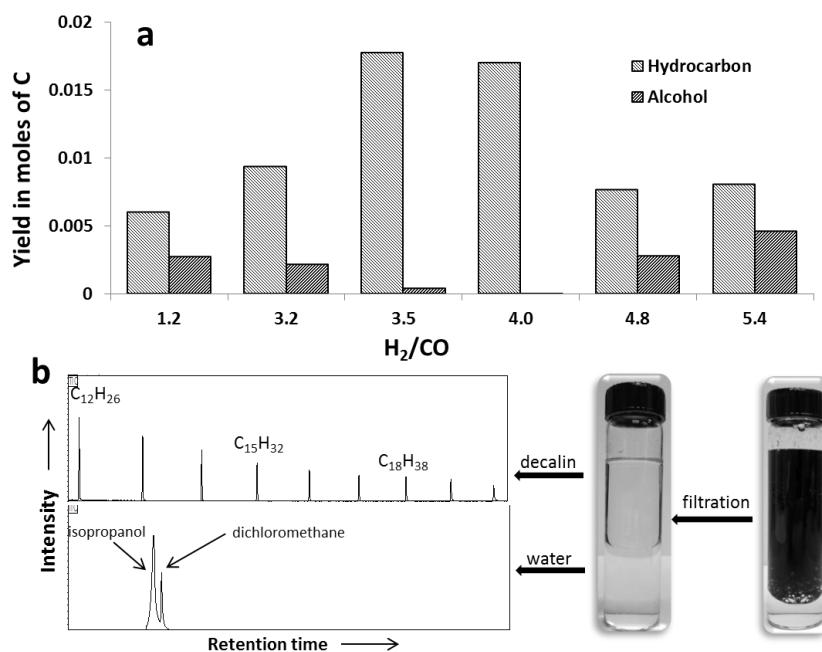


Figure 9 (a) Liquid phase product yields at different H₂/CO ratios. (b) Representative sections of GC chromatographs for products in decalin and water phase obtained with syngas ratio = 5.4 over reaction time of 12 h.

The changes in product composition, or relative alcohol yield, with changing H₂/CO ratio is an interesting aspect. It can be rationalized by taking into account the presence of water in our case, and general rules and patterns of primary FTS products. Considering that isopropanol was the only alcohol in the water phase, and the abundance of water in the reaction, isopropanol was likely the product of hydration-dehydration equilibrium with propene [96,97], rather than that of FTS, which would

result in a range of primary alcohols [13]. At the low H₂/CO ratio side (below 4), alkene yield decreased as the ratio increased [41,42], leading to decreasing alcohol yield; at the high H₂/CO ratio side (above 4), increasing ratio led to higher CO conversion rates (see the discussion below) and thus higher local water production rates on the catalyst surface, which pushed hydration forward and thus increased alcohol yield. In all cases, the as-produced isopropanol migrated to water phase. Thus the equilibrium largely favored its production. Longer alcohols from hydration of heavier alkenes would not be favored, since they tend to migrate to oil phase where dehydration would more likely happen. Ethene hydration to ethanol was not favored either, since it would involve a primary carbonium ion as an intermediate, which is much less stable than a secondary carbonium ion as in the case of propene hydration. While the explanations are subject to extensive experimental examination for further verification which is beyond the scope of this paper, this result may imply the possibility of better alcohol (and/or other products) selectivity with emulsion system. The conversions and chain growth probability (α) values are listed in Table 5 for these reactions, except for the α value for the run with H₂/CO ratio of 1.2 which gave a large variety of products and made quantification rather complex as mentioned earlier. It is generally observed that CO consumption rates are proportional to H₂ pressures, and proportional to CO pressures only below certain values (threshold), beyond which the latter have no effects on rates [98-100]. The conversion values at different H₂/CO ratios reflect the combined effects of both pressures. In all the cases, reactions started with much higher CO pressures than the threshold (e.g., ~50 psi [101]). So H₂ pressure was the only “rate determining

pressure”. Thus at relatively low H₂/CO ratios of 1.2 and 3.2, reactions were slow and low conversions were obtained.

Table 5 Conversions and chain growth probability (α) values in some FTS reactions in this study

H ₂ /CO ratio	1.2*	3.2	3.5	4.0	4.8	5.4	3.5**
Conversion	38.1%	58.5%	96.0%	96.1%	93.4%	90.9%	87.8%
α value	N/A	80.0%	84.3%	84.2%	81.2%	81.2%	86.6%

* 6 h reaction

** 6 h reaction, with Catalyst #2

An important conceptual point must be raised here. It is well known that the driving force that determines chemical reaction and diffusion rates is given by thermodynamic properties, such as chemical affinity, chemical potential or activity. Only in ideal reaction mixtures is it possible to express the reaction rates as a function of the concentration of the species present in the system [102]. Specifically, in the case of a reactant or catalyst poison with low solubility in one of the phases, this concept plays a very important role. Boudart et al. [103] noted that when a component distributed in more than one phase reaches thermodynamic equilibrium, its chemical potential is the same in both phases. Therefore, the presence of a catalyst poison in one phase should affect equally the catalyst regardless the phase in which this is present. However, the chemical potential of a given component may remain low in a phase with low solubility when the rate of mass transfer in that phase is so low that the phases are not in thermodynamic equilibrium.

Actual syngas often contains other components besides H_2 and CO . The inorganic impurities include HCl , H_2S , COS , NH_3 , etc., which are catalyst poisons. Despite a multistep and integrated approach that is usually involved in syngas conditioning [104], impurities are only eliminated down to a certain level due to economic considerations and technological limitations. With higher solubility in water and more restricted mass transfer in oil of these impurities (see discussion below), and confined location of the catalyst due to the hydrophobicity of the supporting carbon nanotubes, it is possible to further lower the impact of the trace amounts of poisons to catalyst activity in emulsion phase FTS. To test this concept, we performed FTS in the emulsion system in the presence of HCl in one case and pyridine in another, which may be taken as representative compounds of acid and N-containing tar impurities, respectively, both of which are known to poison FTS catalysts [83]. For the HCl run, 5mL of 0.012M hydrochloric acid was fed into the catalyst/10mL water/15mL decalin mixture in the reactor through a syringe after the reactor was cooled down from the reduction step. A mixture of 5mL water and 0.5mL pyridine was injected to the same catalyst/water/decalin mixture above in the case of pyridine run. Then the reactor was pressurized to 600 psi with syngas of $H_2/CO = 4$ and brought to the reaction temperature. The amounts of HCl and pyridine added to the system corresponded to composition ranges of actual syngas from biomass gasification [83].

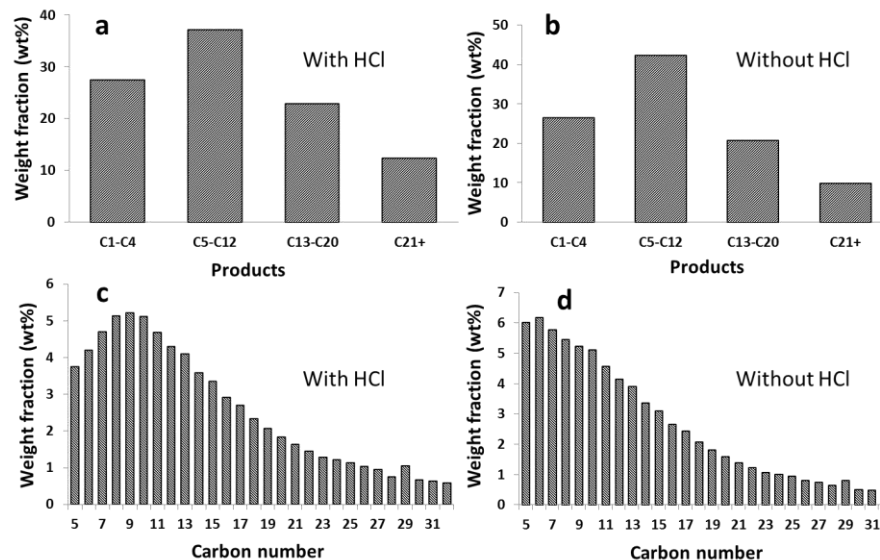


Figure 10 Weight distribution of hydrocarbon products obtained on Catalyst #2 with and without HCl. (a,b) overall; (c,d) liquid phase. Syngas ratio = 4, reaction time = 12 h.

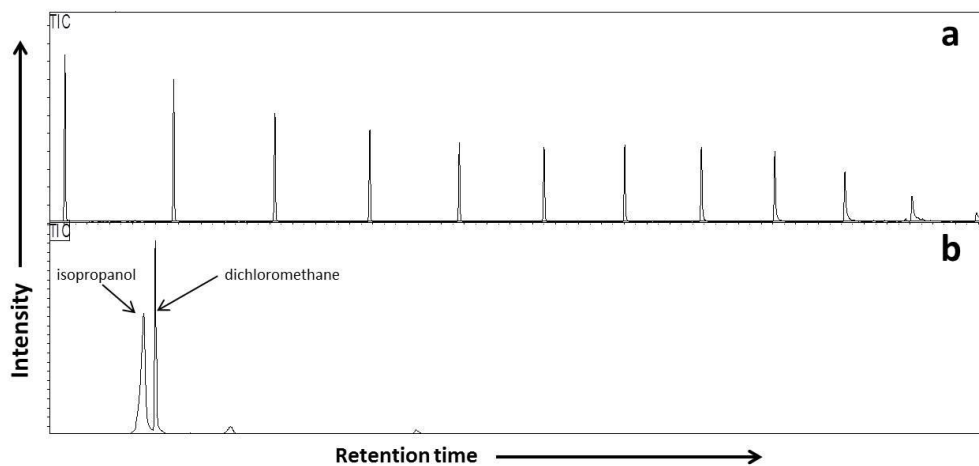


Figure 11 Representative sections of GC chromatographs for products in decalin (a) and water phase (b) from reaction in the presence of HCl.

Table 6 Partition of pyridine and its derivatives in decalin and water phase after reaction (Syngas ratio = 4, reaction time = 12 h)

Compound	Partition (mol%)	
	Decalin	Water
Pyridine	0.83	4.99
Piperidine	3.73	81.35
Alkylated piperidine	9.10	0
Total in each phase	13.66	86.34

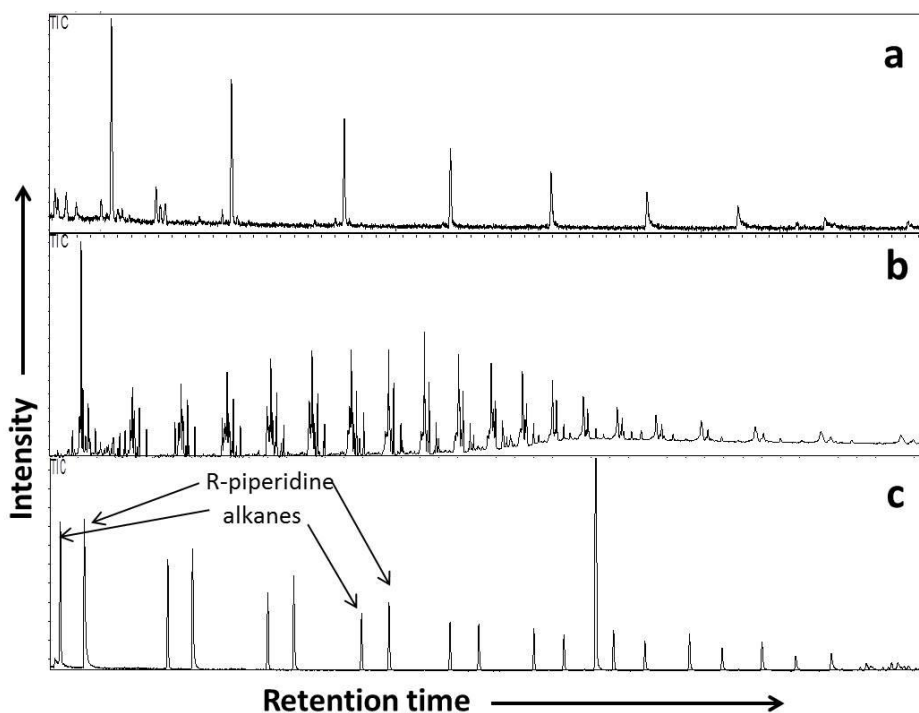


Figure 12 Representative sections of GC chromatographs for products from the run of decalin single-phase without pyridine (a), decalin single-phase with pyridine (b) and emulsion phase with pyridine (c).

Results of HCl run are reported in Figure 10. The product distribution at CO conversion of 94.7% was very similar to that obtained without the addition of HCl. Adding pyridine to decalin single-phase reaction resulted in much lower conversion and a wide spectrum of products in comparison to the run in clean decalin single phase (Figure 12), including alkanes, alkene, long chain alcohols, acids and esters, clearly indicating the poisoning effect of pyridine. While conversion was also affected considerably in the emulsion phase run in the presence of pyridine, products consisted of only alkanes and alkylated piperidine, derived from pyridine, each following a neat ASF-type trend. The partitions of pyridine, its hydrogenated product, piperidine, as well as alkylated piperidine were obtained after the reaction and listed in Table 6. 86.3% of the pyridine and its derivatives were captured in water phase due to their higher partition capability in water.

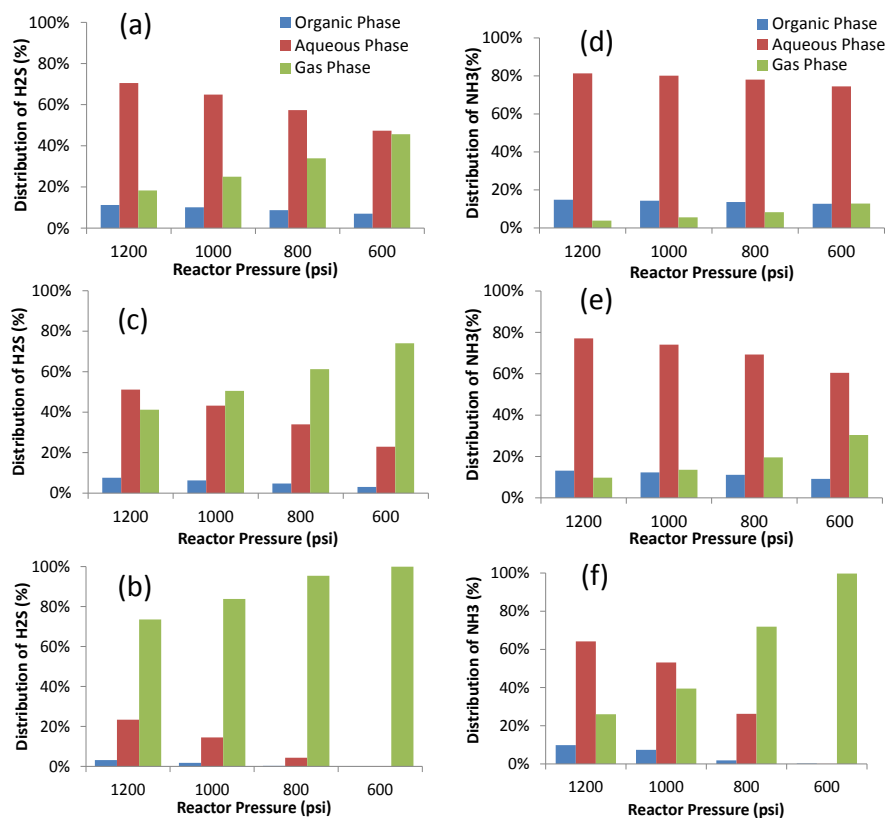


Figure 13 Distribution of hydrogen sulfide (left) and ammonia (right) in the three phases (organic, aqueous and gas phase) at 150 °C (a,d), 200 °C (c,e), and 250 °C (b,f).

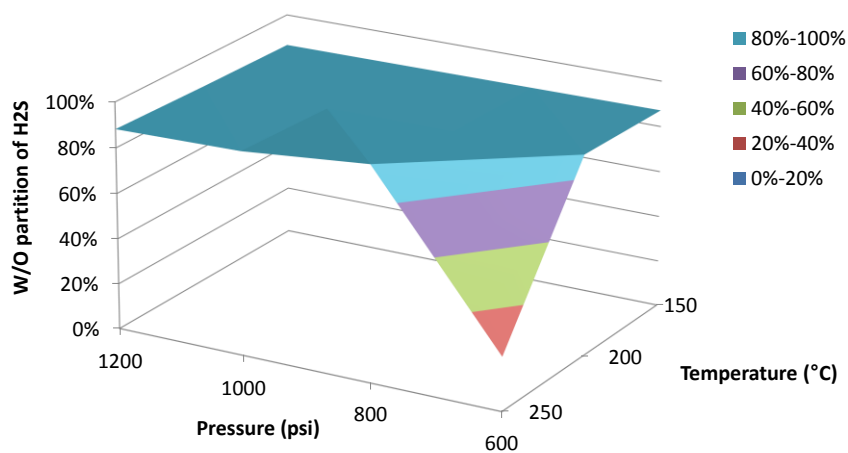


Figure 14 Partition of H₂S between organic and aqueous phases at different reaction conditions.

Calculations of partitions and mass transport of the impurities in different phases were conducted assuming thermodynamic equilibrium under a range of temperatures and pressures common to FTS. Figure 14 shows the partition plot of H₂S and it clearly indicates much higher partition in aqueous phase than in organic phase. Mass transfer parameters for H₂S and NH₃ are shown in Table 7. While the two molecules have similar diffusion coefficients in both aqueous and organic phases, their mass transport coefficients are smaller in organic phase than in aqueous phase. In addition, molar fluxes of H₂S and NH₃ in organic phase are at least twice smaller in organic phase than in aqueous phase. As a result, the undesired polar impurities experience higher transport resistance in organic phase. Thus the calculations lend support to the possibility of improving catalyst stability by adding additional resistance to transport of undesired polar impurities, and therefore higher impurity tolerance in emulsion phase FTS as shown experimentally.

Table 7 Mass transfer parameters of H₂S and NH₃ in decalin and water phase.

Molecule	H ₂ S		NH ₃	
	Decalin	Water	Decalin	Water
Diffusion coefficient (x10 ⁻⁸ m ² /s)	3.42	3.94	3.91	4.51
Mass transport coefficient (x10 ⁻¹ m*s)	0.942	1.12	1.06	1.26
Concentration (x10 ⁻² Kmol/m ³)	1.31	2.98	3.09	5.96
Molar flux (x10 ⁻³ Kmol/m ² *s)	1.23	3.33	3.28	7.52

Finally, to confirm that the formation of emulsion is partially responsible for the high CO conversion rate, Ru on carbon nanotubes only (without the hydrophilic head)

was used for a 12 h FTS reaction with $H_2/CO = 4$ under otherwise exactly the same conditions. As it turned out, the conversion with carbon nanotubes only, which was not expected to form emulsion, was only 28.1% as compared to the latter of 96.2%.

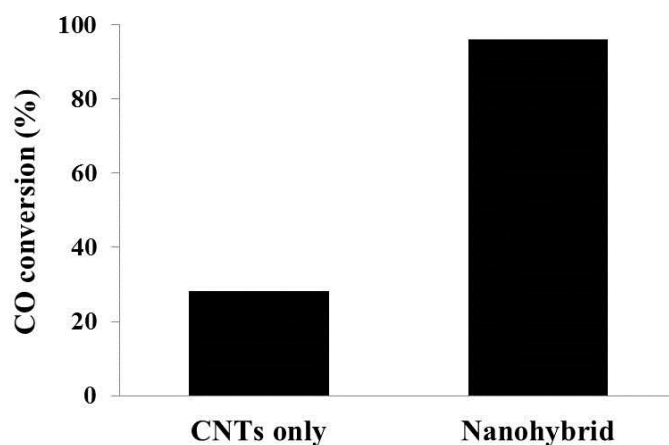


Figure 15 CO conversions with syngas ratio of 4 over 12 h in an oil/water mixture (1:1 ratio) using carbon nanotubes (CNTs) and nanohybrid as supports.

1.4 Summary

A novel multiphasic FTS system is proposed and demonstrated in this study, in which water and oil were mixed as the liquid reaction medium. The amphiphilic nature of the nanohybrid catalyst support used in the study facilitates the formation of the emulsion, in which the nanohybrid particles are stabilized at the water/oil interface. The FTS reaction conducted in the emulsion resulted in high CO conversion rates and a uniform ASF product distribution. Multiple potential benefits are envisioned for the FTS reaction in the emulsion system. One advantage of this system is that it allows for spontaneous product separation under reaction conditions purely based on solubility differences. This is especially significant for reactions like FTS that produce a wide

range of products with different polarities and solubilities. In addition, a more restricted mass transfer rate of impurities from the aqueous phase to the organic phase could greatly enhance impurity tolerance of FTS. One of the potential applications of the proposed system would be in FTS units with integrated syngas production by biomass gasification.

2. Liquid-phase Fischer-Tropsch synthesis: the rationale behind the choice of catalyst supports toward better productivity and selectivity

2.1 Introduction

2.1.1 Water effects in FTS

Water is the primary and inevitable FTS product. Therefore, its effects have long been studied [105,106]. There are usually multiple factors dictating the influences of water to FTS, and they largely depend on the metal chosen as the catalyst. The effects of water on Fe-catalyzed FTS are well understood, i.e., water re-oxidizes Fe during FTS and thus reduces catalyst activity [38,94,107-109]. Water effects on Co-based catalyst are more complex, depending on catalyst composition, nature of the support and catalyst preparation method. The water effects on FTS with unsupported Co catalysts were studied using fixed-bed reactor [110] and CSTR [111], and were found to result in enhanced CO reactivity, which was ascribed to lower barrier of CO dissociation due to water-CO interaction [112-114], oxidation of low coordination sites, or surface reconstruction [115]. Methane selectivity was found to be lower in comparison to “dry” conditions in all these cases, and was attributed to higher surface concentration of active carbon intermediates [115]. Meanwhile, as a result of competitive adsorption of water, secondary hydrogenation of alkenes was inhibited and more alkenes were produced [111]. Study has also shown that oxidation of Co by water is possible when the particle size is smaller than 4 nm [116]. For supported Co catalyst, besides the above mentioned effects, extra considerations are given to the interaction between support, metal and water. For example, the addition of water vapor facilitates the formation of cobalt silicate of Co-silica catalyst. Cobalt silicate has stronger interaction with cobalt oxide,

which retards the reduction of the latter and causes catalyst deactivation [117]. Similarly, when alumina was used as support, the formation of hard-to-reduce cobalt aluminate was observed with water addition [118]. TiO₂ support doesn't react with Co in the presence of water. Therefore, the effects of water on Co-TiO₂ catalyst are similar to unsupported Co catalyst at low water partial pressure. However, at higher water partial pressure, it was postulated that water would form a condensed phase, facilitating the transport of CO and H₂, and therefore favoring FTS [94].

With highest tolerance against oxidation by water and high activity by itself, Ru is an ideal catalyst to study the fundamentals of FTS, such as the effects of water [13,119-124]. A more recent study on this topic using Ru catalyst was conducted in a continuously stirred slurry reactor [91], which is close to the experimental apparatus in our own study. It was found that as the water partial pressure was increased, CO consumption rate also increased, while methane selectivity decreased and C₅₊ selectivity increased, which was in agreement with several studies on Co catalysts [109,125-127] and ascribed to product desorption inhibition and chain growth promotion by water [109]. Low carbon number range products (C₃-C₇), which are not subject to secondary reactions, increased with water partial pressure in formation rate and weight distribution, reflecting the promoting effect of water on the primary chain growth probability. On the other hand, secondary hydrogenation was inhibited by water, as indicated by higher alkene contents at large carbon numbers, a range more subject to secondary hydrogenation due to longer chain-induced higher solubility [12,52,128-131] or diffusivity [17], and therefore longer residence time, in comparison to “dry” conditions.

As can be seen, the effects of water on Co- and Ru-based catalysts share many similarities, e.g., increased CO consumption rate, suppressed methanation, and higher alkene contents. The essential question is how water affects the catalyst activity, a question that's been eluding conclusive answers. In spite of observations of water-CO interactions [112-114], these studies didn't pin point how it facilitates CO dissociation, a step believed to be rate-limiting for FTS [101]. Rate enhancement due to water-assisted transport [94] is still a possibility. However, the use of very small catalyst particles ($< 100 \mu\text{m}$) in the above study largely excluded intra-pellet transport limitation. Another explanation given in this study was that water supplies a source of surface hydrogen needed for CH_n species formation. While the explanation was rather brief and ambiguous, it did point to a direction that is better supported and elucidated by recent studies on Fe and Co [101], and Ru [40], which compared, experimentally and theoretically, the activation energy for CO dissociation via direct route vs. hydrogen assistance, i.e., carbide mechanism vs. enolic mechanism. It was determined that hydrogen-assisted CO dissociation has much lower energy barrier. Therefore it is the dominant pathway. Water may increase the rate of kinetically-relevant CO activation steps by mediating the formation of COH^* via a H-shuttling mechanism, in which H^* transfers to a nearby H_2O molecule to form a short-lived H_3O^+ intermediate which can then protonate the O of CO^* [39]. The thus formed COH^* undergoes H^- addition at the C to form $^*\text{HCOH}^*$ and then dissociates with H_2O nearby as a solvent in the kinetically-relevant step. The transition state for this step has an energy of 129 kJ mol^{-1} compared to a CO^* -covered surface with H_2 and H_2O in the gas phase, while it is 193 kJ mol^{-1} compared to a CO^* -covered surface and H_2 in the gas phase. The CO

consumption rate, methane and C_{5+} with respect to water pressure follow similar trends as reported above. Beyond a water pressure value of 0.3 MPa, the effects became much weaker, suggesting blocking of active sites by water derived intermediates. It should be noted that all of the above studies involved the addition of vapor-phase water only.

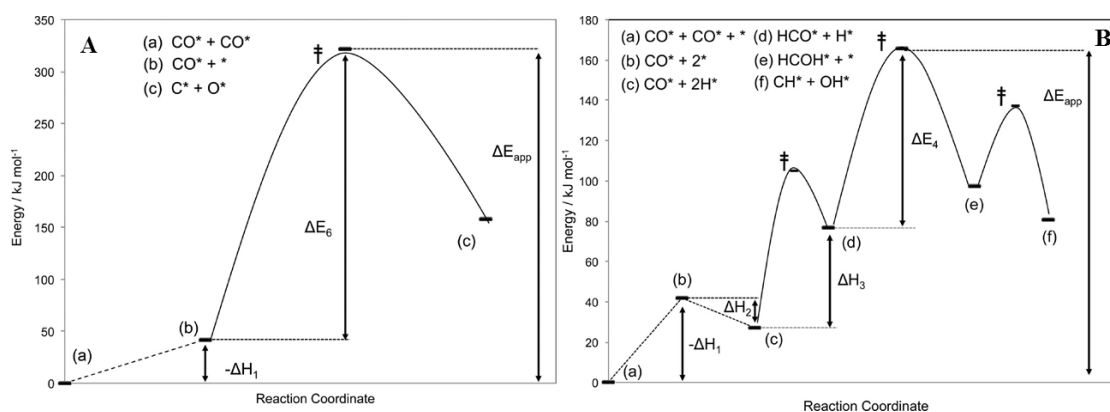


Figure 16 (A) DFT-derived energy diagram for vacancy generation and direct CO^* activation on (111) terraces of Ru_{201} (1.55 ML CO^*). The apparent activation energy (ΔE_{app}) for the direct path is a sum of the energy required to generate a vacancy ($-\Delta H_1$) from a CO^* -covered surface (a) and the intrinsic activation energy (ΔE_6) for direct activation of CO^* by a surface vacancy (b) to form chemisorbed C^* and O^* species (c). (B) DFT-calculated energy diagram for H -assisted CO^* activation path on the (111) terrace of Ru_{201} (1.55 ML CO^*). The apparent activation energy for the H^* -assisted path is a sum of the energy required to generate a vacancy ($-\Delta H_1$) from a CO^* -covered surface (a), the enthalpy of H_2 adsorption (ΔH_2 ; (b) to (c)), the enthalpy of H^* addition to CO^* (ΔH_3 ; (c) to (d)), and the activation barrier for H^* addition to HCO^* (ΔE_4 , (d) to (e)). The barrier for the dissociation reaction of $HCOH^*$ to $CH^* + OH^*$ ((e) to (f)) is shown to justify the irreversibility of HCO^* hydrogenation. Transition-state energies are denoted by double daggers (from Reference 40).

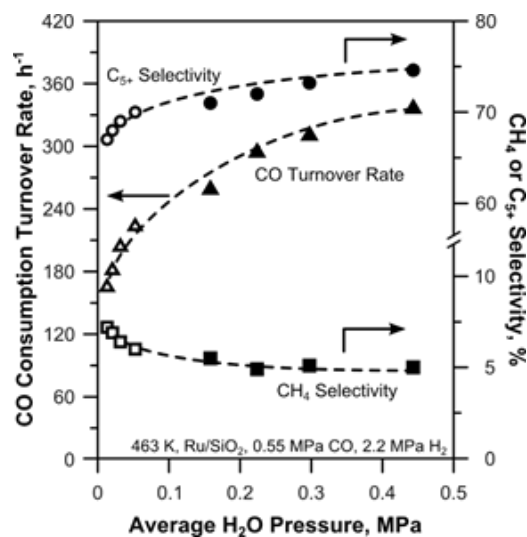


Figure 17 CO consumption rate, selectivity to CH₄, and selectivity to C₅₊ products as a function of the average H₂O partial pressure on a 5 wt% Ru/SiO₂ catalyst. (Open symbols) Space velocity runs; (Closed symbols) H₂O-addition runs (from Reference 39).

2.1.2 Research objectives

We have demonstrated in Chapter 1 the concept of FTS in emulsion phase using nanohybrid-supported catalysts and its multiple advantages, among which the enhanced CO consumption rates in comparison to oil single-phase are an important observation and in line with literature reports, which, however, only explored the addition of water vapor together with syngas feed. As will be discussed below, the presence of liquid water would be expected to behave differently from water vapor in three major ways: 1) liquid water under FTS conditions guarantees maximum chemical potentials that water could reach at thermodynamic equilibrium, since water is saturated; 2) liquid water induces other effects that water vapor doesn't. For example, syngas has diffusion coefficients in water that are three times higher than in typical hydrocarbon liquids [132,133], meanwhile its solubility in water is lower [134]. In addition, FTS products

have very different diffusion and solubility behaviors in water than in organic solvents as well. Therefore, mass transfer might be an important consideration; 3) Depending on the catalyst and catalyst support used, the bi-phasic system, i.e., the mixture of water and oil, might have different configurations. A direct example is the emulsion system that we focus on in this study, which results from the amphiphilic nature of the support, i.e., the nanohybrid support possesses both hydrophobic and hydrophilic properties. This solvent-catalyst interaction not only determines the liquid configuration (e.g, emulsion), but also how catalyst particles are distributed. For example, our study showed that the majority of the catalyst particles are located on the hydrophobic carbon nanotube side of the nanohybrid. Therefore, catalyst would be more in the oil phase in the emulsion system. In this sense, catalyst support plays a more important role in liquid phase reaction than in gas phase reaction. A detailed examination on the FTS reaction in biphasic system, emulsion in particular, would provide significant insight both scientifically and industrially. Recently, FTS carried out in liquid water was reported for the first time and showed promising results, i.e., much higher CO consumption rates than in common organic solvents [135]. In light of this result, and as a natural continuation of our study, FTS in water single-phase was carried out as well, and showed very different behavior than FTS in emulsion phase. Interpretation of these results involves the fore-mentioned considerations, as well as new insights on FTS and on catalysis in general.

2.2 Experimental

Catalysts were prepared via incipient wetness impregnation method to load Ru onto different supports. Ruthenium (III) chloride hydrate (99.98%, Sigma-Aldrich) was dissolved in water and impregnated drop-wise onto a determined amount of support, which were nanohybrids as used in Chapter 1, activated carbon (Darco, Aldrich), or fumed silica (Aerosil 380, Evonik). The samples were then dried for approximately 12 h in a vacuum oven at 80°C and subsequently reduced in flowing H₂/Ar (1/10 ratio) at 400°C for 3 h, followed by cooling down and passivation in flowing O₂/He (1% O₂) for 2h. Ru loadings were determined by inductively coupled plasma (ICP, Galbraith Laboratories), and the mean particle sizes were based on transmission electron microscope (TEM, JEOL 2000-FX). The FTS reaction was performed in a 100-mL stainless steel autoclave batch reactor from Parr Instruments. In a typical experiment, 150 mg of catalyst and 30 mL of solvent(s), i.e., decalin (mixture of cis + trans, anhydrous, ≥ 99% purity, Sigma-Aldrich), water (HPLC grade, Fischer Scientific), or decalin/water mixture at a 2:1 ratio were added to the reactor vessel. The reactor was sealed, purged and pressurized with H₂ to 400 psi for a reduction period of 12 h at 250°C. After reduction, the reactor was cooled down to room temperature, and syngas was introduced from a cylinder (H₂/CO = 3.5, Air Liquide) to purge and then pressurize to a total pressure of 600 psi. The reaction was conducted at 200°C at a constant stirring speed of 700 rpm. Same as the reduction step, the vessel was a closed and isolated system during the reaction. Conversion was monitored at different times by the pressure change observed during the reaction. The gas phase products were measured on the

GC/TCD (Carle 400 AGC), while the liquid phase products were analyzed after filtration using gas chromatography mass spectrometer (GCMS-QP2010S, Shimadzu) and GC (Agilent 7890B).

2.3 Results and Discussion

At the early stage of this study, FTS reactions were tested at a CO conversion of 20% or lower using 100 mg of catalyst, a H_2/CO ratio of 2 and run time of 2 h to acquire the initial catalyst activity, i.e., turnover frequency (TOF) as a function of changing amount of water, while the total volume of the solvent(s) was kept constant. It should be noted that, the calculation of TOF excluded water-gas shift reaction, since this reaction converts CO into CO_2 which is not a direct and desirable FTS products. Figure 18 shows the evolution of TOF along with that of methanation, i.e., the molar percentage of methane produced with respect to the amount of CO consumed. According to calculation (see Appendix), water in excess of 1.2 mL and 0.5 mL would be in liquid form at the reduction and reaction conditions, respectively. The observed TOF enhancement and methane selectivity drop with increased water content agree well with previous studies conducted in the vapor phase [39]. An interesting point to emphasize is that the trends continue well beyond the threshold for appearance of liquid water. That is, while the chemical potential of water does not increase beyond the saturation, the presence of increased amounts of liquid water seems to continue to enhance TOF and suppress methanation to a certain extent. We chose 10 mL of water + 20 mL of decalin as the standard composition, as this is the point where the catalyst

activity and product selectivity (as indicated by the TOF and methanation curves) are fairly stable, and the relatively higher fraction of oil phase coupled with the dominant hydrophobicity of the nanohybrid facilitates the formation of water-in-oil emulsion [81].

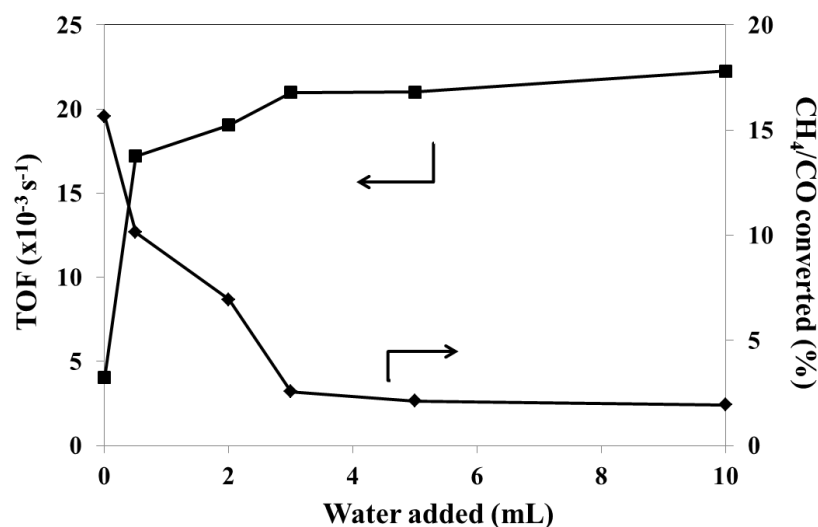


Figure 18 Evolution of TOF and methanation as a function of initial amount of liquid water added into decalin, keeping a total of 30 mL of solvent(s). Data obtained with syngas ratio of 2 at a low conversion of below 20% over 2 h reaction time.

The syngas ratio of 3.5 was used from this point throughout this study. TOF of the nanohybrid-supported catalyst was tested using 100 mg catalyst in decalin, emulsion and water with a relatively short reaction time of 2 h, which reached a conversion below 30%. Furthermore, to test catalyst deactivation, three more 2-h runs were followed in each case. Between these runs, the reactor was cooled down to room temperature, gas phase was sampled and released from the reactor vessel, then fresh syngas was introduced to the vessel to the initial pressure of 600 psi. The data were summarized in Figure 19. As can be seen, the catalyst exhibited lowest TOF of $25.2 \times 10^{-3} \text{ s}^{-1}$ in decalin phase. In emulsion and water single-phase, a much higher TOF of $39.2 \times 10^{-3} \text{ s}^{-1}$ and

$40.8 \times 10^{-3} \text{ s}^{-1}$ was obtained, respectively. In addition, the catalyst showed much slower deactivation rates over the four reaction cycles in emulsion and water phases: the TOF dropped by 33.6% and 22.9% respectively after three cycles, as compared to 62.2% in decalin phase. The enhanced catalyst activity in the presence of water agrees well with our earlier results of FTS in emulsion [136] and with other relevant FTS studies as well. The latter represent the long and on-going interest in exploring and unraveling the effects of water in FTS reactions. In these efforts, small amounts of water vapor were mixed with syngas to feed into liquid phase [91] or vapor phase reactor [137,138]. Mechanisms drawn from these studies vary, from water assisted intra-pellet transport of syngas and hydrocarbons [94], to water-shuttled transport of hydrogen to the active site to facilitate CO dissociation [39]. As mentioned above, syngas diffuses in water much faster than in organic solvents. In addition, in emulsion, the presence of the organic phase may pose a hindrance to the function of water as “hydrogen shuttle” toward catalyst surfaces. Therefore, water single-phase is more advantageous in terms of CO, H₂ and proton transfer, which is possibly the reason for the slightly higher activity in water single-phase than in the emulsion phase. Studies have shown that carbon deposition tends to form on Ru catalyst, causing deactivation [139,140]. In our study, at similar conversions, decalin single-phase had a carbon balance of less than 70%, while emulsion and water single-phase gave carbon balances of above 80%. Since gas phase and liquid phase products were captured by the respective GC and/or TCD, it is reasonable to speculate that carbon deposition on the catalyst was more severe in decalin single-phase reaction, causing the observed higher rate of deactivation relative to that in emulsion and water single-phase. Hydrothermal gasification of carbon

[141,142] and biomass [143-147], where carbonaceous materials are converted to gases (mainly CO and H₂) in the presence of water at elevated temperatures and pressures, are well established technologies, and the latter has been highly pursued as a promising approach toward biomass utilization. Ruthenium, among many other metals, has been shown to be a very active catalyst for this process [148,149] Therefore, with water under the FTS conditions of elevated temperature and pressure, the carbonaceous deposition on Ru surface could easily undergo hydrothermal gasification, a scenario that explains the slower deactivation rates in the cases of emulsion and water single-phase.

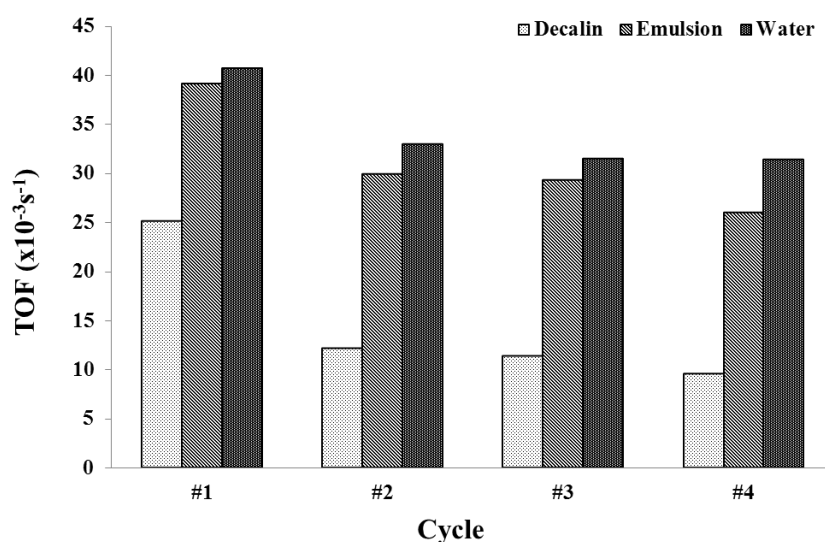


Figure 19 Turnover frequency of nano-hybrid-supported catalyst in different solvents over four reaction cycles, each cycle being 2 h. Between cycles, the reactor was cooled down to room temperature, gas phase was sampled and released from the reactor vessel, then fresh syngas was introduced to the vessel to the initial pressure of 600 psi.

The molar fractions of the three major FTS products, i.e., alkanes, alkenes and alcohols, were surveyed for C₆, C₁₂ and C₁₈ at similar conversions around 65% (Figure 20). In comparison to products of decalin single-phase, those of emulsion and water

phases are higher in alcohol content, especially at low carbon numbers (e.g. C₆). Our previous study has shown that alcohols are products of alkene hydration in our case [136]. In the presence of abundant amount of water, alcohols would be less subject to dehydration and therefore more likely tend to retain their alcoholic form. This is especially true for short alcohols due to their higher affinity to water. Another interesting observation is that, relatively less alkenes and more alkanes were produced in water single-phase. While alkenes can promptly dissolve as a primary product in the presence of decalin as the reaction medium, in water single-phase, their poor solubility in water would enable more contact and more re-adsorption to the catalyst surface, and therefore more secondary hydrogenation. It should be noted that, pure alkane products can be easily obtained upon hydrogenation of the as-produced products, or at higher conversions, as shown in Figure 21.

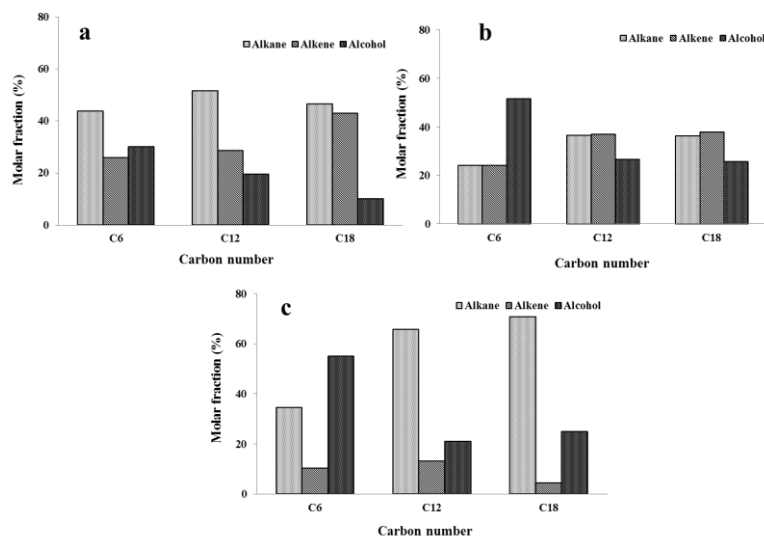


Figure 20 Alkane/alkene/alcohol fraction for C₆, C₁₂ and C₁₈ products in decalin (a), emulsion (b) and water (c) at a conversion \approx 65%.

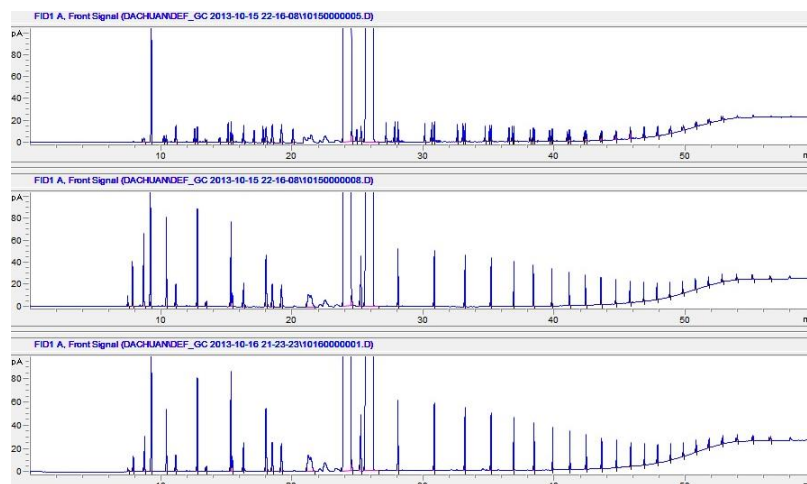


Figure 21 GC chromatographs of products from FTS with nanohybrid-supported catalyst in emulsion phase at a conversion of 64.7% before hydrogenation (a), after hydrogenation (b) and at a conversion of 91.0% without hydrogenation (c).

Figure 22 compares product carbon chain length distribution in terms carbon molar fractions at the same nearly-identical conversions as above. It can be seen that in decalin single-phase, the lightest group (C_1 - C_4) has the highest fraction of carbon of nearly 47%, and nearly 33% in the case of water single-phase. In the case of emulsion, chain length distribution is drastically different: the fraction of the lightest C_1 - C_4 range is the lowest ($\approx 10.5\%$) in comparison to longer ranges as well as to the same range of decalin and water single-phases. The C_5 - C_{12} range, in contrast, is the highest at over 55%, and the “primary” C_5 - C_{20} make up the vast majority (76.2%) of the products. For reference at low conversions, the C_1 - C_4 hydrocarbon fractions, defined as the percentage of total number of carbon atoms in this product portion with respect to the total number of CO molecules consumed, are listed in Table 8 along with their corresponding conversions. The light product fractions were measured in this way so that only gas phase measurements were involved, since at low conversions, liquid phase products exhibit higher noise-to-signal ratios on GC, causing more systematic errors. In

addition, in catalyst recycling test, in which the liquid products are collected only after the last cycle is finished, this is the only way to measure the selectivity toward light products for each individual cycle. Although this leaves out the alcoholic part of the products, if any, it is not indiscreet to conclude that at low conversions, the fractions of the C₁-C₄ range products follow the same order of decalin > water > emulsion. Furthermore, as the conversion increases, the C₁-C₄ fraction increases as well in all three cases. The much higher selectivity to C₅₊ products in the presence of water agrees well with numerous studies on Ru [91,150] and other catalysts such as Co [151-153] and was attributed to water-inhibited hydrogenation leading to more alkene availability for chain growth and/or water-inhibited product desorption [154], intra-pellet water phase facilitating syngas transport [94], or water as surface hydrogen supply [91].

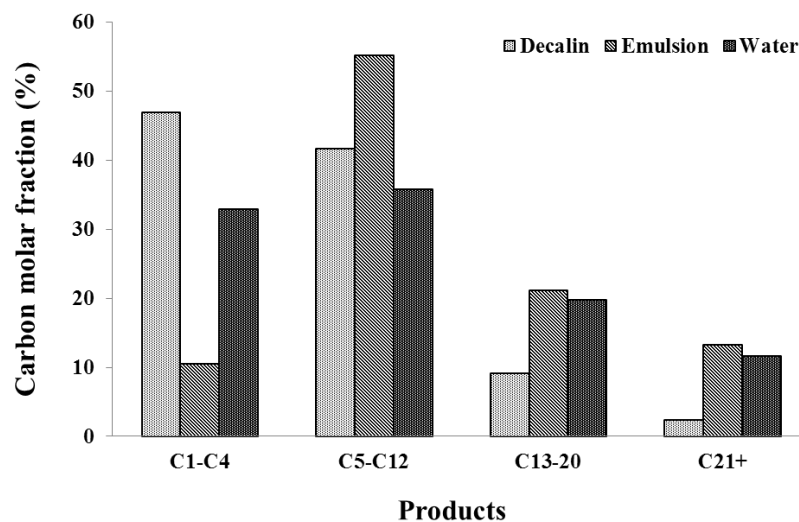


Figure 22 Product distribution at a conversion $\approx 65\%$ in decalin, water and emulsion (Syngas ratio = 3.5, 150 mg catalyst, reaction temperature = 200°C).

Table 8 C1-C4 hydrocarbon fractions at low conversions

Reaction medium	Decalin	Emulsion	Water
Conversion (%)	23.2	25.5	28.8
C1-C4 hydrocarbon fraction (%)	22.1	6.0	13.4

While the high selectivity to light products (C₁-C₄) in the absence of water is explainable on the basis of prior studies, the selectivity to products of this range in water single-phase is much higher than in emulsion, which defies straightforward interpretation and deserves further examination. Product carbon chain length distributions at incremental conversions from emulsion and water single-phase reactions are shown in Figure 23a and 23b, respectively, and the difference is apparent: not only was selectivity to C₁-C₄ much higher in water single-phase, the selectivity also increased dramatically with increasing conversion. In contrast, in emulsion, only slight increase in C₁-C₄ was observed with increasing conversion, and the change in the overall chain length distribution was minimal: the fraction of the C₅-C₂₀ range shifted from 76.6% to 72.3% with corresponding conversions from ~40% to ~80%, as opposed to a large drop from 53.7% to 35.7% in water single-phase with a similar conversion span. A more straightforward comparison in selectivity to light products between water and emulsion is shown as gas phase hydrocarbon product fraction in Figure 23c. Meanwhile, conversion in these two systems evolved differently as well. As shown in Figure 24, the conversion rate in water single-phase started off higher than that in emulsion phase but decreased much faster, and dropped below that in emulsion phase

shortly before 2 h. It should be noted that, since the FTS was carried out in sealed batch, syngas pressure would drop as conversion went up. Therefore conversion rate is expected to drop, and eventually down to nearly zero as syngas is exhausted, whether there is catalyst deactivation or not. Nevertheless, the observation of the two systems at the same conversion makes comparative sense, since FTS consumes syngas at a stoichiometric H_2/CO ratio of ~ 2 . At the same conversion, therefore, difference in syngas partial pressure should be excluded from accounting for the different conversion rates. The higher conversion rate at low conversion level in water single-phase corresponds well to the higher TOF of the catalyst mentioned above. And as discussed earlier, it is a result of higher diffusion coefficient of syngas in water, which, in turn, indicates the presence of syngas mass transfer limitation to a certain extent in emulsion. Taking together the evolution of carbon chain distribution and conversion rate with respect to conversion, one can see a clear association between the catalyst deactivation and increase in selectivity to light products in both emulsion and water single-phase, and this deactivation, and correspondingly the increase in light product selectivity, happened in water single-phase to a much larger extent.

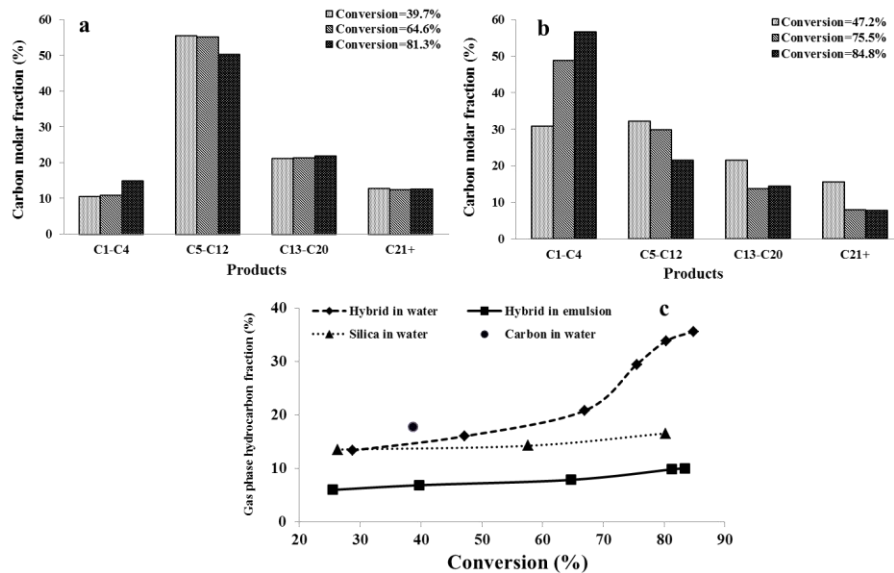


Figure 23 Product distribution at different conversions in emulsion (a) and water single-phase (b); Gas phase hydrocarbon fraction vs. conversion with different catalysts in different solvents (c) (Syngas ratio = 3.5, 150 mg catalyst, reaction temperature = 200°C).

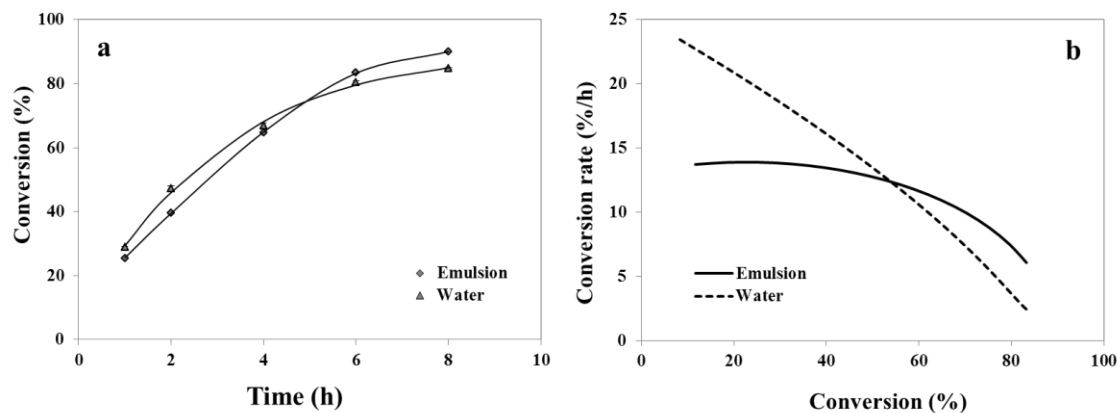


Figure 24 CO conversion vs. reaction time in emulsion and water phase, with each data point from a separate run (a), and CO conversion rate vs. conversion in emulsion and water phase, analytically obtained from the plot of CO conversion vs. reaction time (b).

To obtain more insight into the deactivation mechanism, FTS were carried out with 150 mg catalyst for 6 h first. Then a short 2-h run was followed, observing the same between-run procedures used in the recycle tests for catalyst deactivation. Data

from this 2-h run were compared with those from the fourth (last) 2-h run of the aforementioned recycle test, and are listed in Table 9. The first and foremost observation is that, in emulsion, the TOF of the catalyst after a 6-h run was not very different from that after three 2-h runs. In sharp contrast, in spite of the same total reaction time beforehand, intermittently or continuously, the catalyst in water phase suffered much more severe deactivation in the latter case, that is, the catalyst after a continuous 6-h run was 33.9% less active than that after three 2-h runs. This comparison can be better illustrated in Figure 25 (Columns highlighted inside the rectangle). Furthermore, while the two compared 2-h runs in water gave similar CO conversions, the run with much less active catalyst (i.e., the one preceded by 6-h run) led to much higher selectivity to gas phase products. This further consolidates the association between catalyst deactivation and increased selectivity to light products established earlier.

Table 9 Data of 2-h FTS reactions with different catalyst pretreatments

Solvent	Parameter	after three 2-h runs (100 mg cata.)	after one 6-h run (150 mg cata.)
Emulsion	TOF ($\times 10^{-3} \text{s}^{-1}$)	26.0	26.5
	CO conversion (%)	19.0	29.4
	Gas fraction (%)	9.3	13.4
Water	TOF ($\times 10^{-3} \text{s}^{-1}$)	31.4	20.8
	CO conversion (%)	23.2	23.9
	Gas fraction (%)	13.6	22.6

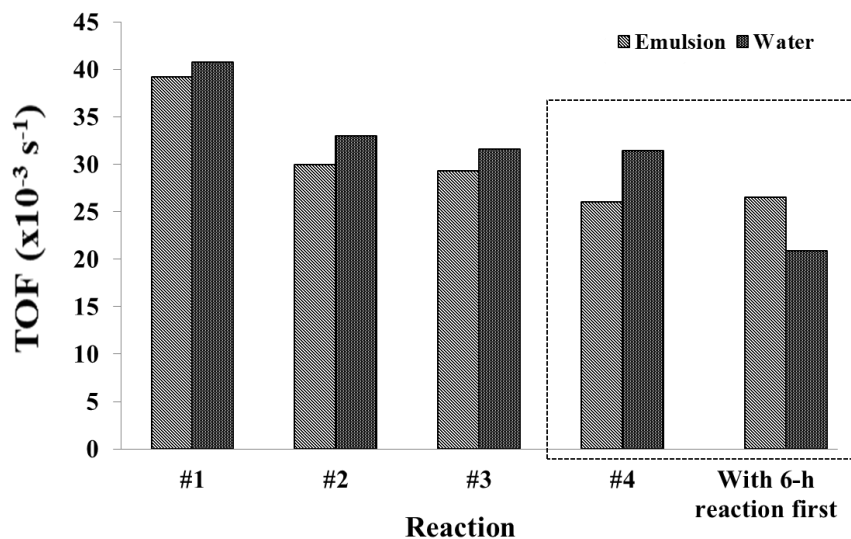
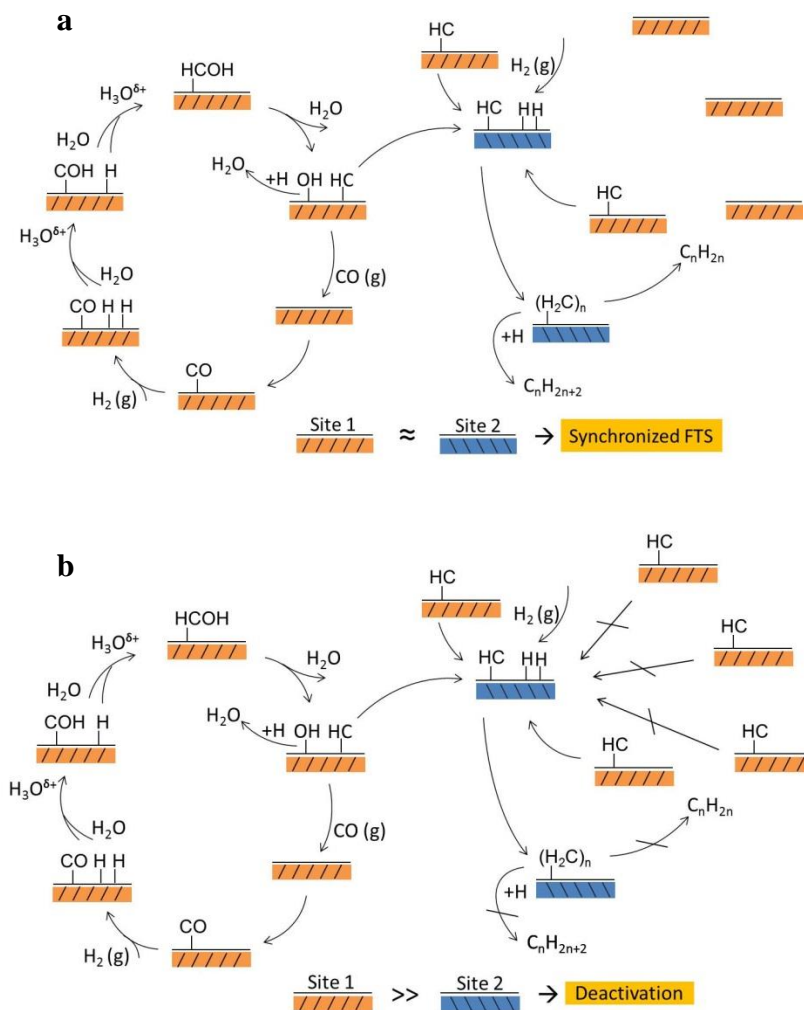


Figure 25 Evolution of catalyst TOF during recycle tests and after 6-h reaction (Syngas ratio = 3.5, 100 mg catalyst for recycle tests, and 150 mg catalyst for 6 h-2 h test, reaction temperature = 200°C).

This association between catalyst deactivation and increased selectivity to light products has been observed earlier [155,156]. Very recently, an explanation was proposed [139] that takes into account the lately developed dual-site model for FTS [157,158], in which one of the two sites on FTS catalyst (Site 1) is responsible for CO dissociation while the other (Site 2) responsible for chain growth. According to the explanation, FTS catalyst deactivates due to carbonaceous species formation on the CO dissociation site, leading to decrease in C₁ species and consequently, decrease in chain growth possibility and thus lighter hydrocarbon fractions. Here we've found this explanation coordinates well with our observations, and the difference in the results in water single-phase and emulsion can be well interpreted in light of the dual-site model. In water single-phase, where syngas has much higher diffusion coefficient than in organic phase as mentioned above, production of C₁ species can quickly pick up on fresh catalyst where Site 1's (as well as Site 2's) are abundant. Therefore, the amount of

C_1 species can easily exceed the consumption capability of Site 2, causing excess C_1 that then forms carbonaceous deposits and poisons Site 1. In addition, hydrocarbon chains may not desorb promptly upon formation due to their hydrophobicity, and this further reduces the number of chain growth sites available. When reactions are carried out intermittently with short runs, as in the case of catalyst recycle test composed of four 2-h runs, each termination enables the still active CO dissociation sites to restore their original state before poisoning sets in, and the interval allows more time for hydrocarbons to desorb and free up chain growth sites. Thus, catalyst deactivation does not appear as severe as after a continuous run of equal total duration. In emulsion, the balance between Site 1 and Site 2 can be well adjusted in two major ways. First, there is constraint of syngas mass transfer to a certain extent due to its lower diffusion coefficient in oil that is part of the emulsion, so that C_1 formation on Site 1 doesn't overwhelm C_1 consumption on Site 2, or at least not as soon as in the case of water single-phase. Second, in emulsion, products can more readily desorb from catalyst surface into oil due to their higher solubility in oil phase, and Site 2 can be regenerated quickly for continued chain growth. Therefore, different from water single-phase, emulsion serves to preserve both sites and helps to retain a relative balance between the two sites. The catalyst deactivation in this case is not expected to be a strong function of time, which is well illustrated by the almost equal TOFs after three 2-h runs and after one 6-h run.



Schematic 6 Overall FTS process on the catalyst surface in emulsion, which maintains synchronized activity between Site 1 and Site 2 (a), and in water single-phase, which has much higher initial activity on Site 1 than on Site 2 and thus causes quick deactivation by carbonaceous species from excess CH^* units (b).

It should be noted that there existed studies prior to the proposal of dual-site model that hinted in the same direction. Through carbon isotope transients study on Co catalyst, Bertole et al.[115] pointed out that water increases CO activity to dissociate and thus increases the surface coverage of C^* . However, there is no parallel increase in the overall reactivity of C^* . As a result, there is a “carbon crowding” effect that causes

higher selectivity to heavy products. Despite a different explanation regarding the effects of water in enhancing CO dissociation, this opinion shares the essential perspective with our explanation using the dual-site model, that is, there exists an issue of balance between the production of active carbon monomer species and consumption of them, and that the consumption rate of the monomer species is not altered by water. On the other hand, the authors didn't consider "carbon crowding" as a possible deactivation pathway but catalyst sintering instead. In our study, TEM examination of the spent catalysts from emulsion and water single-phase suggested that the Ru catalyst particles sintered to the same extent in both cases, as shown in Figure 26.

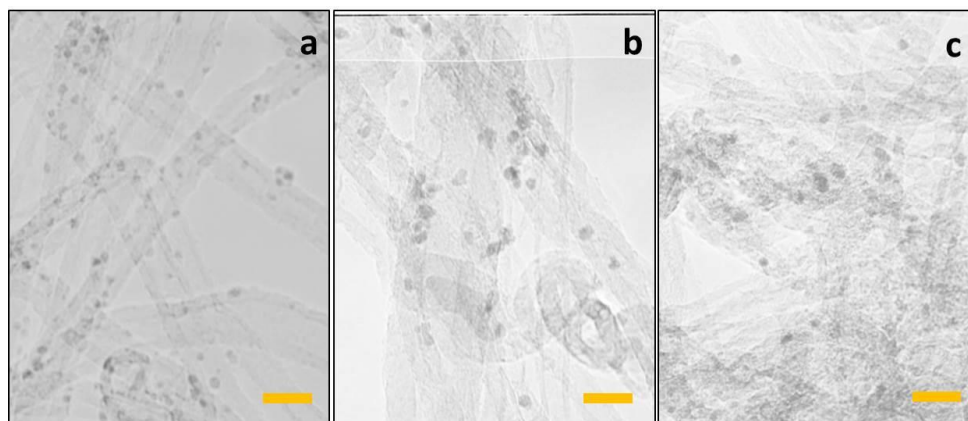


Figure 26 TEM images of fresh Ru catalyst (a), spent catalyst in emulsion for 8 h (b) and spent catalyst in water for 8 h (c). (Syngas ratio = 3.5, 150 mg catalyst for 8 h reaction at 200°C. Scale bar is 10 nm).

Given that the nanotube ends of the nanohybrids bearing most of the Ru catalyst particles are hydrophobic, it is a reasonable hypothesis that in water single phase, the hydrocarbon molecules would tend to stick to the carbon nanotube walls instead of desorb, while in organic phase or at least in the presence of it, the driving force to desorb is much higher. As a result, as the conversion increases in water single-phase,

thin layers of hydrocarbon film would form around the catalyst particles. This has two effects: 1) it blocks the active surface sites, causing catalyst deactivation; 2) the affinity of the hydrocarbons to the catalyst surface makes them more prone to hydrogenolysis. As a test, a model hydrocarbon compound, dodecane of nearly equivalent C amount to that after a 8 h reaction, was placed in either emulsion or water single-phase at 200°C under 400 psi H₂ for 6 h. The resulting composition after the reaction is shown in Figure 27. It can be seen that in water single-phase there are shorter hydrocarbons that make up for the loss of dodecane. In emulsion phase, however, there is only very slight loss of dodecane. While the extent of hydrogenolysis did vary between emulsion and water single-phase, the amount of methane from the hydrogenolysis in water single-phase was still only negligible in comparison to that from FTS in water single-phase. Therefore, we conclude that this is a possible but minor effect.

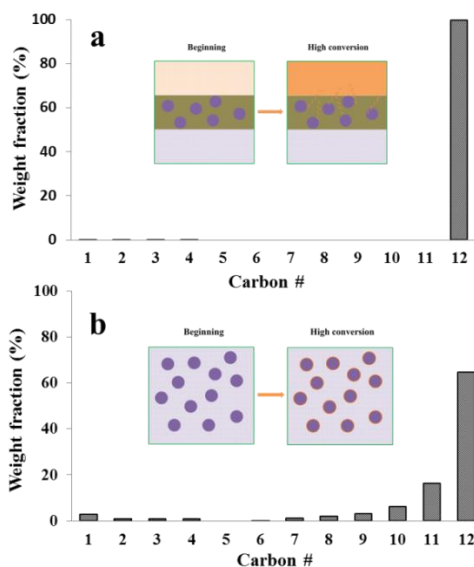


Figure 27 Hydrogenolysis test in emulsion (a) and water single-phase (b) using dodecane as the probe compound. Insets: schematics of the extraction of hydrocarbon products in emulsion (a), and formation of hydrocarbon film coating on catalyst particles in water single-phase (b).

Extending the type of catalyst supports provided further insights into the interplay between catalyst supports, solvents and products. As a comparative study, two other support materials were used, activated carbon, which is hydrophobic, and silica, which is hydrophilic. The TEM images of the three catalysts are shown in Figure 28 along with the optical images of the three supports in decalin/water mixture. As can be seen, the Ru particles on activated carbon has a very small average size of about 1.3 nm, while the average Ru particle size on silica is 4 nm. This difference is expected, considering the complexity and high defectiveness of the surface of activated carbon, which includes carboxylic groups, hydroquinone free radicals, quinones, metallic ions and nitrogen impurities [159]. The defects, together with the large surface area, make activated carbon a good dispersing agent. In comparison, silica surface is rather inert, and it has much lower surface area.

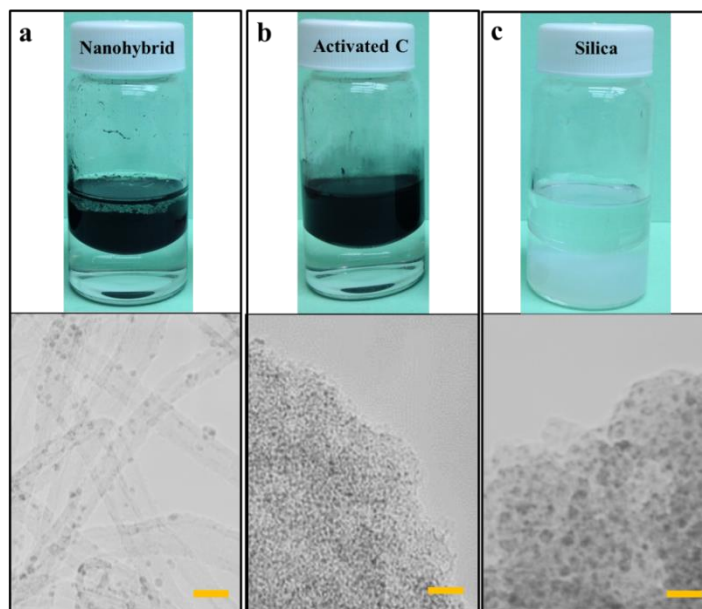


Figure 28 TEM images of Ru supported on nanohybrid (a), activated carbon (b) and silica (c) and optical images of the corresponding support in decalin/water mixture. Scale bar is 10 nm.

Figure 30 shows the TOFs of the three catalysts in the three solvents based on 2-h runs. As can be seen, TOFs of the activated carbon-supported catalyst are much lower in all three solvents in comparison to that of nanohybrid-supported catalysts, while the silica supported catalyst has the highest TOF except in emulsion. That is, the TOFs roughly follow the same order of particle size variation. It should be noted that in the cases of activated carbon and silica, the term “emulsion” merely denotes a mixture of 10 mL water and 20 mL decalin, since neither support actually facilitates the formation of emulsion. The CO conversions of the three catalysts in different solvents for 2 h and 8 h runs are plotted in Figure 30.

These results reveal the particle size effect on FTS activity, as well as the critical role of nanohybrid as catalyst support in the emulsion system. Studies have showed a common observation that the catalyst activity is usually higher on relatively large particles. For example, a study on the particle size effect on TOF investigated Co in the range of 2.6-27 nm and found highest TOF occurred on 6-8 nm particles [160]. In another study on FTS with Ru [161], the highest TOF appeared with particle size of 6.3 nm. This was usually ascribed to large domain or fraction of sites present on planar surfaces needed for high FTS activity, which seemed rather ambiguous. Here we propose an alternative explanation incorporating the dual-site model. According to the model, B₅ sites, which consist of an arrangement of three Ru atoms in one layer and two further Ru in the layer directly above this at a monoatomic step on an Ru(0001) terrace [162], are the sites responsible for CO dissociation (Site 1) [158]. Calculation has shown that the maximum concentration of B₅ sites is obtained on Ru particles with a diameter of 2 nm [163], which happened to be the average Ru particle size on

nanohybrid in this study. Below 2 nm, the site concentration rapidly drops to zero; above 2 nm, the site concentration drops in a parabolic and less dramatic way. On the other hand, the smaller the particle is, the less stable B₅ sites are and the higher the barrier for CO dissociation [158]. Taken both effects into consideration, Ru particles less than 2 nm in size favor CO dissociation the least, and the optimal size for CO dissociation would be one somewhat larger than 2 nm, e.g., 6.3 nm as reported in the above mentioned study. Therefore, the three catalyst in this study would exhibit CO dissociation activity in the order of Ru/silica > Ru/nanohybrid > Ru/C, the same order with their particle sizes. As we see from Figure 29, this is the case in both decalin and water single-phase. However, this doesn't apply in the case of emulsion. Instead, Ru/nanohybrid is the catalyst that exhibited the highest TOF, that is, the amphiphilic effect of the nanohybrid overruled that of the particle size and became a more dominant factor. By reference to the explanation given earlier for the higher TOF of the Ru/nanohybrid catalyst in water single-phase, we propose that the emulsion phase formed in the presence of the nanohybrid can be considered as a new single phase that has a higher syngas diffusivity than the overall diffusivity of oil/water mixture where Ru/C or Ru/silica is present in one of the phases. Careful calculation is needed to consolidate this explanation.

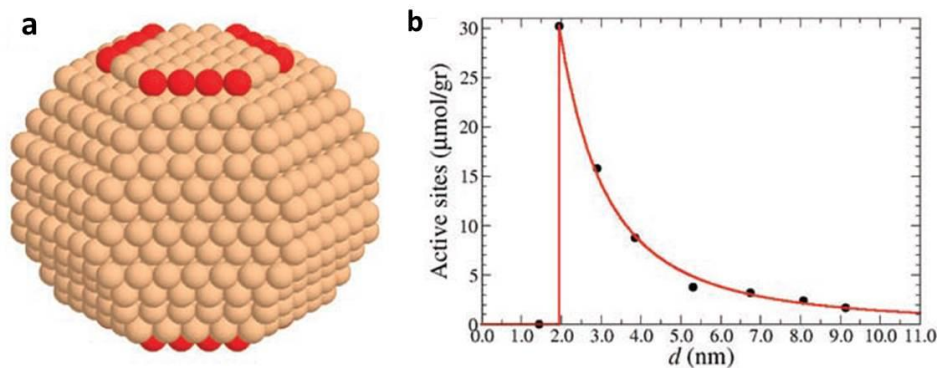


Figure 29 (a) A typical calculated Ru particle, with an average diameter of 2.9 nm. Atoms that belong to active B_5 sites are shown in red. (b) Density of active sites as a function of particle diameter, as calculated through analysis of the atomistic Wulff construction (adapted from Reference 163).

An interesting and noteworthy observation is that, in water single-phase, for 2 h run, silica-supported catalyst had a conversion of ~26.3%, which is much less than that of its nanohybrid counterpart at 47.2%. However, after 8h reaction, the former gave a conversion of 80.7% which is close to 84.8% given by the latter. In other words, the silica supported catalyst seemed to deactivate in water to a much less extent. With less number of Site 1 on the much larger Ru-on-silica, the fore-mentioned deactivation mechanism on Ru-on-nanohybrid, i.e., Site 1 quickly fulfills the needs of Site 2 for chain growth and causes site poisoning by excess carbon, is less likely to happen. Therefore, this catalyst didn't deactivate as much as that on nanohybrid, if any. Due to low CH supply from Site 1, chain growth probability should also be low, leading to more light products. This is evidenced by the constantly high gas phase hydrocarbon fraction, as plotted in Figure 23c. Overall, these results underpin the critical role of catalyst supports in determining the catalyst performance.

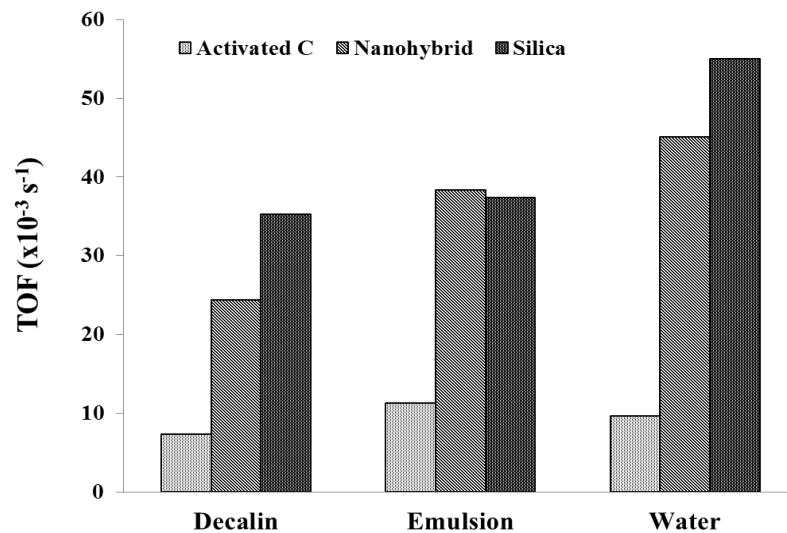


Figure 30 TOF of Ru catalysts on different supports in different solvents.

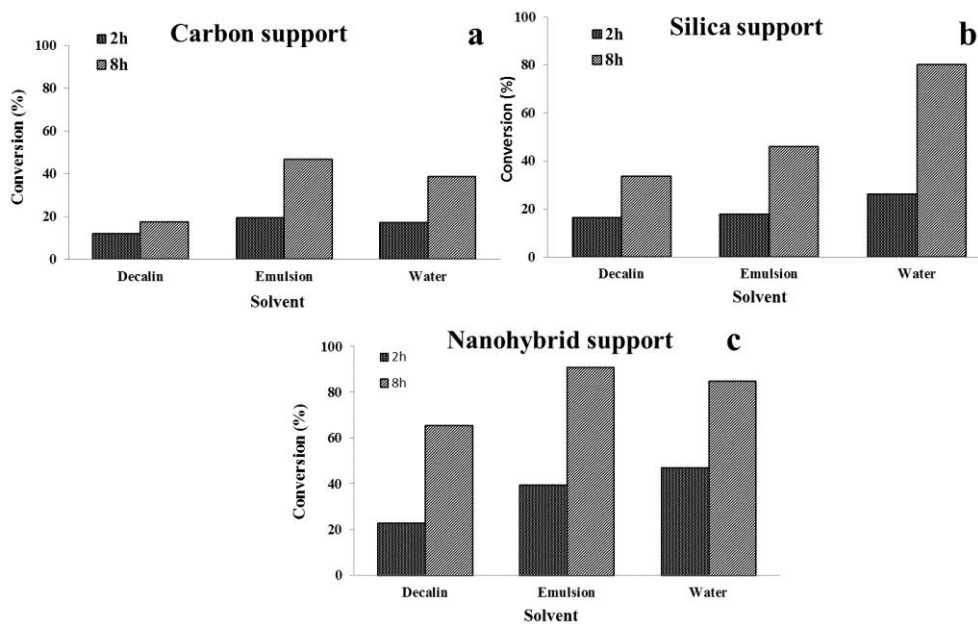


Figure 31 Conversions of FTS with three catalysts in different solvents at 2 h and 8 h reaction time.

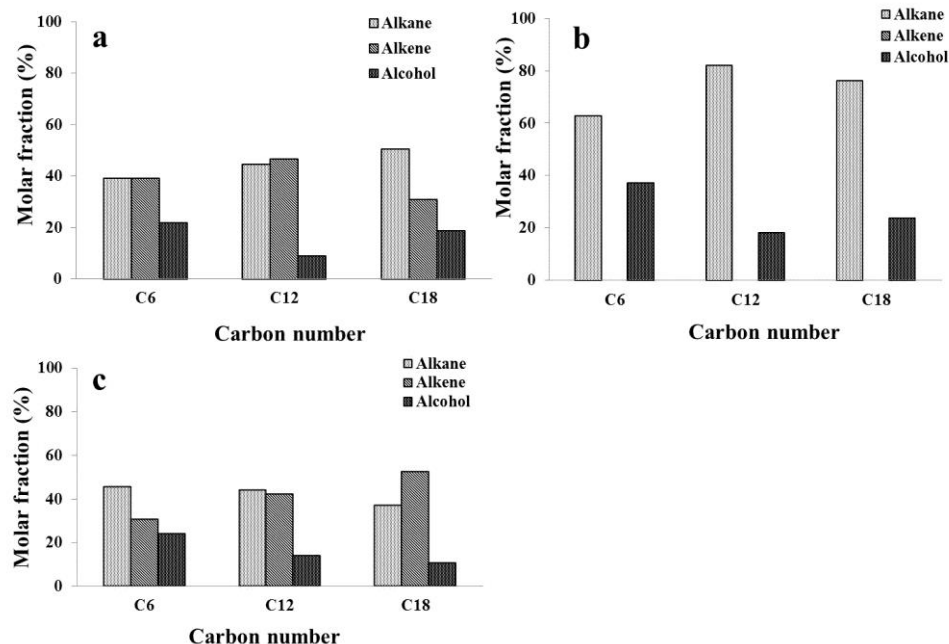
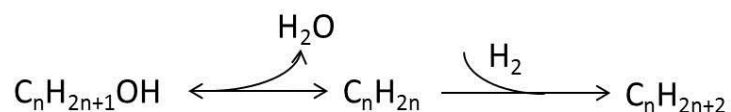


Figure 32 Alkane, alkene and alcohol fractions of C_6 , C_{12} and C_{18} products with silica-supported catalyst in water single-phase at a conversion of 80.2%: before (a) and after (b) hydrogenation, and with silica-supported catalyst in decalin single-phase at a conversion of 33.5% before hydrogenation (c).

Another important difference between the carbon-, nano-hybrid- and silica-supported catalysts is that, in the former two cases, products at high conversions were only alkanes, or at lower conversions, could be hydrogenated by H_2 at the end of the reaction into alkanes, regardless of the liquid medium being water or emulsion, as shown in Figure 21. Notice that at high conversions, the H_2 partial pressure would be much higher than CO and the H_2/CO ratio would be much higher than the initial ratio of 3.5, since FTS consumes syngas at a H_2/CO ratio of approximately 2. Therefore conditions at high conversions largely favor hydrogenation. However, in water single-phase when silica-supported catalyst was used, only alkenes can be hydrogenated into alkanes while alcohols remained, as clearly shown in Figure 32a and b. To test if this was due to the effect of catalysts of different sizes or due to different supports, products

were hydrogenated right after a run with silica-supported catalyst in decalin single-phase, and it showed that the alcoholic products were hydrogenated into alkanes (Figure 32c. Also see GC chromatograph in Appendix). Clearly, the use of silica support in water inhibited the hydrogenation of alcohol products. The hydrophilicity of the support played a critical role here. The pathway of alcohols to alkanes presumably involves dehydration to form alkenes as the first step as shown in Schematic 7. With hydrophilic support, water molecules can easily participate into the equilibrium and act as a strong force to inhibit dehydration and keep the alcohols intact. In other words, the hydrophilic surface enables the full presence of water molecules, or its chemical potential.



Schematic 7 Alcohol to alkane pathway.

2.4 Summary

FTS involving both water and organic phases seem to be a rational choice for liquid-phase operation. On one hand, as demonstrated earlier, the products can partition into different phases based on their solubility differences and thus enable easy product collection. On the other hand, an equally important advantage with the water-oil

biphasic system is the effect of water in enhancing the FTS activity, which has been well documented before but only with water vapor. This study extended the application of water into liquid zone and found dramatic decrease in selectivity to light products (gas phase) and favors selectivity toward more valuable heavy products, in addition to enhanced FTS activity, in much agreement with reported effects with water vapor. However, the same doesn't apply to water single-phase, in which similar product selectivity to organic single-phase, and faster deactivation was observed. We rationalized the observation based on the dual-site model and proposed that the use of water-oil dual liquids mediates CO dissociation rates and facilitates the equilibrium between the two sites.

The choice of support, i.e., nanohybrids, is critical. Their amphiphilic nature facilitates the formation of water-in-oil emulsion, which maximizes interfacial area between the two phases, enhances the catalyst particle dispersion and eases the mass transfer of products. The horizon of the study was extended by including supports other than nanohybrids. Although more stringent and comprehensive studies are needed for thorough comparisons, the current results pinpoint the rationale behind the choice of nanohybrid supports for the water/oil biphasic system, and the interplay between catalysts, supports and solvents. The newly proposed dual-site model was incorporated in the effort to better comprehend the observations, which also shed new light on some inconclusive issues of FTS, such as the relationship between catalyst particle sizes and their TOFs.

3. Synthesis of single-walled carbon nanotubes on planar supports and their applications

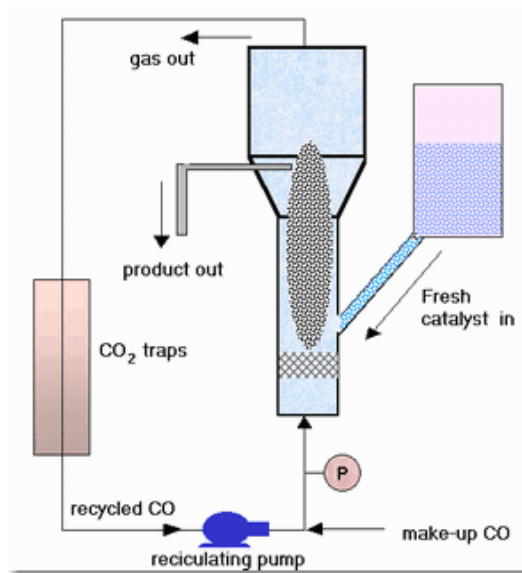
3.1 Introduction

3.1.1 Synthesis, catalysts and growth mechanisms of carbon nanotubes

Carbon nanotubes (CNTs) are cylindrically structured fullerenes. Owing to their excellent properties in electronics [164-166], mechanical strength [167,168], thermal conductivity [169-171] and hydrogen storage [172,173], experimentally or theoretically, CNTs have long been extensively studied since their official debut in 1991 [174]. Depending on the number of composing cylindrical layers, there are single-walled carbon nanotubes (SWCNTs) and multi-walled carbon nanotubes (MWCNTs). Synthesis is the first step toward CNTs research, and oftentimes proves also the foremost step in that their structures and/or compositions, and therefore, properties, are highly dependent on the conditions under which they grow. There are three major techniques for CNTs synthesis, namely, chemical vapor deposition (CVD), arc discharge and laser ablation.

CVD is a process where the volatile precursors flow through catalysts and react and/or decompose to form the desired deposits on substrates or supports carrying the catalyst. Major variants of CVD include fluidized bed and fixed bed systems. Our group has pioneered the synthesis of carbon nanotubes using fluidized bed CVD [175,176] and has successfully commercialized the process (CoMoCAT[®]). This method uses Co and Mo bimetallic catalyst and CO precursor at 700-950°C at a total pressure that typically ranges from 1 to 10 atm. CO disproportionate into CNTs and carbon dioxide. One critical condition for CNT growth was found to be high CO space velocity to keep

low CO conversion, which can be easily achieved by the tubular fluidized bed reactor, in which small catalyst particles are suspended by the upward motion of the incoming CO gas. In addition, other advantages include: thorough mixing and efficient contact between the gas and the solid catalyst particles and therefore uniform temperature distribution throughout the catalyst bed, since the catalyst particles are in constant motion within a confined region in the reactor; non-severe mass transfer limitations due to the small size of the catalyst particles, and the possibility of continuous addition and removal of solid particles from the reactor, without stopping the operation. The SWCNTs produced by CoMoCAT[®] are of high quality and with a remarkably narrow distribution of tube diameters [177].



Schematic 8 CVD CoMoCAT[®] process developed by our group (<http://www.ou.edu/engineering/nanotube/comocat.htm>)

When the flow rate is below the minimum fluidization velocity, the system becomes a fixed bed CVD. It is a more suitable set up for studying growth mechanisms and for growing CNTs on flat substrates. For this reason, a horizontal furnace is more often used for easy placement of the substrate, as shown in Figure 33. Common substrates for growing CNTs include silicon wafers [178], quartz [164] and Sapphire [179], and CNTs can be in the form of vertical forests [180] or horizontal films. In the latter case, the configurations of the film can be either aligned arrays or random tube network, depending on the interaction between the CNTs and the substrate [181]. Different from the incipient wetness impregnation method for fluidized bed, which method is commonly used to prepare supported catalysts, catalysts are casted onto the substrate through various other means, including dropping the catalyst precursor solution onto the substrate [182], dipping the substrate into the catalyst precursor solution [183], physical evaporation of metal particles onto the substrate, such as thermal evaporation [184] and e-beam evaporation [185].



Figure 33 Horizontal CVD system used in our group.

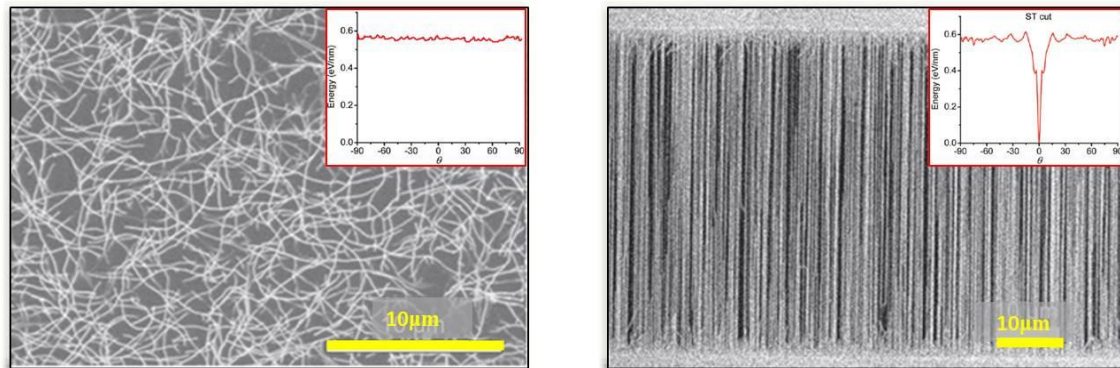
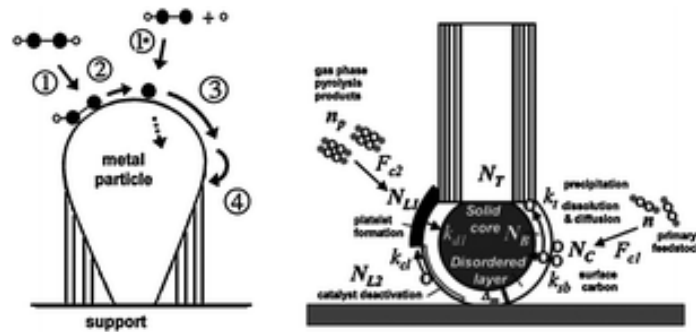


Figure 34 Random networks (a) and aligned CNT arrays (b) obtained via CVD method in this research. Inset: interaction energy profiles between CNTs and substrates, adapted from Reference 165.

Arc discharge is a technique that applies an electrical potential to two closely spaced graphite electrodes to generate a high-temperature plasma. The electrodes sublime and condense rapidly to form CNTs and other carbonaceous byproducts. Laser-ablation technique is based on similar principle, except a laser source is used to generate the heat on a carbon target.

Catalysts used for CNT growth are usually transition metals, especially cobalt [184,186,187], iron [188-192] and nickel [193,194]. These catalysts can produce either MWCNTs or SWCNTs, depending on reaction conditions and carbon feed. Bimetallic catalyst often proves more efficient for CNT production. For example, in the CoMoCAT[®] process, cobalt is the active catalyst for CO activation while molybdenum prohibits sintering of cobalt particles and therefore inhibits the formation of undesired carbonaceous species that lower the selectivity. Cobalt is reduced and stays in the metallic form during the reaction while molybdenum is converted to the carbidic form (Mo₂C).

The growth mechanism of CNTs is still an issue of debate. The most adopted theory is the vapor-solid-solid (VSS) model that has its origin in the earlier vapor-liquid-solid (VLS) model [195]. According to this model, carbon from feed decomposition precipitates on the catalyst surface, diffuses into the catalyst and nucleates as CNTs at the edges of the catalyst. Two growth models are possible, depending on the catalyst-substrate interaction. When the interaction is relatively poor, i.e., the surface energy of the substrate is lower than the that of the catalyst-substrate interface, as in the case of Fe on SiO₂, tip-growth is observed, where the catalyst particle stays at the tip of the growing CNT and moves along as the CNT continues to grow; when the interaction is relatively strong, as in the case of Fe on Ta, base-growth is observed [196].



Schematic 9 Two popular models of CNT growth mechanism: tip-growth (left, adapted from S. Hofmann, G. Csanyi, A.C. Ferrari, M.C. Payne, J. Robertson, *Phys. Rev. Lett.* 95 (2005) 3) and base-growth (right, adapted from A.A. Puretzky, D.B. Geohegan, S. Jesse, I.N. Ivanov, G. Eres, *Appl. Phys. A: Mater. Sci. Process.* 81 (2005) 223).

3.1.2 Applications of carbon nanotubes

Their excellent mechanical, electronics, thermal and energy storage properties lead to a wide range of applications where CNTs are expected to show, or are already showing great promises. For example, addition of 1wt% MWCNTs to epoxy resin can enhance its stiffness and fracture toughness by 6% and 23%, respectively [197]. The current discussion will focus on electronics properties and applications of SWCNTs, the type of CNTs that is most intriguing and is more scientifically valuable in itself, in line with the applications the efforts of this research is directed to.

The understanding of SWCNTs' electronics properties should start with that of graphene, a single atomic layer of graphite from which SWCNTs are made from, and a material that has been studied for over 50 years [198] but has been receiving extensive attention only since recently when single layered samples were isolated from graphite [199]. A SWCNT can be considered a graphene sheet being rolled up to in the form of a seamless cylinder.

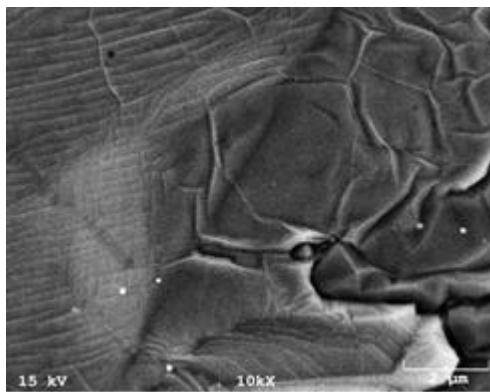


Figure 35 SEM of graphene obtained by CVD growth in this research.

Made up of sp^2 -bonded carbon atoms, graphene has a two-dimensional “honeycomb” structure (Figure 36a). A critical factor in determining its conducting properties is the nature of the electronic states near the Fermi energy, E_F , the energy of the highest occupied electronic state at the temperature of zero Kelvin (absolute zero). Figure 36b shows the energy of the electronic states as a function of their wave vector, k , near E_F . This band structure, determined by the way electrons scatter from the atoms in the crystal lattice, is different from a metal or a semiconductor. In the former, there are many states that freely propagate through the crystal at E_F ; in the latter, there is an energy gap with no electronic states near E_F due to the backscattering of electrons from the lattice. The band structure of graphene is therefore somewhere in between that of a metal and a semiconductor. In most directions (as in the Γ -M direction) in k -space, there is a band gap. In the Γ -K and five other directions that pass through the Fermi points (K-points), there is no band gap and graphene behaves as a metal.

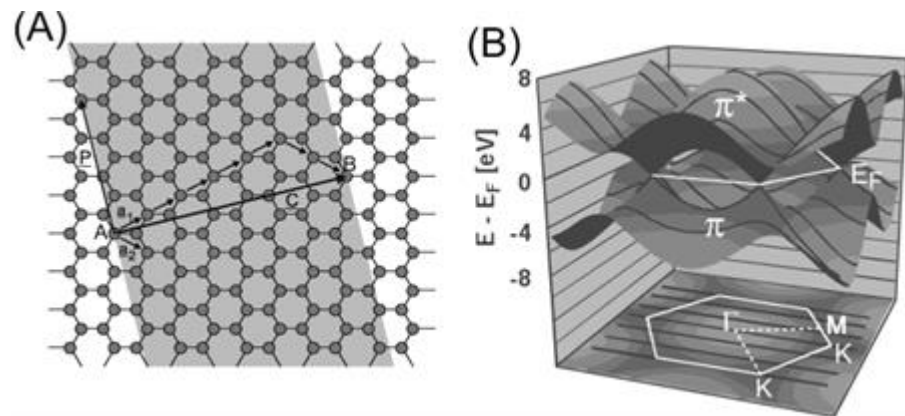


Figure 36 (A) Wrapping a graphene sheet into a CNT. The wrapping and the resulting nanotube are characterized by the chirality vector $C = na_1 + ma_2 \equiv (n,m)$, where a_1 and a_2 are the unit vectors of the hexagonal lattice. In the example shown here, point B is brought over point A, resulting in a tube with a circumference $C = 5a_1 + 2a_2$. (B) Top: Band-structure of graphene. Bottom: The first Brillouin zone of graphene. (Adapted from Reference 238).

When graphene is folded to a SWCNT, the transition from 2-D to 1-D introduces an additional confinement of electrons around the circumference, which can be expressed by the quantization condition, $k_C C = 2\pi j$, where k_C is the wave vector in the circumferential direction; C , the chirality vector; and j , an integer. Thus, j denotes a number of one-dimensional subbands split from each band of graphene. The black lines in Figure 34b shows the allowed states j of a (3,3) CNT. Two of these subbands pass through the K-point, and the tube is metallic. When no subbands pass through a K-point, the tube is semiconducting. It's been shown [200-202] that tubes are metallic when $n = m$ or $n - m = 3i$ ($i = \text{an integer}$), while semiconducting when $n - m \neq 3i$, (n, m) being the chirality vector mentioned in the caption of Figure 36b. Therefore, statistically and normally, metallic and semiconducting SWCNTs coexist at a 1:2 ratio [203].

One of the most promising applications of SWCNTs is thin conductive films, owing to the highly conductive metallic components of SWCNTs. Their excellent electrical conductivity and high optical transparency make them attractive coating materials for a large number of devices, such as light emitting diodes (LEDs), and may become a potential replacement for widely used indium tin oxide (ITO) glass. On the other hand, by making use of the semiconducting components, SWCNT films can be used to fabricate field effect transistors (FETs), an important building block for modern electronic devices.

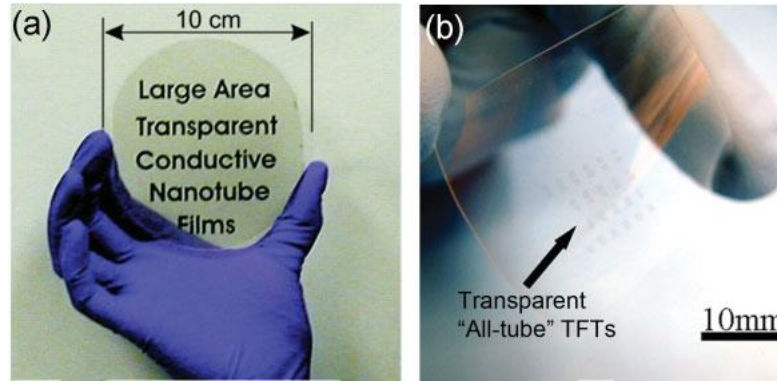


Figure 37 Optical image of a transparent, conductive SWCNT film on a sapphire substrate (a), and optical image of an array of “all-tube” flexible transparent thin film transistors (TTFTs) on a plastic substrate, with arrow indicating the S/D structures(b). (Adapted from Reference 1).

While SWCNT-based FETs can take different compositions and forms, the basic configurations are the same and are a reflection of the FET working mechanisms. Two metal electrodes designated as “source” and “drain” are connected by a semiconducting channel, which is a semiconducting SWCNT (s-SWCNT) in place of Si in conventional devices. A third, “gate” electrode is separated from the channel by a thin insulating film. While the conductivity of s-SWCNTs intrinsically originates from electrons (n-type), under atmospheric circumstances, interaction with oxygen makes them deplete of electrons, leaving holes as the charge carriers (p-type). A negative bias to the gate electrode induces holes on the s-SWCNT and makes it conduct, and a positive bias depletes the holes and decreases the conductance.

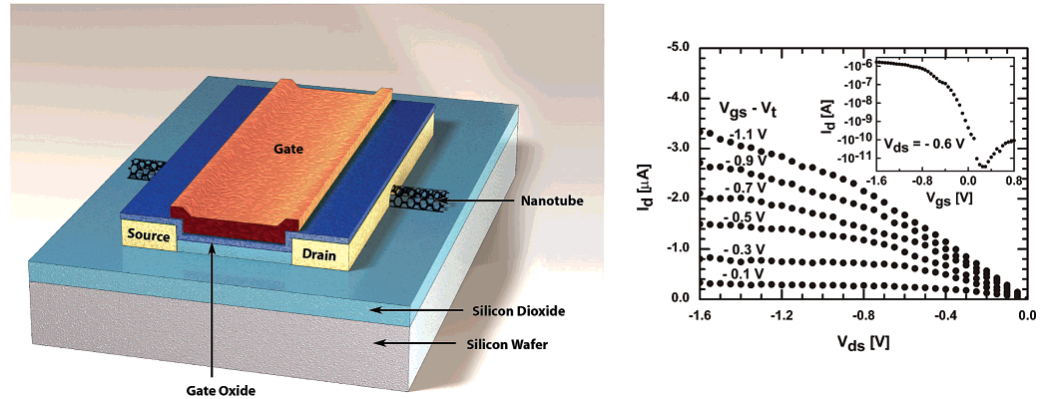


Figure 38 Schematic structure of a top-gated CNTFET (left) and output electrical characteristics of a top-gated CNTFET (right). (Adapted from Reference 238).

3.1.3 Objectives of this study

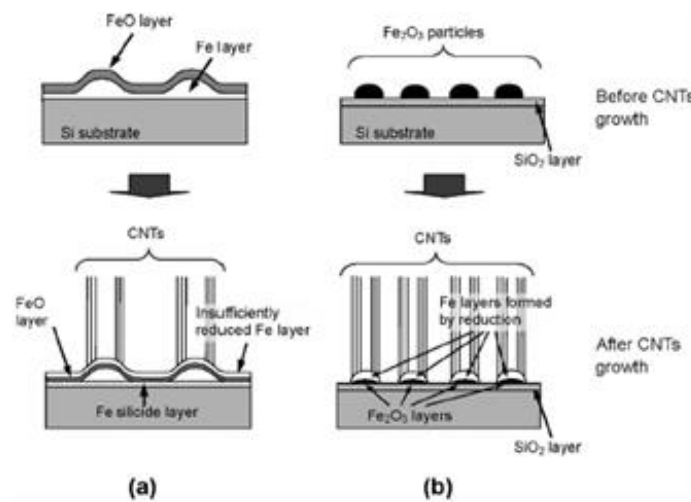
It is well known that SWCNTs possess excellent charge transfer properties and unique mechanical properties, making them promising candidates for advanced applications in electronics, including field effects transistors, thin film electrodes, flexible circuits, and bio-sensors [164-166]. In order to realize the advantages that SWCNTs present, they must be integrated into the device construction at high densities without losing the intrinsic properties of the individual nanotube. Efforts to make ultra-thin films from SWCNTs produced by chemical vapor deposition (CVD) have been ongoing for some time. Those efforts have produced a variety of methods including Langmuir-Blodgett, layer by layer deposition, and spin casting [204,205]. Horizontally aligned SWCNTs (HA-SWCNTs) present another route towards integrating nanotubes into devices by utilizing the crystal structure of the substrate to perfectly align the nanotubes. HA-SWCNTs have been grown on a variety of substrates (ST-cut quartz [164], Silicon Oxide [206], and R-cut Safire [207]) using chemical vapor deposition (CVD) with a variety of conditions and catalysts [208-211]. The resulting films can be

produced with uniform densities across a whole wafer for integration into active devices using a lift off transfer techniques [212]. In order to further enhance the properties (current density, sensor sensitivity, and conductance) of the devices made from HA-SWCNTs the linear density of nanotubes must be increased. Such efforts have been underway to further increase the capacity of devices, e.g., double growth CVD and sequential depositions [213]. A more rudimentary method to increase the tube density is to reduce the distance between parallel catalyst lines to utilize the typically higher density near the catalyst edge.

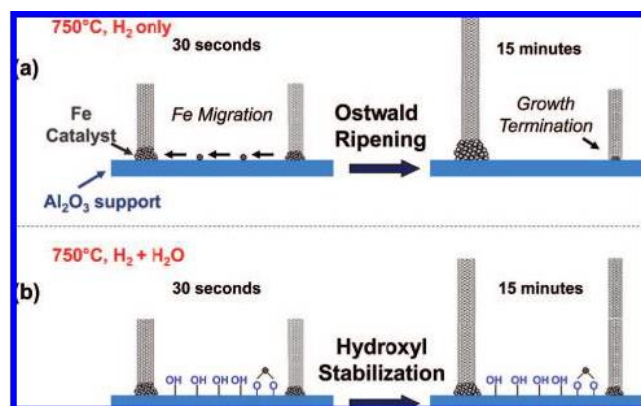
In those reports for CVD synthesis of HA-SWCNTs, iron was used as catalyst and methane was used as carbon feed source. In the following efforts, ethanol is used as the carbon feed source, which proved to give equal or even better results [213,181]. In some other contributions where ethanol was used, a small amount of water was added. For example, Qian et al. reported superlong-oriented SWCNT arrays grown from ethanol mixed with 1-3% of water with Fe-Mo nanoparticles as the catalysts [214]. Meanwhile, the incorporation of water into the growth of SWCNT forests or carpets has been shown a success [180], and various enhancement mechanisms of water have been proposed, including water induced oxidation of catalyst surface to prevent iron silicification [215], inhibition of the Ostwald ripening of the catalyst [216], and etching of coating carbon around catalyst particles [217].

While it seems that the growth of super long SWCNT arrays was a successful incorporation of the water enhancement effects as demonstrated in the cases of forests or carpets, reports are rare that explain how water improves the growth of aligned SWCNTs on substrates [217], which is to be addressed in the first part of this research

as we optimize the growth efficiency by adjusting water content. So far, using iron as catalyst, we have grown HA-SWCNT arrays on ST-cut quartz using pure ethanol and ethanol mixed with different contents of water as carbon feed. Scanning electron microscope (SEM) and atomic force microscope (AFM) were used to characterize the samples. By comparing the samples obtained with different water contents, we show that the addition of water up to a certain amount improved the growth efficiency. On the other hand, too much water caused elimination of SWCNTs and resulted in a decreased tube density. To better illustrate the role of water, reactions with ethanol mixed with 3% of water, 1% of water and pure water were carried out on the same sample successively. The preliminary results provide further evidence for the carbon etching mechanism, and serve to construct the guideline of water-assisted growth of SWCNTs on substrates. Greater enrichment in tube densities is possible once the enhancement mechanism is fully understood.



Schematic 10 Prevention of iron silicification for CNT growth (from H. Sato, Y. Hori, K. Hata, K. Seko, H. Nakahara, Y. Saito, *J. Appl. Phys.* 100 (2006) 104321).



Schematic 11 Inhibition of Ostwald ripening through the ability of oxygen and hydroxyl species to reduce diffusion or migration rates of catalyst atoms on the substrate (from Reference 216).

Inspired by the results from the first part, we went on with ethanol-water blends as the carbon feed and tested other conditions in an effort to synthesize conductive SWCNT films with ultra-high transparencies.

As mentioned earlier, SWCNT films possess excellent electrical conductivity and high optical transparency, making them a potential replacement for widely used indium tin oxide (ITO) glass. Albeit widely used today for transparent conducting electrodes (TCEs), ITO has significant limitations for current and future opto-electronic applications, not only because it is optically, electronically, and chemically problematic [218], but also the availability of Indium is questionable and therefore expensive. Consequently, research related to the fabrication of SWCNT TCEs has received extensive attention. In the majority of the reported methods, carbon nanotubes are prepared ex-situ and transferred to a substrate as a suspension [219-225]. In general, the as-synthesized SWCNTs are post-treated in order to purify the nanotubes and facilitate the application of the suspension onto the substrate by different techniques,

including transfer printing [219,220], filtration [221,222], spray [223], dip-coating [224], and drop casting [225]. Typically, the post-treatment that produces the suspension includes sonication, acid or caustic attack, use of a surfactant, etc. Most of these methods have a negative impact on film performance. Acid or caustic attack and sonication may cut the nanotubes and introduce defects. External surfactants or dispersant are also be detrimental to conductivity. They are difficult to remove completely and their presence incorporates an electrical barrier that increases the contact resistance between nanotubes, increasing the resistance of the network.

In addition, the as-synthesized SWCNTs are often in the form of bundles and typical post-treatment methods are not effective in de-bundling them. As discussed below, bundling further limits film conductivity and, as a result, it is difficult to produce thin SWCNT films with low sheet resistance [226]. Moreover, in some applications of TCEs, such as display panels, ultra-high transparency is a more desirable feature than conductivity. But these methods cannot produce films of such high transparency. Therefore, the methods are highly desirable that can simultaneously reduce sheet resistance and maximize transparency into the ultra-high region (i.e. > 98%).

While growth of horizontally orientated SWCNT arrays grown on flat substrates by chemical vapor deposition (CVD) has been recently reported [210,227-229], the use of these arrays in TCEs is limited by the anisotropic electrical properties caused by their particular morphology [230,231]. Isotropic thin films appear as a more suitable structure to maximize conductivity at high transparency.

Iron can be effective in catalyzing the selective growth of SWCNT [232]. A common protein, ferritin has been widely used as catalyst precursor, which can be

conveniently applied onto substrates by dipping [233] or spin-coating [234]. Previous efforts on SWCNTs synthesis involving ferritin include either growing SWCNT arrays on substrates such as ST-cut quartz and sapphire [229,235,236], which result in electrical anisotropy as discussed earlier, or discrete SWCNTs [233,234], which were not continuous enough to form conducting networks. Recently, two-dimensional networks have been grown using ferritin as the catalyst precursor [237]. However, they were formed on non-transparent silicon substrates, so no optical transmittance test was conducted. In addition, the reported sheet resistance was as high as 770 k Ω /square. We have found that ferritin is an effective catalyst precursor when combined with water-doped ethanol as carbon feed. Under these conditions, conductive SWCNT films with ultra-high transparency on transparent quartz substrates have been successfully synthesized. To optimize the film performance, the effects of catalyst annealing and concentration were studied. Scanning electron microscope (SEM) and Raman spectroscopy were used to characterize the SWCNT films. The optoelectronic performance of the films was monitored by measuring the sheet resistance and optical transmittance on the same samples.

In addition to the excellent optoelectronic properties that points to promising applications in TCEs, we have developed a method that combines inkjet- and transfer-printing to fabricate FETs using the SWCNT films, which not only further showcases the potential applications of the SWCNT films in FETs, but also is a novel and noteworthy FET fabrication technique by itself. Graphene synthesized in our lab was also used via this technique with success.

Carbon-based nanoelectronics has received extensive attention over the past decade largely due to the outstanding electrical properties of SWCNTs [238], and more recently, the demonstration of even better performance of graphene in certain aspects, such as carrier mobility [239-241], along with the development of CVD method to produce it in higher quality and larger scale [242]. Thin film transistors (TFTs), the primary building units for many devices such as liquid crystal display, is one of the areas where carbon nanomaterials have shown their promises as the functioning building blocks. Deposition of a corresponding suspension is one way to make thin films toward that goal. The thus obtained films, however, are not ideal for device applications. For example, the as-synthesized SWCNTs are post-treated in order to be purified and facilitate the application of the suspension onto the substrate. Sonication, acid or caustic attack, use of a surfactant, etc. are usually involved and they have a negative impact on film performance due to introduced defects on nanotubes and added electrical barriers between nanotubes. In comparison, in-situ synthesized, bundle-free SWCNT networks don't have these limitations and have shown electrical properties superior to their counterparts from suspensions [243]. Analogically, graphene grown on metal substrates via CVD method has much fewer defects than that from graphene oxide reduction [244-246] and overcomes the size limitation of graphite exfoliation method [247].

In following fabrication procedures, a transfer step is required to place the surface-grown materials from their source substrate onto the substrate of the device (target substrate). This is especially true when it comes to flexible TFTs, where the flexible polymer substrate does not provide the smooth surface for the semiconducting material

to grow on, nor can it withstand the high temperature during the growth process. Conventional transfer methods rely on a combinatorial use of gold deposition, thermal releasing tape and polydimethylsiloxane (PDMS) stamps [248]. More recently, poly(methyl methacrylate) (PMMA) has become a widely used transfer mediator for carbon nanotubes [249] and graphene [250] due to its ease of use and high reliability. In this method, a PMMA solution is spin coated onto the source substrate and cured, followed by partial etching of the source substrate in a basic solution to detach the PMMA/nanomaterial layer in water. The floating film is then laid over the target substrate and acetone is used to dissolve the PMMA. Meanwhile, with a dielectric constant range of 2.5–3.5 [251,252], PMMA is among the few polymeric materials used as gate dielectric [250,253-255]. Yet to our knowledge, its usage has been limited to organic TFTs (OTFTs), mainly with pentacene as the semiconducting material [250,251,254,256].

Conventional photolithography and e-beam/thermal evaporator are well established tools for the deposition of electrodes [257]. For gate dielectric deposition, spin casting or atomic layer deposition (ALD) is usually used. Inkjet printing provides a cost-effective alternative that circumvents the complexity of the above approaches, and enables mass production of large-area electronic circuits [258], which, along with its low temperature processability, makes it a technique especially promising for flexible electronics.

We present a novel and facile method to fabricate flexible thin film transistors of carbon nanotubes and graphene that incorporates PMMA-transfer and inkjet printing. The nexus between the two procedures, and the most unique part of this method, is the

multifold function that the PMMA has: instead of being removed after landing on the target substrate, the transfer mediator stays and serves as gate dielectric. In addition, it can be a protective encapsulation for SWCNTs/graphene against p-doping in air, making it possible to achieve air-stable n-type devices. As proof-of-concept, we show preliminary measurement results that are comparable to those from devices of same types of materials that are structurally similar (e.g., similar nanotube network density/coverage) but fabricated using more conventional methods. The PMMA functions well as the dielectric layer even at relatively large currents.

3.2 Experimental

3.2.1 Surface-guided growth of horizontally aligned SWCNTs on quartz

The HA-SWCNTs were grown on ST-cut single crystal quartz wafers (Hoffmann Materials). First the wafers were cut into 1.6 cm x 0.8 cm pieces and then annealed at 800°C for 8 hours. Using photolithography, well defined Fe stripes of 0.3 nm in thickness were deposited via thermal evaporation (Edwards thermal evaporator). The substrates were then annealed at 900°C in air to form iron oxide nanoparticles.

To grow HA-SWCNTs, the substrates were heated in a furnace (Lindberg/Blue) to 925°C in H₂. During growth a mixture of Ar and H₂ (3:1, 35 sccm in total) flowed over the sample with ethanol (pure or premixed with a small amount of water) either with Ar and H₂ going through a bubbler or injected with a syringe pump at rate of 0.27 ml/h for 20 min. The HA-SWNTs were characterized using SEM (Zeiss 960) and AFM (Nanoscope III and Topometrix). It should be noted that although traditional SEM can observe the nanotubes effectively it cannot distinguish tube diameter or two tubes lying close together due to the relatively large beam widths compared to the typical nanotube

diameter (sub nm to 5 nm as measured by AFM). Thus all linear densities derived from SEMs constitute a minimum of the measurement.

3.2.2 Growth of conductive SWCNT films with ultra-high transparency

Transparent quartz substrates were washed thoroughly with soap and dipped in piranha solution (i.e., one part of hydrogen peroxide in three parts of sulphuric acid) for 15 min at room temperature. After this treatment the samples were rinsed with acetone and isopropanol and blown-dried with nitrogen. Ferritin (Type I, saline solution, Sigma-Aldrich) was diluted in distilled water by 10, 30 or 200 times to achieve iron concentrations of 100mM, 33mM and 5mM (indicated below as C100, C33 and C5). The solution was spin-coated onto the quartz substrate on a spinner (Laurell WS-400-6NPP-LITE) at 5000 rpm for 10 sec. The substrate was then dried in a vacuum oven at 90°C for two hours and annealed in air at 900°C for 0, 10, 20, 30, 45 or 60 min (indicated below as A0, A10, A20, A30, A45 and A60). Growth of SWCNT films on the quartz/catalyst substrate was carried out in a horizontal furnace (Lindberg/Blue). In each run, the substrate was placed at the center of a one-inch tube reactor and heated up to 925°C in H₂. Then, ethanol mixed with 0.5% of water was injected at a rate of 0.30 ml/h along with Ar and H₂ (35 sccm total flow, ~ 3:1 molar ratio) for 20 to 30 min. We identify the samples used in this study with the notation C_x-A_y-R_z, where x is the ferritin concentration in mM, y is the annealing time in minutes, and z is the reaction time in minutes.

Sheet resistances were measured on a test meter (JANDEL HM20). Current-voltage measurement was conducted using a Keithley SourceMeter (2410) with probes

applying onto silver electrodes (Ted Pella) on two ends of the SWCNT film. Transmittance spectra were obtained on a Shimadzu UV-Vis spectrophotometer (UV-2450). Raman spectra were acquired on a Jovin Yvon-Horiba Lab Ram equipped with a charge-coupled detector and a He-Ne laser (632 nm) as excitation source. SEM analysis was carried out on a FEI Quanta 600 field-emission gun environmental scanning electron microscope.

3.2.3 Synthesis of graphene

Copper foil 0.05 mm thick (Alfa Aesar, Puratronic) was hand-polished and placed inside the same reactor as above. The reactor was then heated up to 800°C in a mixture of 10 sccm H₂ and 600 sccm Ar. After staying at this temperature for 15 min, the temperature was brought up to 1000 °C and methane was introduced at 30 sccm. The reaction lasted for 15 min before cooling down to room temperature in Ar.

3.2.4 Fabrication of thin film transistors and device measurements

Two types of source substrates were prepared: SWCNT films grown on quartz glass and graphene grown on copper foils. Electrodes were printed on the target polyethylene terephthalate (PET) substrate using silver ink (InkTec, TEC-IJ-010) and a materials deposition system (Dimatix DMP-2831, nominal drop volume of 1pL and drop spacing of 20 μm). Prior to printing, the substrates were treated with corona treater (ETP, BD-20AC) to enhance ink wettability. From this point, our TFT assembly strategy involves three major steps (Figure 56a): integrating SWCNTs or graphene onto PMMA, detaching the PMMA/SWCNT or PMMA/graphene layer and loading it onto

the target substrate, and printing the gate electrode. The PMMA/SWCNT and PMMA/graphene layers were obtained following established protocols starting with spin coating a PMMA solution (950 PMMA C4, MicroChem) onto the source substrate [242,248], which eventually resulted in a transparent film floating on water. The target substrate bearing source and drain electrodes then reached into water to allow the attachment of the PMMA film. After drying the target substrate in vacuum oven, the gate electrode was printed on top of the PMMA. The target substrate was subject to a 180°C oven baking for 10 min after each printing in order to cure the electrodes. The electrode patterns were designed on ACE Translator 3000 software, which then converted the design to a printer-recognizable format. A typical pattern consists of three silver bars 10 mm long and 0.5 mm wide as source, drain and gate, each with a 1.5 mm x 1.5 mm square pad at one end for easy contact with measuring probes.

Devices measurements were conducted on a probe station (Signatone) connected with two Keithley SourceMeters (2400 series) providing source-drain and source-gate voltages, respectively. Specific contact resistance was calculated using transmission-line-model [259].

3.3 Results and discussion

3.3.1 Surface-guided growth of horizontally aligned SWCNTs on quartz

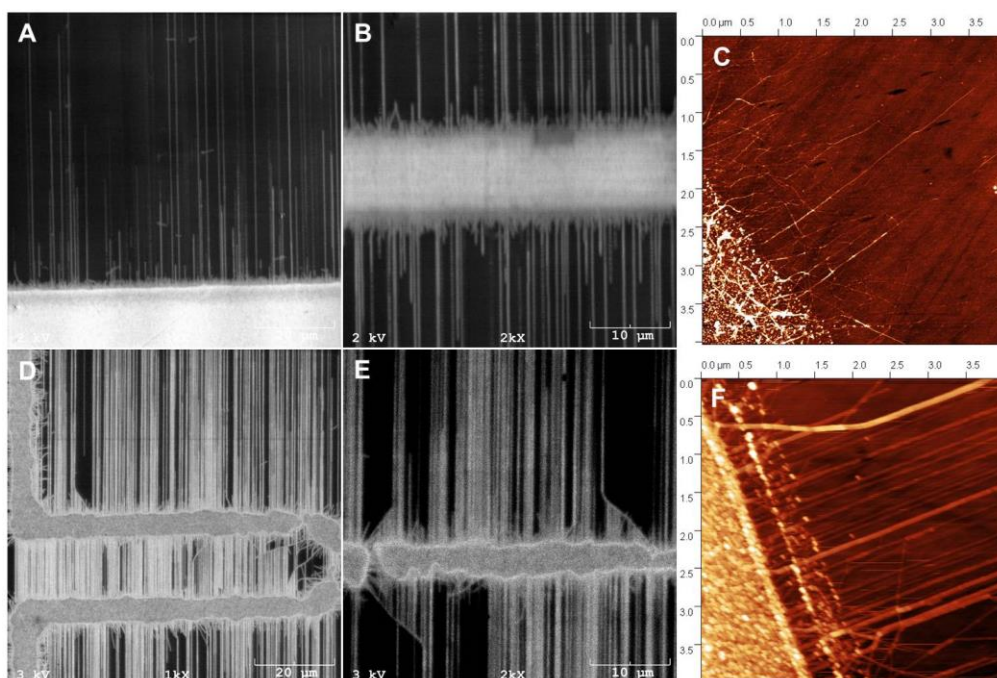


Figure 39 SEM images of HA-SWCNTs grown with pure ethanol (A and B) and AFM image (C); corresponding images with 1% of water mixed with ethanol in the bubbler (D, E and F).

Figure 39 shows the results of HA-SWCNTs grown with pure ethanol (A-C) and with 1% of water mixed with ethanol in the bubbler (D-F) (denoted as B0 and B1). Without water, the SWCNTs appear relatively sparse with many short, small diameter, and disordered nanotube “hairs” present at the catalyst edge (Figure 39 B & C). With 1% of water, the SWCNTs appear much denser, which is further demonstrated at higher magnifications in Figure 39, and fewer “hairs” are observed at the edge (Figure 39 D, E and F). These observations led us to a preliminary conclusion at this point that it was the small disordered nanotubes that stopped further growth of SWCNTs and decreased the tube density. In B1, some “hairs” showed up at a later stage of the growth and in the form of what we call “hockey sticks” (Figure 41), which are long nanotubes that deviated and went across their normal growth direction. As can be seen from the SEM

and AFM images, most aligned nanotubes stopped where they meet the “hockey sticks”, indicating a tube-tube interaction termination mechanism.

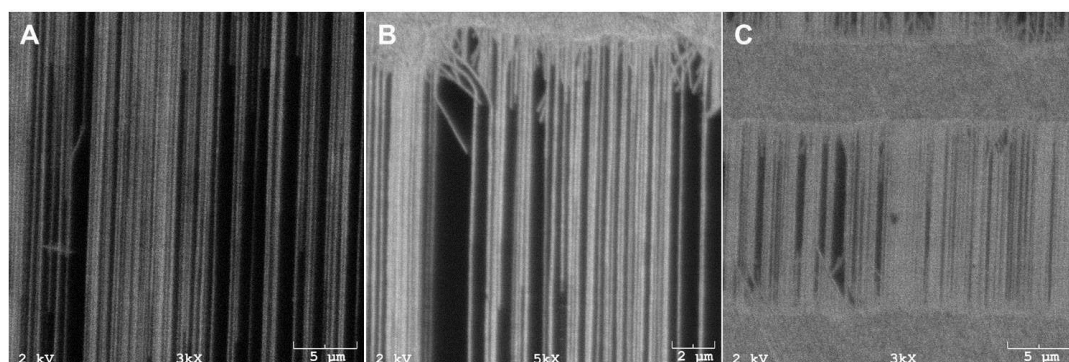


Figure 40 SEM images of HA-SWCNTs grown with bubbler with ethanol mixed with 1% of water, showing high density.

The above difference observed prompted us to look further into the effects of water. To obtain an easier control over ethanol injection rate as well as water content, we replaced the bubbler with a syringe pump, since it is more reliable to vary the concentration in solution rather than depending on the uniformity of the bubble formation (and thus water content) in the bubbler.

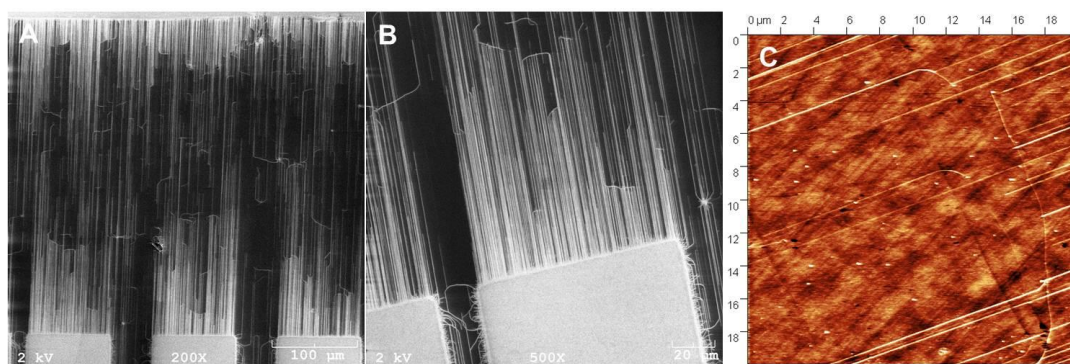


Figure 41 SEM and AFM images showing the hockey stick termination of tube growth.

Figure 42 shows the SEM images of the HA-SWCNT arrays grown with ethanol mixed with water contents of 0 and 1% (denoted as S0 and S1). With pure ethanol (Figure 42 A and C), many “hockey sticks” were observed. Some SWCNTs were not long enough and failed to bridge the gap between two catalyst bars. Besides, a considerable portion of void substrate surface deplete of SWCNTs was observed. We estimated the average tube density on this sample to be around 4 per μm . In S1 (Figure 42 B and D), hockey sticks were seldom seen, and the substrate surface was covered with long and dense SWCNTs. A density of around 6/ μm was estimated here. When we increased water content to 3% (Figure 43 A) and 5% (Figure 43 B) (S3 and S5), however, degeneration was observed. While both samples showed straight and aligned tubes, their qualities dropped dramatically: many short tubes protruded along the catalyst bars, and tube densities were only under 1/ μm for S3 and lower for S5.

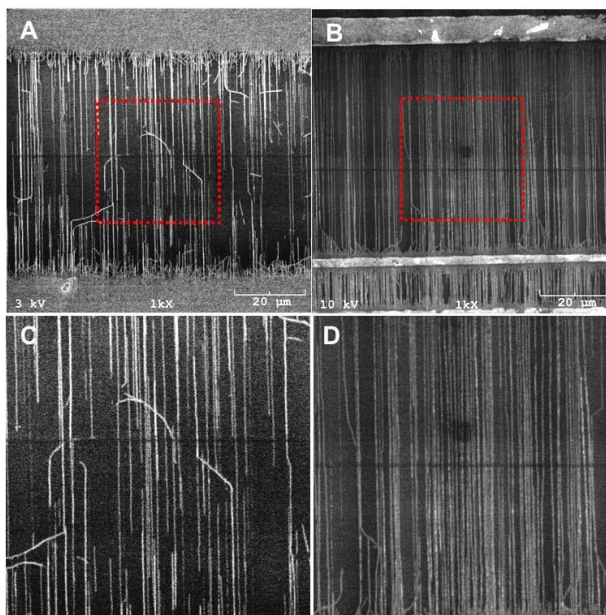


Figure 42 SEM images of HA-SWCNTs grown with pure ethanol (A) and the zoom-in view of the center part (C); with ethanol and 1% of water (B) and the zoom-in view of the center part (D).

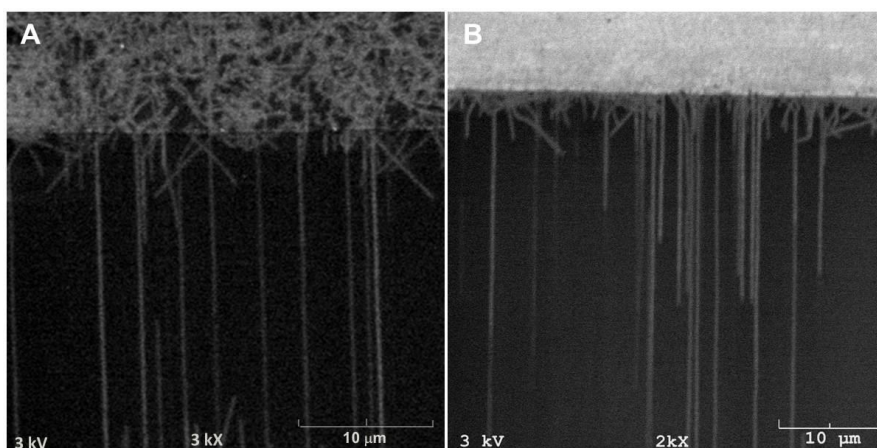


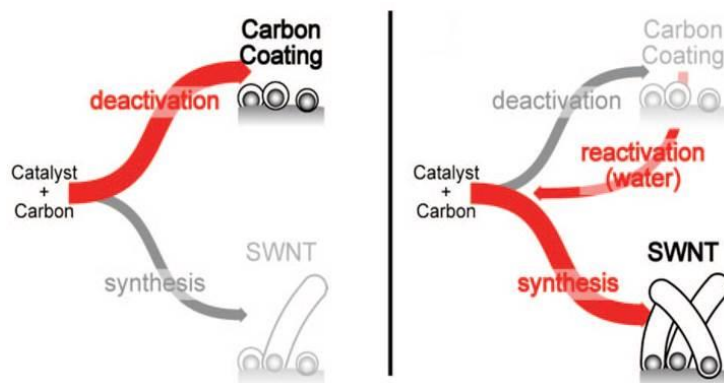
Figure 43 SEM images of HA-SWCNTs grown with ethanol and 3% of water (A); with ethanol and 5% of water (B).

The fact that ethanol has been more employed than methane in the growth of SWCNTs on substrates and shown better results serves as an implication of the water

effects in the first place, since water is known as a thermal decomposition product of ethanol, although that the decomposition of ethanol is much easier than that of methane could be another consideration. In this study, the comparison between samples from reactions of different water contents presents straightforward demonstration of the water effects as a double-sided sword: a small content of water (1% in our case) promotes the growth of SWCNTs on the substrates, while excessive water demotes it. We believe that both the positive and negative effects derive from the etching of carbon by water, which can be simply depicted by the following equation [215]:



Carbon coating over catalyst has been believed to contribute to the termination of SWCNT growth [217]. In the presence of abundant amount of water; carbon coating was promptly etched away, leaving catalyst particles active for continuous deposition of carbon atoms that were built into carbon nanotubes. On the other hand, excessive amount of water not only etched away the carbon coating but also the carbon nanotubes themselves. The net effect, as a result, was a water content (around 1% in our case, as we can see) at which the highest growth efficiency was achieved. This corresponds well to the case of water-assisted growth of SWCNT forests, where it has been shown that the growth efficiency maximizes at a certain water/carbon source ratio [260].



Schematic 12 Reactivation of catalyst by hydrothermal effect of water (adapted from Reference 199).

Interpretation of “hockey sticks” brings us more insight into the mechanism. Similar observation has been reported [261], where the bent structures were named “sickles”. The authors suggested that the nanotubes were grown by tip-growth, and the alignment was due to catalyst particle-substrate interaction. As the growth proceeded, the nanoparticles on the tips of the nanotubes collided with each other, forming larger nanoparticles that no longer energetically favored a certain direction on the substrate along which they slid. While we agree on the tip-growth mechanism, as it can conveniently explain our observation as discussed later, the idea of particle collision doesn’t quite fit into the context of nanotube-substrate interaction. Moreover, it was not supported by our observation that adding more water resulted in fewer hockey sticks. Here we propose that the hockey sticks were caused by excessive carbon deposition either on catalyst particles or on the tip of carbon nanotubes. When catalyst particles were coated with carbon, conceivably, incoming carbon atoms would not deposit in the way they would on clean catalyst particles to form ordinary nanotube structures. As a result, defects were formed that shaped the morphology of the nanotube with a curvature. When the second scenario occurred in which, probably due to very high

activity of the catalyst nanoparticle, excessive amount of carbon atoms were deposited on the tip of the nanotube but would not be built into the nanotube wall, the nanotube-substrate interaction was interrupted by the attached amorphous carbon and the energetically favorable direction was no longer the same. The nanotube ended up growing along another direction. In either case, excessive carbon was accumulated enough to terminate nanotube growth eventually, which probably serves as a more dominant termination mechanism especially in S1, where no pronounced tube-tube interaction termination was observed. When water was introduced into the reaction below a certain percentage, the unwanted carbon was etched away before it could curve the nanotubes, and thus straighter, longer and denser HA-SWCNT films are obtained. In the case of B0, carbon contamination was so instant that without additional water input the “hockey sticks” formed right at the catalyst edge and ran into each other very soon due to the high tube density at the catalyst edge that they took the form of short “hairs”.

Also noticeable is that compared to B series, water seemed to played a more active role in S in that it seems there was a water effects “up-shift” in S relative to B. For example, water as a thermal decomposition product of ethanol in S0 showed its effects as what the additional water did in B1. This is conceivable since the two injection methods could result in quite different water input rates.

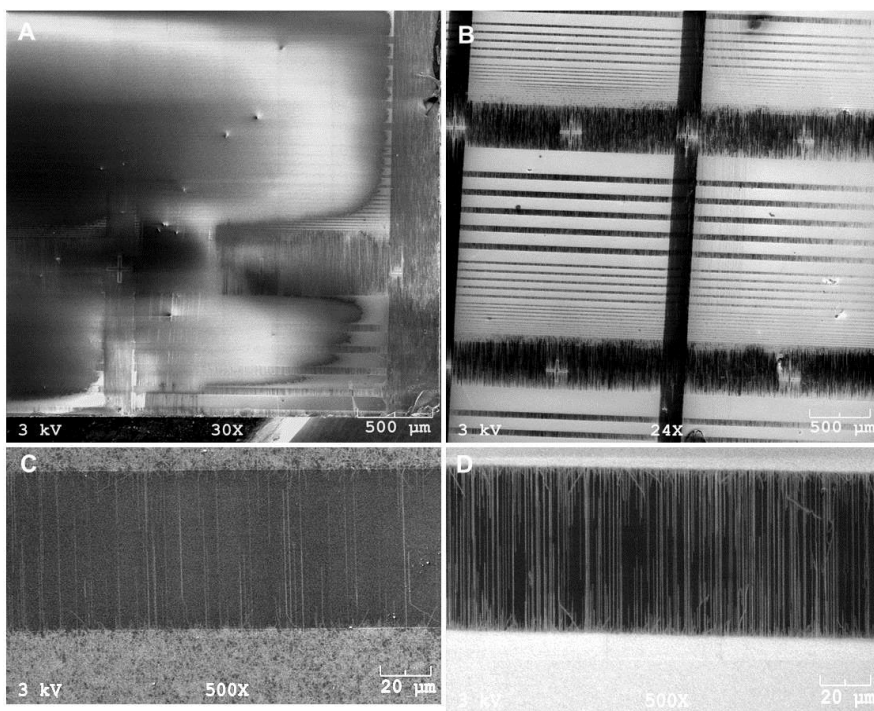


Figure 44 SEM images of samples grown with ethanol and 3% of water (A) and the zoom in view (C); re-grown with ethanol and 1% of water (B) and the zoom-in view (D).

To further verify the etching mechanism of water, reactions with ethanol mixed with 3% of water, 1% of water and pure water on the same sample were conducted successively. For the experiment with 1% of water, the sample was first annealed at 900°C in air to burn off SWCNTs grown with ethanol-water (3%) mixture. Then it was processed in the furnace following the procedures in the experimental part. After SEM characterization, the sample was put into the furnace without annealing, and the reaction was carried out at a water injection rate of 0.03 ml/h for 5 min, with the other steps the same. The results with 3% of water were similar as shown before, where there were loose SWCNT arrays on the substrate (Figure 44 A and C). The density of SWCNTs was dramatically increased with 1% of water introduced (Figure 44 B and D). Dense SWCNT mats were grown on the catalyst bars, making the catalyst patterns visible with

high contrast. This further reduces the role of Ostwald ripening, which is not a reversible process as we see here. It is interesting to see what happened after pure water injection (Figure 45). We notice that the tube density between the catalyst bars were not decreased by much, while the visibility of the catalyst patterns dropped again, indicating drastic elimination of the SWCNT mats on the catalyst bars. The preservation of nanotubes in the catalyst gaps suggests that water preferentially reacted with carbon on catalyst, indicating that the carbon etching by water is catalytic. This lends us a hint when we reexamine the two scenarios we proposed in explaining the hockey sticks and leads to more confidence in the first one, i.e., water acted to etch away carbon coating on catalyst nanoparticles to revive their catalytic activity. This conclusion is also supported by preceding studies [217].

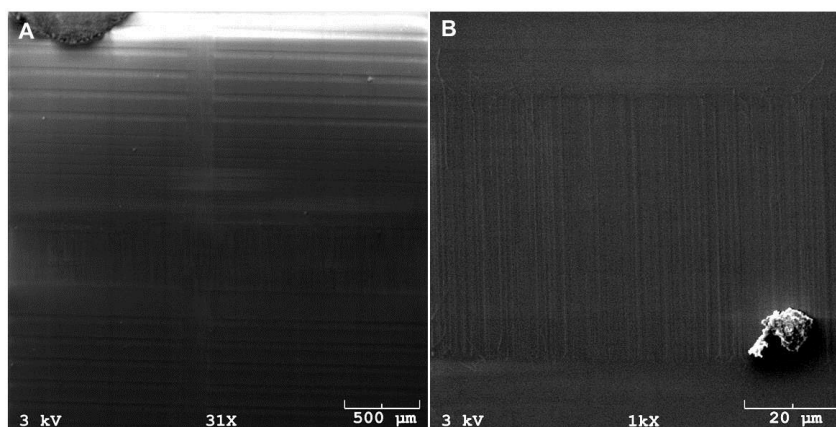


Figure 45 SEM images of samples after water injection for 5 min.

3.3.2 Growth of conductive SWCNT films with ultra-high transparency

3.3.2.1 SWCNT film general characteristics



Figure 46 Optical photo showing quartz substrates without (left) and with a SWCNT film (right). The black dot on the bottom left corner of the right substrate was used as a marker for the side with the film.

Figure 46 shows a photograph of one typical transparent SWCNT film thus synthesized (in this case, C33-A60-R30). The SWCNT film exhibited a sheet resistance of 7.1 k Ω /sq and transmittance of 98.4% at 550 nm wavelength. Its dc electrical conductivity was calculated to be around 3.9 x 10⁴ S/m, which is superior considering its ultra-high transparency [262,263], and twice as high as pure bulky paper [264]. Dc electrical conductivity (σ_{dc}) was calculated using the equation:

$$\sigma_{dc} = \frac{Gl}{tw}$$

where G is the electrical conductance obtained from the slope of the I-V curve, l is the distance between two electrodes, t and w are the thickness and width of the SWCNT film, respectively.

As seen in the image, the substrate with the SWCNT film (right) displays a transparency hardly distinguishable from that of the plain substrate (left), which had a transmittance of 99.5 %. The SEM images for this sample are shown in Figure 47. The low-magnification SEM image (Figure 47A) demonstrates the uniformity of the film. The higher-magnification images (Figure 47B and 47C) reveal that the film is composed of essentially unbundled and long nanotubes that interconnect and form a continuous network. It is worth noting that, at the acceleration voltage (20 kV) used for all the SEM observations, no charging effects was observed, indicating a high electrical conductivity of the film.

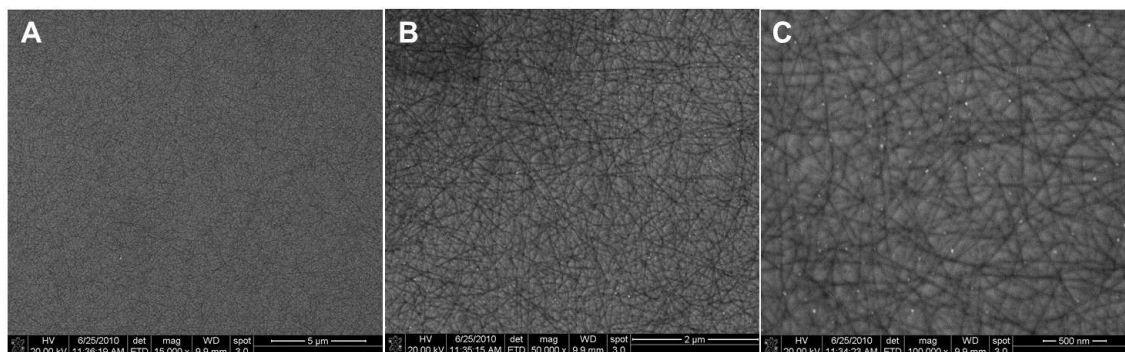


Figure 47 SEM images of the SWCNT film at magnifications of $\times 15\,000$ (A), $\times 50\,000$ (B) and $\times 100\,000$ (C).

The observed uniformity of the films can be largely attributed to a uniform distribution of the Fe catalyst clusters as a result of the piranha pretreatment of the surface that renders the substrate highly hydrophilic, and the high spinning speed (5,000 rpm) used in the spin-coating step. The long nanotube length and individuality (i.e., no bundling) are in sharp contrast to those typically observed in films made from solution, in which the nanotubes have been shortened to get dispersed, but tend to form bundles

as they dry from the suspension [225]. Theoretical and experimental studies have shown that long and individual SWCNT have a significant advantage in generating films of high conductivity [219,265-267]. It has been demonstrated that the film resistance is largely dominated by the resistance of the nanotube-nanotube contacts [268]. Therefore, the fewer junctions in the film, the higher is the overall conductivity.

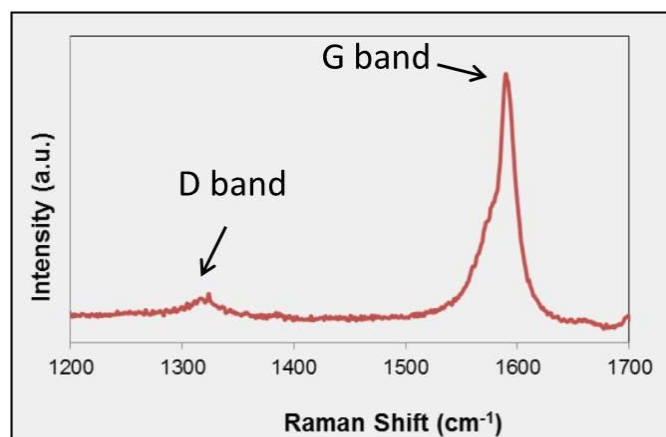


Figure 48 Raman spectrum of the SWCNT showing the D and G band.

The Raman spectrum for this sample (Figure 48) shows that the intensity ratio between the G band (ca 1582 cm⁻¹, signature of a sp² carbon structure) and the D band (ca 1350 cm⁻¹, due to disordered carbon) is high (~16) and indicative of low defect concentration in the nanotube and an overall good quality. And, most importantly, such a high G/D ratio is indicative of SWCNTs rather than MWCNTs (multi-wall carbon nanotubes). The radial breathing mode (RBM) could not be seen due to the strong scattering appearing in this region from the quartz substrate [235].

3.3.2.2 Effects of catalyst annealing

In this comparison, we used a C33 ferritin solution and 20 min reaction time while varying the annealing time. The results are summarized in Figure 4. It can be observed that the sheet resistance generally decreases with increased annealing time, from above measurement range of the test meter ($\sim 1 \text{ } \Omega/\text{sq}$ - $\sim 10 \text{ M}\Omega/\text{sq}$) with no annealing to $12.6 \text{ k}\Omega/\text{sq}$ at 60 min. At the same time, the transmittance at 550 nm is seen to gradually and slowly decrease with annealing time from 99.6% at 10 min to 99.3% at 60 min. Interestingly, without annealing, the observed optical transmittance was even lower than with annealing.

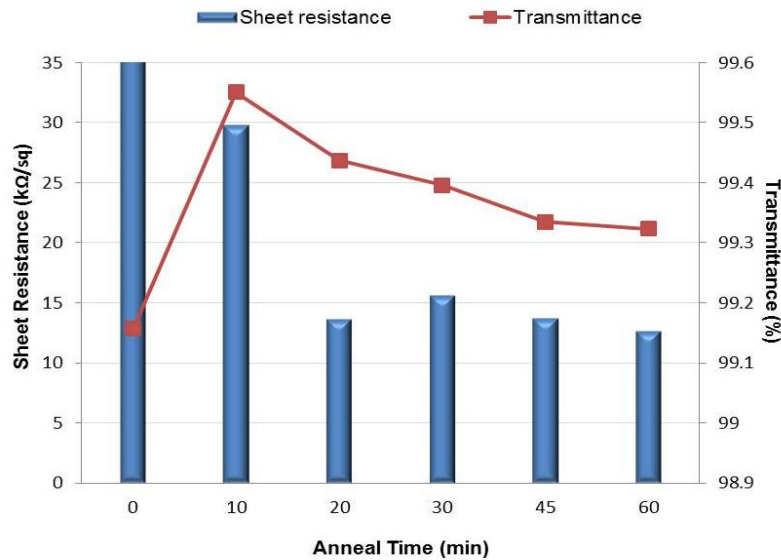


Figure 49 Sheet resistance and transmittance (at 550 nm) as a function of anneal time.

The films were characterized by SEM (Figure 50) to keep track of the morphology changes caused by the annealing process. Without annealing, no SWCNTs could be observed on the substrate. With 10 min annealing, a rather open network

composed of short tubes was obtained, with a density of ~ 5 tubes/ μm^2 . Starting from 20 min, a denser and more interconnected network was formed as the annealing time increased, and the tube density boosted by ten times to ~ 50 tubes/ μm^2 , which corresponds well with the increase in film conductivity observed after 20 min annealing. The changes in morphology also correspond with the changes in transmittance. That is, the open film obtained with only 10 min annealing time resulted in the lowest SWCNT coverage and highest optical transmittance. Without annealing, an amorphous shell associated with the organic fractions of the ferritin still remained on the substrate, causing deactivation of Fe [269]. In addition, these fragments increase the absorption of light but do not enhance conductivity. Therefore, this sample exhibited high resistance and low optical transmittance.

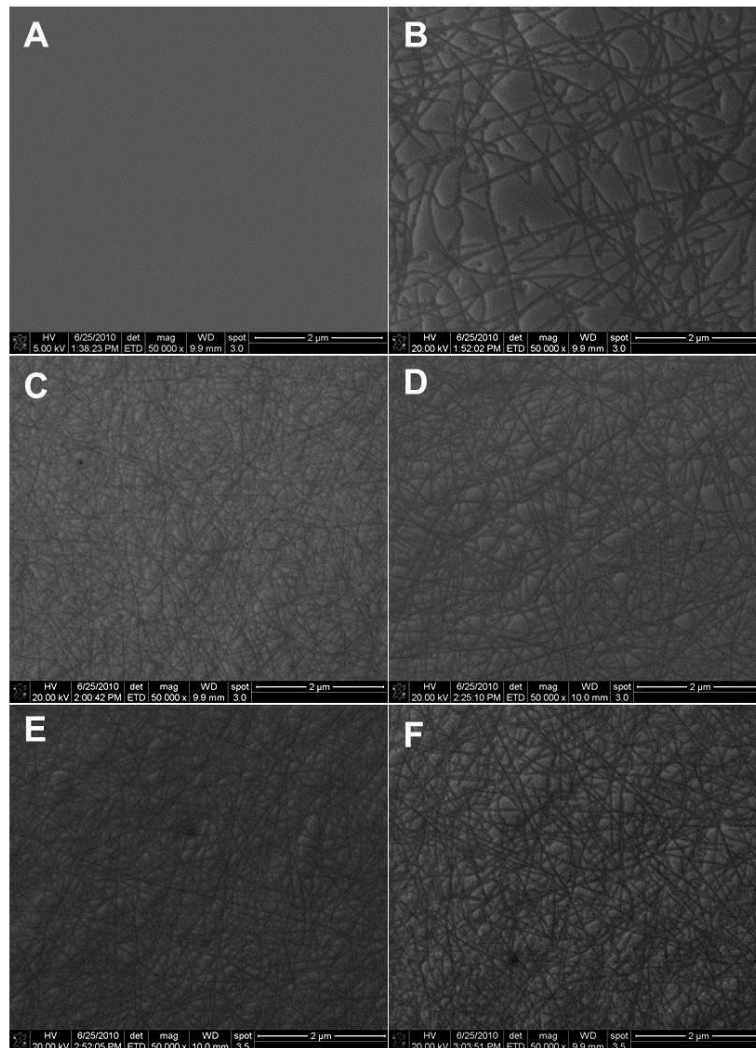


Figure 50 SEM images of SWCNT films obtained with annealing time of 0 min (A), 10 min (B), 20 min (C), 30 min (D), 45 min (E) and 60 min (F).

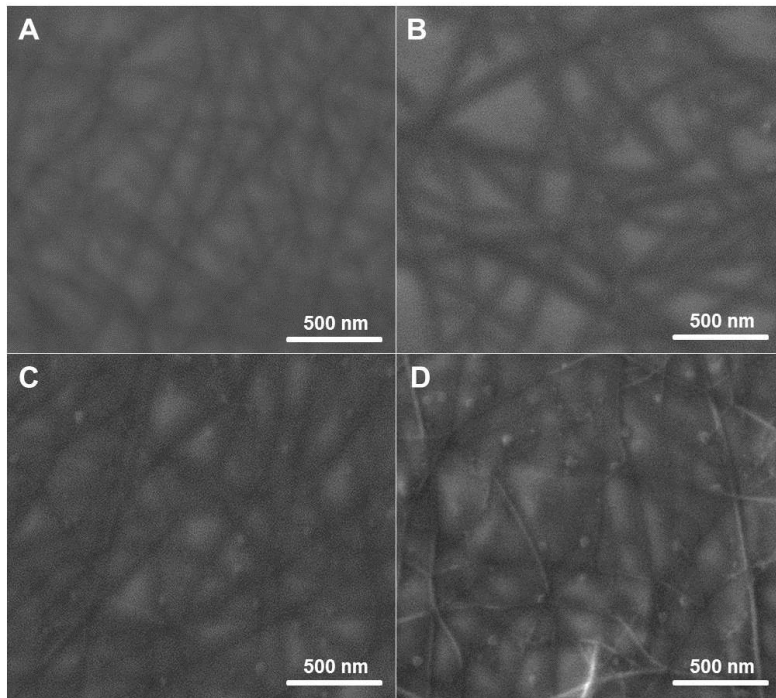


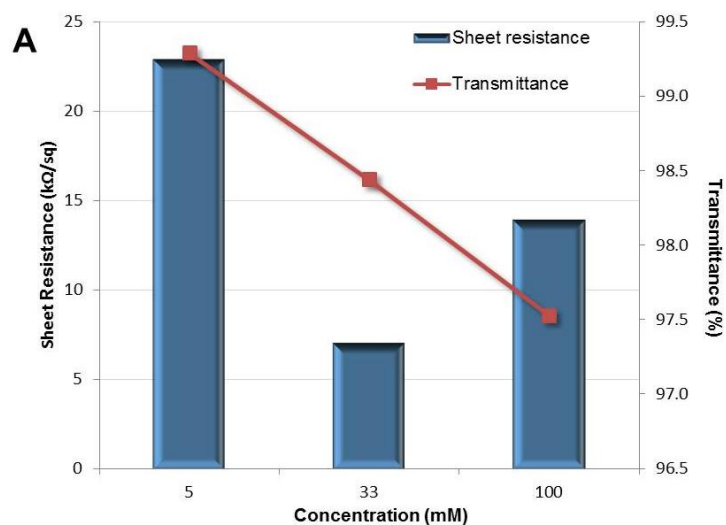
Figure 51 Higher-magnification SEM images of SWCNT films obtained with annealing time of 20 min (A), 30 min (B), 45 min (C) and 60 min (D).

The clear correlation observed between the catalyst annealing time and the film morphology (performance) can be explained when we look into the SWCNT growth and termination mechanisms. In a recent study on the growth of aligned SWCNTs on ST-cut quartz substrates [270], we have observed that the termination of the nanotube growth was accelerated by nanotube-nanotube interaction that lead to hindrance of the growth and subsequent catalyst deactivation [271]. On the other hand, it is well known that high temperature treatments (e.g. during annealing) lead to metal particle sintering [272]. As can be seen from the higher-magnification SEM images of the annealing series (Figure 51), when the samples were annealed for less than 30 min, the sintering of the catalyst particles did not result in particle growth large enough to be detectable. By contrast, annealing treatments for more extended periods (e.g. 45 and 60 min) led to

particles large enough to be clearly observed by SEM. It has been previously demonstrated [273-275] that there is a direct correlation between the size of the metal clusters that catalyze the growth of SWCNTs and the nanotube diameters, i.e. larger metal clusters generate nanotubes of larger diameters. Therefore, we proposed that the growth hindrance caused by nanotube-nanotube interaction is less pronounced when the diameter is larger, since larger diameter implies higher nanotube rigidity. Therefore, one can anticipate that these nanotubes should be longer and thus of higher conductivity. In addition, Dai et al. [276] have shown that contact resistance seems to increase significantly for the small diameter nanotubes.

3.3.2.3 Effects of catalyst concentration

For this comparison we fabricated films with varying ferritin concentration (C5, C33 and C100), while keeping the rest of the parameters constant. That is, all the samples in this series went through 60 min annealing and 30 min reaction. The results of the optoelectronic performance are summarized in Figure 52.



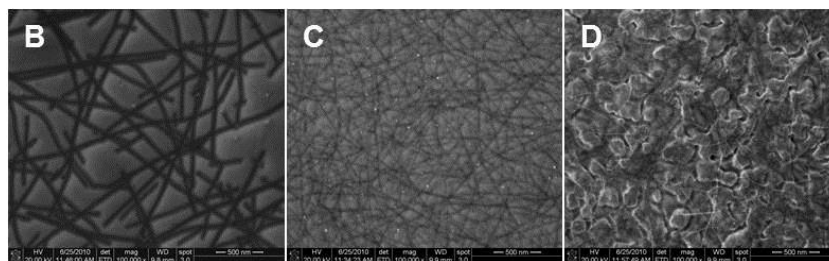


Figure 52 Sheet resistance and transmittance (at 550 nm) as a function of ferritin concentration and their corresponding SEM images. The samples were annealed for 60 min and reaction lasted for 30 min.

First, it is observed that the optical transmittance of the film decreased with increased ferritin concentration. The sheet resistance, on the other hand, went through a minimum at C33. This behavior can be rationalized in terms of the film morphology observed in the SEM images (Figures 52B, C and D). It can be seen that, at high Fe concentration, relatively large Fe clusters were formed on the substrate. It appears that the high concentration of ferritin precursor not only decreases the transparency but also reduced the concentration of nanotubes formed. Instead of the tight network observed at intermediate Fe concentrations, a relatively sparse structure with a density of ~ 40 tubes/ μm^2 is obtained at high concentrations. At the lowest concentration end, very small catalyst particles were formed after annealing. As can be compared in Figures 52B and C, no catalyst particles are visible on the sample made with C5 solution while they are clearly observed on the one made with C33 solution. As discussed earlier, smaller particles generate small diameter nanotubes, which are more easily hindered by interaction with other tubes and terminate growth more quickly. As a result, shorter tubes are produced, evidenced by a larger number of tube tips but lower tube density (~ 7 tubes/ μm^2) observed in the image. Therefore, on the film made with the C5 solution, a higher transparency but lower conductivity were obtained compared to that

made with C33 solution. The C33 film, on the other hand, has a tube density as high as ~ 70 tubes/ μm^2 .

It is also worth noting that the C33-A60-Rz sample of this series showed higher conductivity and lower transmittance than the C33-A60-Rz sample of the annealing series. This difference can be ascribed to the additional 10 min of reaction that the latter underwent. This result indicates that reaction time is another important parameter that one can use to optimize film performance.

3.3.2.4 SWCNT film evaluation

A popular method to quantify TCE performance is based on the following equation [277]:

$$T = \left(1 + \frac{1}{2R_S} \sqrt{\frac{\mu_0 \sigma_{op}}{\epsilon_0 \sigma_{dc}}}\right)^{-2}$$

Where T is the transparency measured at 550 nm, R_S the sheet resistance, σ_{dc} the electrical conductivity, σ_{op} the optical conductivity, $\mu_0 = 4\pi \times 10^{-7} \text{NA}^{-2}$ the free space permeability, and $\epsilon_0 = 8.8542 \times 10^{-12} \text{C}^2 \text{N}^{-1} \text{m}^{-2}$ the free space permittivity. For a given sheet resistance, the lower the σ_{op}/σ_{dc} ratio the higher is the transparency of the film. Therefore, films with low σ_{op}/σ_{dc} ratios are good candidates for TCEs. For example, to reach a sheet resistance of 15 k Ω /sq at a transparency of 98% the required ratio is 2.5. However, to increase the transparency to 99.5%, the ratio should decrease to 0.15.

Table 10 σ_{op}/σ_{dc} values of the samples from this study

Sample Name	σ_{op}/σ_{dc}
Annealing Series	
C33-A10-R20	0.36
C33-A20-R20	0.21
C33-A30-R20	0.25
C33-A45-R20	0.24
C33-A60-R20	0.23
Concentration Series	
C100-A60-R30	0.93
C33-A60-R30	0.30
C5-A60-R30	0.44

The σ_{op}/σ_{dc} ratios obtained for the two series in this study are listed in Table 10. We compared transparency-sheet resistance data reported in several recent publications (Table 11) with those in this study. While small ratios have been obtained in the intermediate transparency region, in the ultrahigh transparent region, open circuit are often observed (i.e. σ_{op}/σ_{dc} infinitely large). By contrast, for the annealing series, our films have transparencies above 99% and an average σ_{op}/σ_{dc} ratio of 0.26. Figure 53 shows the results of the annealing series along with some data extracted from recent literature. Using the σ_{op}/σ_{dc} ratio of 0.26 one can extrapolate the high transparency data to the lower range for comparison with the less transparent films.

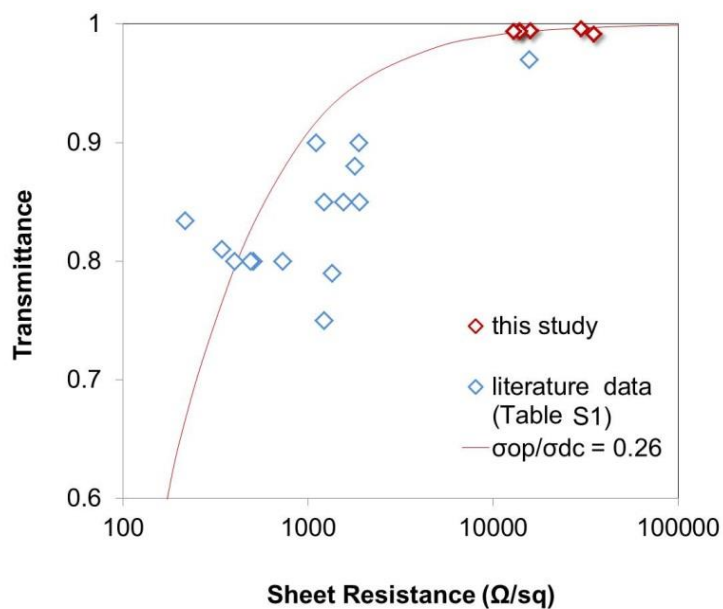


Figure 53 Transmittance vs. sheet resistance in this study and literature.

Table 11 Optoelectronic performance of films reported in the literature

Process	R_s (Ω/sq)	T%	Reference
Liquid-liquid interface	20000	97%	[38]
Air brush	1000	90%	[39]
Mayer rod or draw- down rod	700/300*	90%	[40]
Filter	1100	88%	[8]
Layer by layer	1620	85%	[41]
Layer by layer	1100	85%	[42]
Air brush	956/472*	85%	[43]
Roll-to-roll	24	83.4%	[44]
Ultrasonic spray	70	81%	[45]
Dip or spray coating	332	80%	[46]
Spray coating	150/80*	80%	[5]
Filter/stamp	150	80%	[47]
Spin-coating	100	80%	[48]
Vacuum filtration	1000/220*	79%	[49]
Vacuum filtration	1300/231**	75%	[4]

3.3.3 Graphene synthesized on copper foils

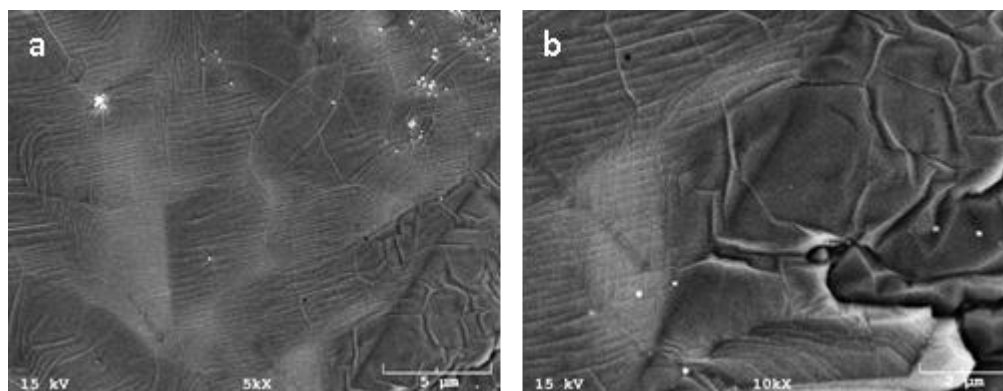


Figure 54 SEM images of graphen synthesized on copper foils.

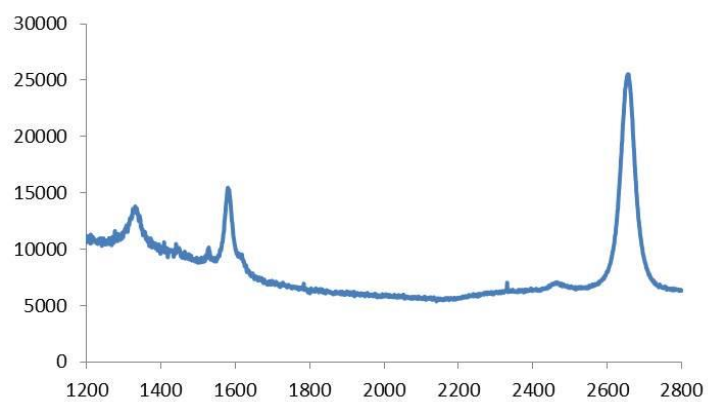


Figure 55 Raman spectrum of the synthesized graphene.

3.3.4 Application of the synthesized SWCNT films and graphene in FETs

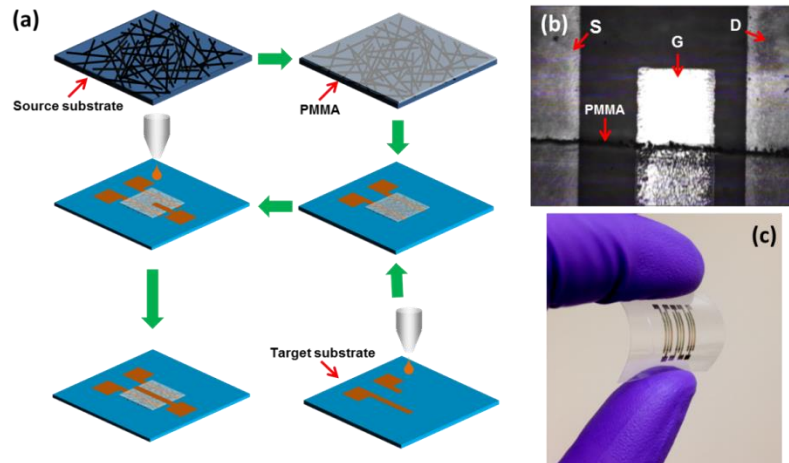


Figure 56 (a) Schematic of the fabrication procedure: spin coating PMMA onto source substrate, transferring PMMA/SWCNT layer onto target substrate with pre-printed source and drain, printing gate electrode on top of PMMA. (b) optical image taken by the camera of the printer showing source (S), drain (D), gate (G) and PMMA layer. The length of the image corresponds to ~1.6 mm. (c) a complete three-transistor array device on PET substrate.

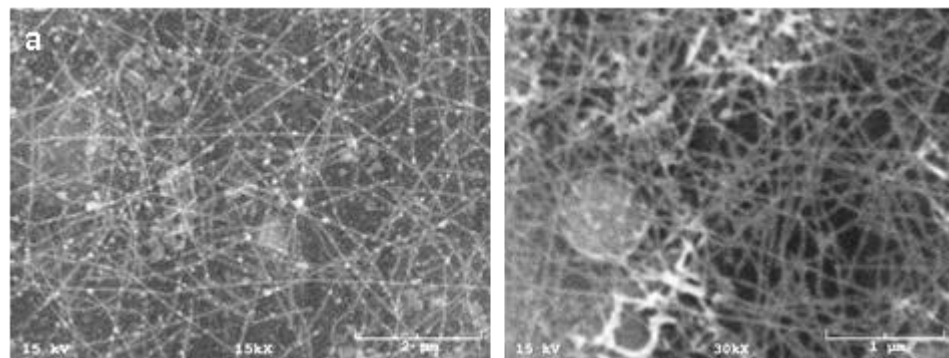


Figure 57 SEM images of SWCNT film transferred to polyimide (a) and glass (b) substrate.

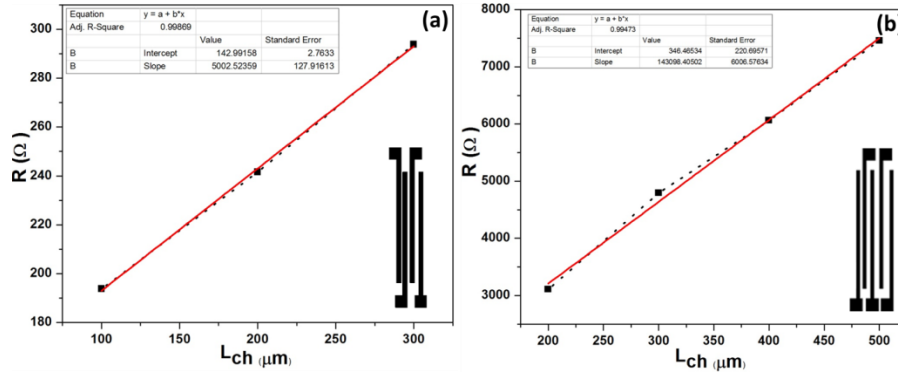


Figure 58 Plot of resistance versus channel length for calculating the specific contact resistance of (a) electrode-graphene and (b) electrode-SWCNT film. Insets show schematics of electrodes used for this measurements.

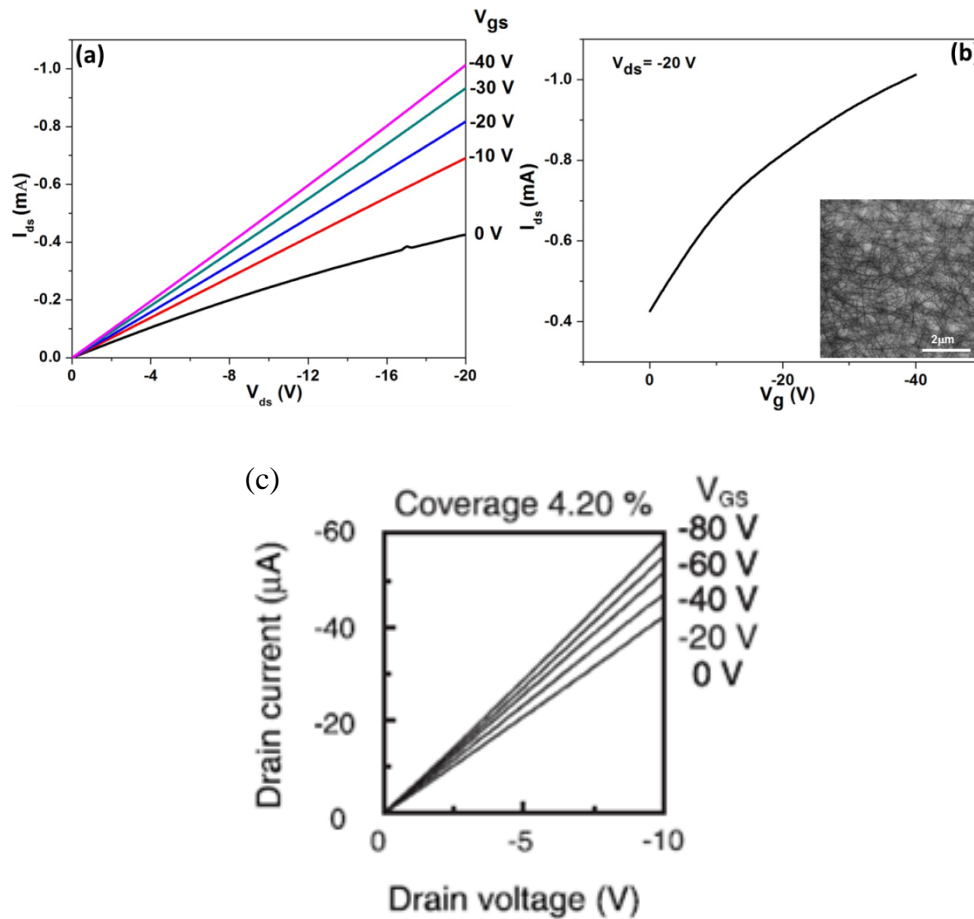


Figure 59 Electrical measurements of the SWCNT TFT device. (a) I_{ds}/V_{ds} characteristics at various V_g . (b) transfer characteristics of the device, inset: SEM image of the SWCNT film on source substrate. (c) I_{ds}/V_{ds} characteristics of a SWCNT TFT device reported in Reference 203.

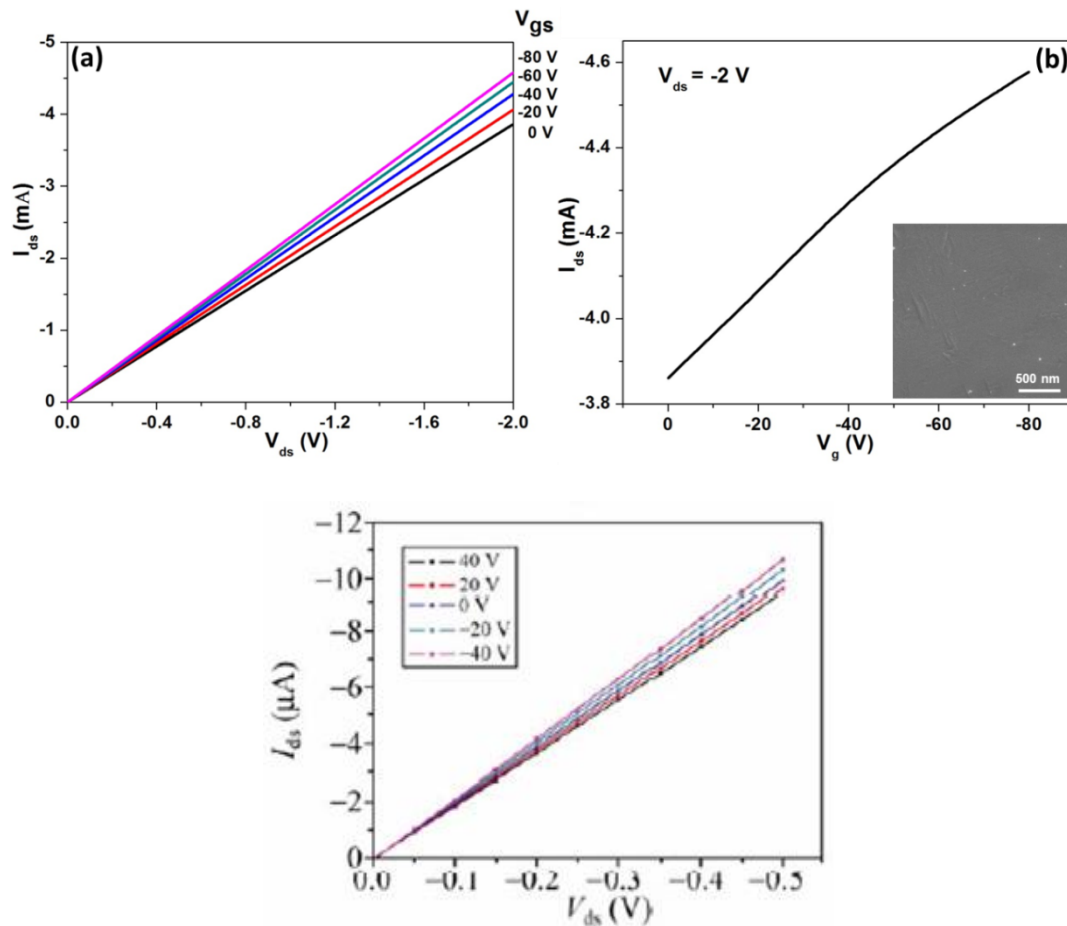


Figure 60 Electrical measurements of the graphene TFT device. (a) I_{ds}/V_{ds} characteristics at various V_g . (b) transfer characteristics of the device. Inset: SEM image of the graphene on source substrate. (c) I_{ds}/V_{ds} characteristics of a graphene TFT device reported in Reference 278.

Table 12 Characteristics of the SWCNT-TFT and graphene-TFT

Characteristic	Sheet resistant (k Ω /sq)	Mobility (cm ² V ⁻¹ s ⁻¹)	Contact resistance (m Ω cm ²)
Device			
SWCNT-TFT	~25	~1.5 - ~10.5	~260
graphene-TFT	~ 2.5	~20 - ~43	18

The typical spacing between the source and drain, i.e., the channel length, was 1 mm. The relatively large channel length was chosen mainly for the purpose of reducing the effect of contact resistance between the carbon nanomaterials and the electrodes, since both the SWCNT networks and graphene used in this study were highly conductive. In fact, it's been shown that in typical percolating networks such as those of SWCNTs, modulation of gate voltages is sensitive to the channel length, and a large channel length can effectively decrease the probability of purely metallic pathways from source to drain [279]. Thus, a large channel length is necessary to achieve reasonable gate modulation. SEM examination of the SWCNT network (Figure 59b inset) reveals that it consists of neat long tubes interlinked at a high density, which accounts for its finite sheet resistance of $\sim 25 \text{ k}\Omega/\text{sq}$ and thus the relatively large drain currents (on the order of mA, as shown below) of the devices. In the SEM of graphene, which has a sheet resistance of $\sim 2.5 \text{ k}\Omega/\text{sq}$ (Figure 60b inset), however, the weak contrast due to its two-dimensional nature makes it hard to visually justify its high conductivity. In addition, during device fabrication, the substrate needed to be processed before being placed back onto the printer platen and realigned with respect to the printer head for the second printing for the gate electrode. A larger device makes it easier to ensure that each part from different printing runs is in the designated position.

The specific contact resistance between the films and electrodes obtained from TLM calculations are $\sim 260 \text{ m}\Omega \text{ cm}^2$ and $18 \text{ m}\Omega \text{ cm}^2$ for the SWCNT network and graphene, respectively, which are in the expected range, considering the reported value of $20 \text{ m}\Omega \text{ cm}^2$ between silver electrodes and a SWCNT film with a sheet resistance of $\sim 350 \text{ }\Omega/\text{sq}$ [280].

The device characteristics are shown in Figure 59 and Figure 60 for an SWCNT-TFT (s-TFT) and graphene-TFT (g-TFT), respectively. The currents are on the magnitude of mA, suggesting that our devices are fairly robust and able to work at large currents without breakdown. The linear I_{ds} - V_{ds} curves indicate ohmic contacts between the film and electrode [281]. The curve series of the s-TFT highly resemble those of classic back-gate TFTs on silicon substrates with similarly high SWCNT coverage [203]. Its gate modulation is modest due to the finite sheet resistance of the SWCNT network [257]. Its mobility was calculated to be in the range of ~ 1.5 - ~ 10.5 $\text{cm}^2\text{V}^{-1}\text{s}^{-1}$, which is higher than most SWCNT-solution based TFTs [203,282,283,282-284]. In comparison with the s-TFT, as predicted [285], the g-TFT shows less gate modulation and significantly higher mobility of ~ 20 - ~ 43 $\text{cm}^2\text{V}^{-1}\text{s}^{-1}$. However, this value is still lower than that from CVD grown g-TFTs [286]. This is most likely due to the high contact resistance between the graphene and silver electrode [287], which can be replaced by other metal electrodes such as gold to dramatically reduce the contact resistance [288]. For mobility calculation, both s- and g-TFTs were treated as a 2-D film to calculate mobility from the slope of the transfer characteristics using the following equation:

$$\mu = \frac{dI_{ds}}{dV_g} \frac{L}{WC_iV_{ds}}$$

where L is the channel length (1 mm), W is the channel width (8.2 mm and 7.4 mm for the particular s- and g-TFTs studied, respectively), and C_i is the gate dielectric capacitance of PMMA using equation:

$$C_i = \frac{\epsilon_0 \epsilon_r A}{d}$$

where A is the gate area (channel width by gate electrode width of 0.5 mm), d is PMMA thickness (600 nm for s- and 540 nm for g-TFT, determined according to spin speed and manufacturer's data sheet [289]), ϵ_0 is electric constant ($\sim 8.854 \times 10^{-12} \text{ F m}^{-1}$), ϵ_r is the dielectric constant of PMMA, 2.9 for s- and 2.8 for g-TFT [290].

It is well known that under ambient environment, s- and g-TFTs show p-type behavior due to oxygen-doping induced charge-transfer [284] as observed in our case. PMMA has been shown to protect SWCNTs against oxygen doping as a cap [291]. The PMMA layers in this study are 540 nm–600 nm thick, and provide perfect encapsulation for SWCNTs and graphene. By carrying out the device fabrication in a glove box under vacuum or in inert gas, or simply annealing the finished device in vacuum, air-stable n-type TFTs can be achieved.

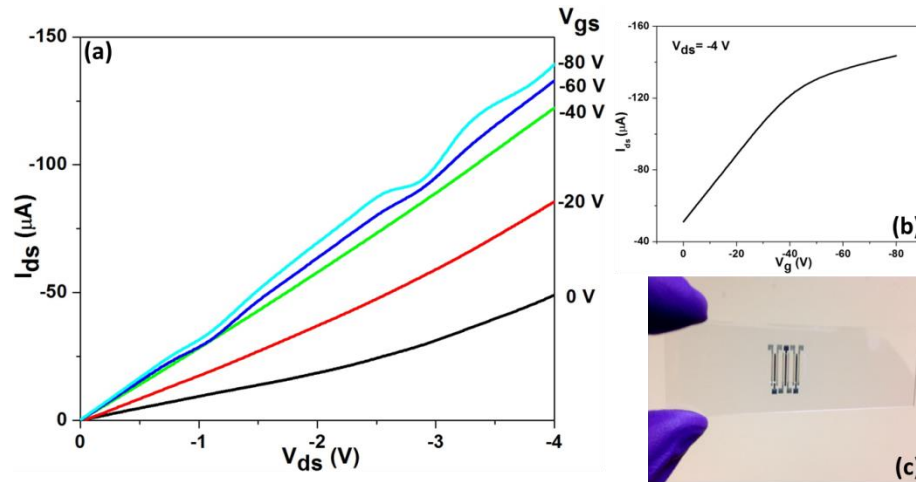


Figure 61 Electrical measurements of a SWCNT TFT on a glass slide. (a) I_{ds}/V_{ds} characteristics at various V_g . (b) transfer characteristics of the device. (c) a complete three-transistor array device.

3.4 Summary

With the same catalyst of Fe and different substrates, two different SWCNT film configurations were achieved due to the different interactions between SWCNTs and substrates. Furthermore, when the temperature was brought from a lower (as in FTS) to a higher zone (as in CVD), the hydrogasification activity of water became more pronounced. From the analysis of the morphology of HA-SWCNT arrays grown on ST-cut quartz substrates we propose an explanation for the beneficial effects of adding small amounts of water to the ethanol feed. We propose that the predominant role of water is the hydrogasification of excess carbon deposits on the catalyst particle, keeping the metal surface available for incorporation of carbon into the growing nanotube and preventing carbon encapsulation. This hydrogasification reaction is catalyzed by the metal and is optimized at intermediate carbon/water ratios, leading to enhanced SWCNT length, density, and uniformity.

In light of the effect of water in enhancing SWCNT growth demonstrated in HA-SWCNTs, we have synthesized conductive SWCNT films with ultra-high transparency on transparent support. The high conductivity and transparency are attributed to the intrinsic advantages of the in situ procedure (as compared with methods based on deposition from solution) that resulted in long and unbundled nanotubes. The SWCNT films not only show great promises in TCE application, with our novel method to fabricate TFTs, their potential applications in FETs were also demonstrated, which exhibited comparable device performances to those in literature. In addition, the fabrication method is highly extendable and universal, i.e., it can be applied to other

surface grown structures such as semiconducting nanowires, and the target substrate can be other materials, flexible or rigid. As an example, an s-TFT on a glass slide was fabricated (supplemental material). In addition, this method can easily accommodate source substrates of any sizes, since inkjet printing is a fast process and pattern design can be readily adjusted before actual printing. The proof-of-concept work was based on materials readily available and therefore was not optimized for TFTs, which leaves plenty of room for future improvements. For example, the synthesis conditions can be carefully tuned to achieve higher semiconductor content and appropriate coverage of SWCNT networks in favor of transistor behavior. Gold ink can replace the silver ink to reduce the contact resistance.

4. Conclusions and future directions

Catalyst supports are an important part of catalysts and play a critical role for the integrity and performance of catalysts. Supports essentially exert their effects through interactions, which can be divided into three categories as we see in this work:

1) Metal-support interaction

This is perhaps the most common and discussed type of interaction in literature. The strong metal-carbon nanotube interaction in our study prevented Ru catalysts from serious sintering and greatly enhanced catalyst dispersion. As a sharp contrast, Ru catalyst loaded onto silica showed larger particle sizes and lower dispersion, although the same preparation procedure was employed.

2) Solvent-support interaction

The amphiphilic nature of the nanohybrids enables their interaction with water and oil to form water-in-oil emulsion in a similar way surfactants do, which maximizes interfacial area between the two phases, enhances the catalyst particle dispersion and eases the mass transfer of products. A simple mixture of water and oil without the formation of emulsion doesn't have such advantages.

3) Product-support interaction

The product-support interaction was evident in FTS. In the case of activated carbon as catalyst support, the microporosity and hydrophobicity worked together to trap hydrocarbon products and poisoned the catalyst; in the case of silica support, its hydrophilicity inhibited the conversion of alcohols into alkanes under hydrogenation conditions. But the more typical examples were found in our study on surface grown SWCNT films, in which directional interaction of the SWCNTs with the planar support

resulted in aligned nanotube arrays, while isotropic interaction resulted in random networks.

Conventional processes of FTS or SWCNT growth don't involve the intentional addition of water, while the promotion effects have been subject to study in both cases. An important contribution of our study is that we've greatly extended the horizon of such discussions. That is, for FTS, we explored the addition of liquid water to organic solvent, and in particular, the formation of emulsion and its effects to FTS, while earlier studies used only water vapor. Adding water into the carbon feed for SWCNT film growth is an important addition to previous studies on the water effect on CNT forest formation. However, water promotes reactions in distinctive ways in the two cases, largely depending on the experimental condition, temperatures in particular. In FTS where the temperature is relatively low, water doesn't involve as a sacrificing agent, but rather as a transporting vehicle to shuttle hydrogen to assist CO dissociation; when the temperature gets high enough as in CVD growth of SWCNTs, hydrogasification on catalyst surfaces helps eliminate carbon deposits to revive the catalyst for continued nanotube growth. Interestingly, both FTS and SWCNT growth can be viewed as a two-step process, i.e., the dissociation of carbon from its source, and the addition of the carbon-based growing units to form chain structures. To our knowledge, water promotes the first step in FTS, and the second step in SWCNT growth. An important future research effort should be directed to whether water affects Step 2 for FTS, and Step 1 for SWCNT growth. A thorough understanding on the elemental reaction step level would be the key toward further exploring the advantages that water could provide.

The recently proposed dual-site model provides powerful support in explaining the observed differences between emulsion and water single-phase FTS. In addition, the lower initial CO conversion and slower deactivation observed with the larger Ru catalyst particle agrees with this model well. This hints a promising new direction in catalyst engineering, that is, the rational design of catalysts that possess multiple sites on single metal species. One way to do this is through the metal-support interaction to change the size of catalyst particles and thus the concentrations of different sites as indicated by the use of silica support in our study.

5. References

1. B.H. Davis, *Catal. Today* 71 (2002) 249.
2. R. Guettel, U. Kunz, T. Turek, *Chem. Eng. Technol.* 31 (2008) 746.
3. S.N. Khadzhiev, A.S. Lyadov, M.V. Krylova., A.Y. Krylova, *Pet. Chem.* 51 (2011) 24.
4. H. Kölbl, M. Ralek, *Cat. Rev. - Sci. Eng.* 21 (1980) 225.
5. R.L. Espinoza, A.P. Steynberg, B. Jager, A.C. Vosloo, *Appl. Catal. A: General* 186 (1999) 13.
6. S.T. Sie, *Rev. Chem. Eng.* 14 (1998) 109.
7. R.D. Srivastava, V.U.S. Rao, G. Cinquegrane, G.J. Stiegel, *Hydrocarbon Process.* 69 (1990) 59.
8. V.U.S. Rao, G.J. Stiegel, G.J. Cinquegrane, R.D. Srivastava, *Fuel Proc. Technol.* 30 (1992) 83.
9. M.J. van der Burgt, C.J. van Leeuwen, J.J. delAmico, S.T. Sie, *Methane Conversion* (D.M. Bibby, C.D. Chang, R.F. Howe, S. Yurchak, eds.), Elsevier Science, New York, **1988**, 473–482.
10. S.T. Sie, M.M.G. Senden, H. M. H. van Wechum, *Catal. Today* 8 (1991) 371.
11. R. J. Madon, E. Iglesia, S. C. Reyes, in *Selectivity in Catalysis* (S. L. Suib, M. E. Davis, eds.), American Chemical Society, Washington, DC, 1993, pp. 382– 396.
12. H. Schulz, M. Claeys, *Appl. Catal. A* 186 (1999) 91.
13. E. Iglesia, S.C. Reyes, R.J. Madon, S.L. Soled, *Adv. Catal.* 39 (1993) 221.
14. P. J. van Berge, R. C. Everson, *Stud. Surf. Sci. Catal.* 107 (1997) 207.
15. B. Jager, R. Espinoza, *Catal. Today* 23 (1995) 17.

-
16. M.E. Dry, T. Shingles, L.J. Boshoff, G.J. Oosthuizen, *J. Catal.* 15 (1969) 190.
 17. M.A. Vannice, *Catal. Rev.–Sci. Eng.* 14 (1976) 153.
 18. M.E. Dry, in *Catalysis—Science and Technology* (J.R. Anderson, M. Boudart, eds.), Springer-Verlag, New York, 1981, Vol. 1, pp. 160–255.
 19. E.S. Lox, G.B. Marin, E. de Graeve, P. Bussiere, *Appl. Catal. A* 40 (1988) 197.
 20. H.B. Zhang, G.L. Schrader, *J. Catal.* 95 (1985) 325.
 21. K. R. P. M. Rao, F. E. Huggins, V. Mahajan, G. P. Huffman, V. U. S. Rao, B. L. Bhatt, D. B. Bukur, B. H. Davis, R. J. O’Brien, *Top. Catal.* 2 (1995) 71.
 22. M.D. Shroff, D.S. Kalakkad, K.E. Coulter, S.D. Kohler, M.S. Harrington, N.B. Jackson, A.G. Sault, A.K. Datye, *J. Catal.* 156 (1995) 185.
 23. M.A. Vannice, *J. Catal.* 37 (1975) 462.
 24. H. Pichler, H. Buffleb, Brennstoff, *Chem.* 21 (1940) 273.
 25. S. Shetty, A.P.J. Jansen, R.A. van Santen, *J. Am. Chem. Soc.* 131 (2009) 12874.
 26. S. Shetty, R.A. van Santen, *Catalysis Today* 171 (2011) 168.
 27. R.A. van Santen, M.M. Ghouri, S. Shetty, E.M.H. Hensen, *Catal. Sci. & Tech.* 1 (2011) 891.
 28. M. Nurunnabi, K. Murata, K. Okabe, M. Inaba, I. Takahara, *Appl. Catal. A: Gen.* 340 (2008) 203.
 29. K. Okabe, K. Murata, M. Nakanishi, T. Ogi, M. Nurunnabi, Y. Liu, *Catal. Lett.* 128 (2009) 171.
 30. J.M. González Carballo, J. Yang, A. Holmen, S. García-Rodríguez, S. Rojas, M. Ojeda, J.L.G. Fierro, *J. Catal.* 284 (2011) 102.
 31. J. Kang, S. Zhang, Q. Zhang, Y. Wang, *Angew. Chem. Int. Ed.* 48 (2009) 2565.

-
32. X.Y. Quek, Y. Guan, R.A. van Santen, E.J.M. Hensen, *ChemCatChem* 3 (2011) 1735.
 33. C.N. Hamelink, A.P.C. Faaij, H. den Uil, *Energy* 29 (2004) 1743.
 34. C.J. Kim, US Patent 5,227,407 (1993).
 35. F. Fischer, H. Tropsch, *Brennst. Chem.* 4 (1923) 276.
 36. B. W. Wojciechowski, *Catal. Rev.—Sci. Eng.* 30 (1988) 629.
 37. R.B. Anderson, *The Fischer-Tropsch Synthesis*, Academic Press, Orlando (1984).
 38. G.A. Huff, Jr. C.N. Satterfield, *Ind. Eng. Chem. Process Des.* 23 (1984) 696.
 39. D.D. Hibbitts, B.T. Loveless, M. Neurock, E. Iglesia, *Angew. Chem. Int. Ed.* 20 (2013) 12273.
 40. B. Loveless, D. Hibbitts, C. Buda, M. Neurock, E. Iglesia, *J. Am. Chem. Soc.* 135 (2013) 6107.
 41. T.J. Donnelly, C.N. Satterfield, *Appl. Catal. A: Gen.* 52 (1989) 93.
 42. R.A. Dictor, A.T. Bell, *J. Catal.* 97 (1986) 121.
 43. D. B. Bukur, S. A. Patel, X. Lang, *Appl. Catal. A* 61 (1990) 329.
 44. E. W. Kuipers, C. Scheper, J. H. Wilson, H. Oosterbeek, *J. Catal.* 158 (1996) 288.
 45. E. Iglesia, S.C. Reyes, R.J. Madon, *J. Catal.* 129 (1991) 238.
 46. P.J. Flory, *J. Am. Chem. Soc.* 58 (1936) 1877.
 47. B. Sarup, B. W. Wojciechowski, *Can. J. Chem. Eng.* 66 (1988) 831.
 48. H. Schulz, E. van Steen, M. Claeys, in *Selective Hydrogenation and Dehydrogenation*, DGMK, Kassel, Germany, 1993.

-
49. Dry, M. E. *J Mol. Catal.* 17 (1982) 133.
 50. T. Komaya, A.T. Bell, *J. Catal.* 146 (1994) 237.
 51. S. Novak, R. J. Madon, H. Suhl, *J. Catal.*, 77 (1982) 141.
 52. E.W. Kuipers, I. H. Vinkenburg, H. Oosterbeek, *J. Catal.* 152 (1995) 137.
 53. C. L. Bianchi, V. Ragaini, *J. Catal.* 168 (1997) 70.
 54. H. Schulz, H. Gokcebay, in *Catalysis of Organic Reactions* (J. R. Kosak, ed.), Marcel Dekker, New York, 1984.
 55. R.J. Madon, E. Iglesia, *J. Catal.* 139 (1993) 576.
 56. R.J. Madon, S.C. Reyes, E. Iglesia, *J. Phys. Chem.* 95 (1991) 7795.
 57. L.M. Tau, A. Dabbagh, B. H. Davis, *Energy Fuels* 4 (1990) 94.
 58. W. H. Zimmerman, D. B. Bukur, S. Ledakowicz, *Chem. Eng. Sci.*, 47 (1992) 2707.
 59. A.M. Saib, D.J. Moodley, I.M. Ciobica, M.M. Hauman, B.H. Sigwebela, C.J. Weststrate, J.W. Niemantsverdriet, J. van de Loosdrecht, *Catal. Today* 154 (2010) 271.
 60. N.E. Tsakoumis, M. Rønning, Ø. Borg, E. Rytter, A. Holmen, *Cataly. Today* 154 (2010) 162.
 61. J.G. Goodwin Jr., D.O. Goa, S. Erdal, F.H. Rogan, *Appl. Catal.* 24 (1986) 199.
 62. H. Abrevaya, M.J. Cohn, W.M. Targos, H.J. Robota, *Catal. Lett.* 7 (1990) 183.
 63. R.A.D. Betta, A.G. Piken, M. Shelef, *J. Catal.* 35 (1974) 54.
 64. R.A. Dalla Betta, A.G. Piken, M. Shelef, *J. Catal.* 40 (1975) 173.
 65. K.R. Krishna, A.T. Bell, *J. Catal.* 130 (1991) 597.
 66. R.M. Bowman, C.H. Bartholomew, *Appl. Catal.* 7 (1983) 179.

-
67. S. Mukkavilli, C.V. Wittmann, L.L. Taviarides, *Industrial & Engineering Chemistry Process Design and Development* 25 (1986) 487.
 68. T.E. Hoost, J.G. Goodwin Jr., *J. Catal.* 137 (1992) 22.
 69. H.M.T. Galvis, J.H. Bitter, C.B. Khare, M. Ruitenbeek, A. Dugulan, K.P. de Jong, *Science* 335 (2012) 835.
 70. J. Garcia, H.T.Gomes, P.Serp, P. Kalck, J.L. Figueiredo, J.L. Faria, *Catal. Today* 102 (2005) 101.
 71. H.T. Gomes, P.V. Samant, P. Serp, P. Kalck, J.L. Figueiredo, J.L. Faria, *Appl. Catal. B* 54 (2004)175.
 72. H. Chen, J. Lin, Y. Cai, X. Wang, J. Yi, J. Wang, G. Wei, Y. Lin, D. Liao, *Appl. Surf. Sci.* 180 (2001) 328.
 73. K. Niesz, A. Siska, I. Vesselenyi, K. Hernadi, D. Mehn, G. Galbacs, Z. Kónya, I. Kiricsi, *Catal. Today* 76 (2002) 3.
 74. T. Prasomsri, D. Shi, D.E. Resasco, *Chem. Phys. Lett.* 497 (2010) 103.
 75. J. Kastner, T. Pichler, H. Kuzmany, *Chem. Phys. Lett.* 221 (1994) 53.
 76. S. Yin, Q. Zhang, B. Xu, W. Zhu, C. Ng, C. Au, *J. Catal.* 224 (2004) 384.
 77. J. Kang, S. Zhang, Q. Zhang, Y. Wang, *Angew. Chem. Int. Ed.* 121 (2009) 2603.
 78. S. Crossley, J. Faria, M. Shen, D.E. Resasco, *Science* 327 (2010), 68.
 79. R.P. Silvy, Y. Tan, (2010), Patent WO2011009071A1.
 80. M. Worley, J. Yale, A. Dutta, National Renewable Energy Laboratory report NREL/SR-5100-57085, (2012).
 81. M. Shen, D.E. Resasco, *Langmuir*, 25 (2009) 10843.

-
82. K. Tomishige, M. Asadullah, K. Kunimori, *Catal. Today* 89 (2004), 389.
 83. H. Boerrigter, H. Uil, H.P. Calis, *Pyrolysis and Gasification of Biomass and Waste Expert Meeting*; Strasbourg, France, September 30-October 1, 2002.
 84. R.B. Anderson, *Catalysts for the Fischer–Tropsch Synthesis*; Van Nostrand Reinhold: New York, 1956.
 85. H. Schulz, *Appl. Cata.*, A 186 (1999) 3.
 86. Z. Kowalczyk, K. Stołeczki, W. Rarog-Pilecka, E. Miskiewicz, E. Wilczkowska, Z. Karpinski, *Appl. Cata. A* 342 (2008) 35.
 87. J.A. Mieth, J.A. Schwarz, *J. Catal.* 118 (1989) 203.
 88. Y. Chen, H. Wang, J.G. Goodwin, W.K. Shiflett, *Appl. Catal.* 8 (1983) 303.
 89. C.S. Kellner, A.T. Bell, *J. Catal.* 75 (1982) 251.
 90. G.L. Bezemer, J.H. Bitter, H.P.C.E. Kuipers, H. Oosterbeek, J.E. Holewijn, X. Xu, F. Kapteijn, A.J. Van Dillen, K.P. de Jong, *J. Am. Chem. Soc.* 128 (2006) 3956.
 91. M. Claeys, Van Steen, *Catal. Today* 71 (2002) 419.
 92. S. Storsæter, Ø. Borg, E.A. Blekkan, A. Holmen, *J. Catal.* 231 (2005) 405.
 93. S. Krishnamoorthy, M. Tu, M.P. Ojeda, D. Pinna, E. Iglesia, *J. Catal.* 211 (2002) 422.
 94. E. Iglesia, *Appl. Catal. A: Gen.* 161 (1997) 59.
 95. P. Forzatti, E. Tronconi, I. Pasquon, *Cat. Rev. - Sci. Eng.* 33 (1991) 109.
 96. E.G. Hancock, *Propylene and its industrial derivatives*; Benn: London, 1973.

-
97. A. De Klerk, *Fischer-Tropsch refining*; Wiley-VCH: Weinheim, 2011.
 98. S.A. Eliason, C.H. Bartholomew, *Appl. Catal. A: Gen.* 186 (1999), 229.
 99. T.K. Das, W.A. Conner, J. Li, G. Jacobs, M.E. Dry, B.H. Davis, *Energy Fuels* 19 (2005) 1430.
 100. I.C. Yates, C.N. Satterfield, *Energy Fuels* 5 (1991) 168.
 101. M. Ojeda, R. Nabar, A.U. Nilekar, A. Ishikawa, M. Mavrikakis, E. Iglesia, *J. Catal.* 272 (2010) 287.
 102. R.J. Madon, E. Iglesia, *J. Mol. Catal.* 163 (2000) 189.
 103. R.J. Madon, J.P. O'Connell, M. Boudart, *AIChE J.* 24 (1978) 904.
 104. R.L. Bain, D.C. Dayton, D.L. Carpenter, S.R. Czernik, C.J. Feik, R.J. French, K.A. Magrini-Bair, S.D. Phillips, *Ind. Eng. Chem. Res.* 44 (2005) 7945.
 105. F. Fischer, H. Tropsch, *Brennst. Chem.* 18 (1923) 274.
 106. S.D. Summerford (1950) US Patent 2,497,964, February 21.
 107. W.H. Zimmerman, D.B. Bukur, *Can. J. Chem. Eng.* 68 (1990) 292.
 108. G.P. Van der Laan, A.A.C.M. Beenackers, *Appl. Catal. A: Gen.* 193 (2000) 39.
 109. H. Schulz, M. Claeys, S. Harms, *Stud. Surf. Sci. Catal.* 107 (1997) 193.
 110. C.J. Kim, US Patent 0,355,216 (1993).
 111. T.K. Das, W. Conner, G. Jacobs, J. Li, K. Chaudhari, B.H. Davis, in *Proceedings of the 7th Natural Gas Conference*, Dalian, China, June 6–10, (2004), pp. 331–336.
 112. N. Kizhakevariam, X. Jiang, M. Weaver, *J. Chem. Phys.* 100 (1994) 6750.
 113. T. Yuzawa, T. Higashi, J. Kubota, J.N. Kondo, K. Domen, C. Hirose, *Surf. Sci.* 325 (1995) 223.

-
114. M. Nakamura, M. Ito, *Chem. Phys. Lett.* 335 (2001) 170.
 115. C. Bertole, C.A. Mims, G. Kiss, *J. Catal.* 210 (2002) 84.
 116. E. van Steen, M. Claeys, M.E. Dry, J. van de Loosdrecht, E.L. Viljoen, J.L. Visagie, *J. Phys. Chem. B* 109 (2005) 3575.
 117. G.W. Huber, C.G. Guymon, T.L. Conrad, B.C. Stephenson, C.H. Bartholomew, *Stud. Surf. Sci. Catal.* 139 (2001) 423.
 118. Y. Zhang, D. Wei, S. Hammache, J.G. Goodwin, *J. Catal.* 188 (1999) 281.
 119. D.L. King, *J. Catal.* 61 (1980) 77.
 120. D.S. Jordan, A.T. Bell, *J. Phys. Chem.* 90 (1986) 4797.
 121. D.S. Jordan, A.T. Bell, *J. Catal.* 107 (1987) 338.
 122. D.S. Jordan, A.T. Bell, *J. Catal.* 108 (1987) 63.
 123. P. Biloen, J.N. Helle, W.M.H. Sachtler, *J. Catal.* 58 (1979) 95.
 124. C.S. Kellner, A.T. Bell, *J. Catal.* 70 (1981) 418.
 125. H. Schulz, E. van Steen, M. Claeys, *Stud. Surf. Sci. Catal.* 81 (1994) 455.
 126. A. Eckstrom, J. Lapszewicz, *J. Phys. Chem.* 88 (1984) 4577.
 127. H.H. Nijs, P.A. Jacobs, *J. Catal.* 66 (1980) 401.
 128. E.W. Kuipers, C. Scheper, J.H. Wilson, I.H. Vinkenburg, H. Oosterbeck, *J. Catal.* 158 (1996) 228.
 129. H. Schulz, M. Claeys, *Appl. Catal. A* 186 (1999) 71.
 130. G.P. van der Laan, A.A.C.M. Beenackers, *Stud. Surf. Sci. Catal.* 119 (1998) 179.
 131. G.P. van der Laan, A.A.C.M. Beenackers, *Catal. Rev.* 41 (1999) 255.

-
132. R.C. Reid, J.M. Prausnitz, T.K. Sherwood, *The Properties of Gases and Liquids*, McGraw-Hill, New York, 1977.
133. R.S. Albal, Y.T. Shah, N.L. Carr, A.T. Bell, *Chem. Eng. Sci.* 39 (1984) 905.
134. U.J. Jauregui-haza, E.J. Pardillo-fontdevila, A.M. Wilhelm, H. Delmas, *Latin American Applied Research* 34 (2004) 71.
135. C. Xiao, Z. Cai, T. Wang, Y. Kou, N. Yan. *Angew. Chem. Int. Ed.* 47 (2008) 746.
136. D. Shi, J.A. Faria, A.A. Rownaghi, R.L. Huhnke, D.E. Resasco. *Energy & Fuels* 27 (2013) 6118.
137. S. Storsæter, Ø. Borg, E.A. Blekkan, A. Holmen, *J. Catal.* 231 (2005) 405.
138. S. Krishnamoorthy, M. Tu, M.P. Ojeda, D. Pinna, E. Iglesia, *J. Catal.* 211 (2002) 422.
139. J.M.G. Carballo, E. Finocchio, S. García-Rodríguez, M. Ojeda, J.L.G. Fierro, G. Busca, S. Rojas, *Catal. Today* 214 (2013) 2.
140. S. Mukkavilli, C.V. Wittmann, L.L. Taviarides, *Industrial & Engineering Chemistry Process Design and Development* 25 (1986) 487.
141. D.W. Mckee, *Carbon* 12 (1974) 453.
142. Y.T.H. Watanabe, A. Tomit, *Carbon* 15 (1977) 103.
143. A. Kruse, *J. of Supercritical Fluids* 47 (2009) 391.
144. A. Kruse, P. Bernolle, N. Dahmen, E. Dinjus, P. Maniam, *Energy Environ. Sci.* 3 (2010) 136.
145. Y. Guo, S.Z. Wang, D.H. Xu, Y.M. Gong, H.H. Ma, X.Y. Tang, *Renewable and Sustainable Energy Reviews* 14 (2010) 334.

-
146. Y. Matsumuraa, T. Minowab, B. Poticc, S.R.A. Kerstenc, W. Prinsc, W.P.M. van Swaaijc, B. van de Beldd, D.C. Elliotte, G.G. Neuenschwandere, A. Krusef, M.J. Antal Jr. *Biomass and Bioenergy* 29 (2005) 269.
147. D.C. Elliott, *Biofuels, Bioprod. Bioref.* 2 (2008) 254.
148. D.C. Elliott, T.R. Hart, G.G. Neuenschwander, *Industrial & Engineering Chemistry Research* 45 (2006) 3776.
149. A.J. Byrd, K.K. Pant, R.B. Gupta, *Industrial & Engineering Chemistry Research* 46 (2007) 3574.
150. C.J. Kim, US Patent 0,355,218 (1993); US Patent 5,269,821 (1993).
151. A.M. Hilmen, D. Schanke, K.F. Hanssen, A. Holmen, *Appl. Catal. A: Gen.* 186 (1999) 169.
152. S. Storsæter, Ø. Borg, E.A. Blekkan, B. Tøtdal, A. Holmen, *Catal. Today* 100 (2005) 343.
153. D. Schanke, A.M. Hilmen, E. Bergene, K. Kinnari, E. Rytter, E. Adnanes, A. Holmen, *Energy Fuels* 10 (1996) 867.
154. A.K. Dalai, B.H. Davis, *Applied Catalysis A: Gen* 348 (2008) 1.
155. T.J. Donnelly, C.N. Satterfield, *Appl. Catal. A: Gen.* 52 (1989) 93.
156. D. B. Bukur, S. A. Patel, X. Lang, *Appl. Catal. A* 61 (1990) 329.
157. A.J. Markvoort, R.A. van Santen, P.A.J. Hilbers, E.J.M. Hensen, *Angew. Chem. Int. Ed.* 51 (2012) 9015.
158. S.G. Shetty, I.M. Ciobica, E.J.M. Hensen, R.A. van Santen, *Chem. Comm.* 47 (2011) 9822.
159. C.C. Chen, C.E. Lin, *Anal. Chim. Acta* 321 (1996) 215.

-
160. G.L. Bezemer, J.H. Bitter, H.P.C.E. Kuipers, H. Oosterbeek, J.E. Holewijn, X. Xu, F. Kapteijn, A.J. Van Dillen, K.P. de Jong, *J. Am. Chem. Soc.* 128 (2006) 3956.
161. J. Kang, S. Zhang, Q. Zhang, Y. Wang, *Angew. Chem. Int. Ed.* 121 (2009) 2603.
162. H. Bielawa, O. Hinrichsen, A. Birkner, M. Muhler *Angew. Chem. Int. Ed.* 40 (2001) 1061.
163. K. Honkala, A. Hellman, I. N. Remediakis, A. Logadottir, A. Carlsson, S. Dahl, C. H. Christensen, J. K. Nørskov, *Science* 307 (2005) 555.
164. Q. Cao, J.A. Rogers, *Adv. Mater.* 21 (2009) 29.
165. S. Kim, S. Ju, J.H. Back, Y.Xuan, P.D. Ye, M. Shim, D.B. Janes, S. Mohammadi, *Adv. Mater.* 21 (2009) 564.
166. J.N. Tey, I.P.M. Wijaya, Z. Wang, W.H. Goh, A. Palaniappan, S.G. Mhaisalkar, I. Rodriguez, S. Dunham, J.A. Rogers, *Appl. Phys. Lett.* 94 (2009) 013107.
167. M.M.J. Treacy, T.W. Ebbesen, J.M. Gibson, *Nature* 381 (1996) 678.
168. M. Yu, B.S. Files, S. Arepalli, R.S. Ruoff, *Phys. Rev. Lett.* 84 (2000) 5552.
169. R.S. Ruoff, D.C. Lorents, *Carbon* 33 (1995) 925.
170. J. Hone, M. Whitney, C. Piskoti, A. Zettl, *Physical Review B* 59 (1999) R2514.
171. S. Berber, Y.K. Kwon, D. Tomanek, *Physical Review Letters* 84 (2000) 4613.
172. A.C. Dillon, K.M. Jones, T.A. Bekkedahl, C.H. Kiang, D.S. Bethune, M.J. Heben, *Nature* 386 (1997) 377.
173. C. Liu, Y.Y. Fan, M. Liu, H.T. Cong, H.M. Cheng, M.S. Dresselhaus, *Science* 286 (1999) 1127.
174. S. Iijima, *Nature* 354 (1991) 56.

-
175. B. Kitiyanan, W.E. Alvarez, J.H. Harwell, D.E. Resasco. *Chem. Phys. Lett.* 317 (2000) 497.
176. J.E. Herrera, L. Balzano, A. Borgna, W.E. Alvarez, D.E. Resasco. *J.Catal.* 204 (2001) 129.
177. S.M. Bachilo, L. Balzano, J.E. Herrera, F. Pompeo, D.E. Resasco and R.B. Weisman. *J. Am. Chem. Soc.* 125 (2003) 11186.
178. E. Joselevich, C.M. Lieber, *Nano Lett.* 2 (2002) 1137.
179. H. Ago, K. Nakamura, K. Ikeda, N. Uehara, N. Ishigami, M. Tsuji, *Chem. Phys. Lett.* 408 (2005) 433.
180. K. Hata, D. N. Futaba, K. Mizuno, T. Namai, M. Yumura, S. Iijima, *Science* 306 (2004) 1362.
181. J. Xiao, S. Dunham, P. Liu, Y. Zhang, C. Kocabas; L. Moh; Y. Huang, K. Hwang, C. Lu, W. Huang, J.A. Rogers, *Nano Lett.* 9 (2009) 4311.
182. S.M. Huang, M. Woodson, R. Smalley, J. Liu, *Nano Lett.* 4 (2004) 1025.
183. M.H. Hu, Y. Murakami, M. Ogura, S. Maruyama, T. Okubo, *J. Catal.* 225 (2004) 230.
184. M Chhowalla, K.B.K Teo, C. Ducati, N.L. Rupersinghe, G.A.J. Amaratunga, A.C. Ferrari, D. Roy, J. Robertson, W. Milne, *J. Appl. Phys.* 90 (2001) 5308.
185. M.R. Maschmann, P.B. Amama, A. Goyal, Z. Iqbal, T.S. Fisher, *Carbon* 44 (2006) 2758.
186. M. Terrones, N. Grobert, J. Olivares, J.P. Zhang, H. Terrones, K. Kordatos, *Nature* 388 (1997) 52.

-
187. J.F. Colomer, J.F. Bister, I. Willems, Z. Konya, A. Fonseca A, G. Van Tendeloo, *Chem Commun* 14 (1999) 1343.
188. G.S. Duesberg, A.P. Graham, M. Liebau, R. Seidel, E. Unger, F. Kreupl, *Nano Lett.* 3 (2003) 257.
189. S. Fan, M.G. Chapline, N.R. Franklin, T.W. Tomblor, A.M. Cassell, H. Dai, *Science* 283 (1999) 512.
190. K. Hernadi, A. Fonseca, J.B. Nagy, A. Siska, I. Kiricsi. *Appl. Catal. A* 199 (2000) 245.
191. T. Hayashi, Y.A. Kim, T. Matoba, M. Esaka, K. Nishimura, T. Tsukada, *Nano Lett.* 3 (2003) 887.
192. W. Kim, H.C. Choi, M. Shim, Y. Li, D. Wang, H. Dai, *Nano Lett.* 2 (2002) 703.
193. Z.F. Ren, Z.P. Huang, J.W. Xu, J.H. Wang, P. Bush, M.P. Siegal, *Science* 282 (1998) 1105.
194. R. Seidel, G.S. Duesberg, E. Unger, A.P. Graham, M. Liebau, F. Kreupl, *J. Phys. Chem. B* 108 (2004)1888.
195. R. S. Wagner, W. C. Ellis, *Appl. Phys. Lett.*, 4 (1964) 89.
196. Y.Y. Wang, B. Li, P.S. Ho, Z. Yao, L. Shi, *Appl. Phys. Lett.* 89 (2006) 183113.
197. F.H. Gojny, M.H.G. Wichmann, U. Kopke, B. Fiedler, K. Schulte, *Compos. Sci. Technol.* 64 (2004) 2363.
198. H.P. Boehm, A. Clauss, G.O. Fischer, U. Hofmann, *Z. Anorg. Allg. Chem.* 316 (1962), 119.
199. K.S. Novoselov, A.K. Geim, S.V. Morozov, D. Jiang, Y. Zhang, S.V. Dubonos, I.V. Grigorieva, A.A. Firsov, *Science* 306 (2004), 666.

-
200. M.S. Dresselhaus, G. Dresselhaus, R. Saito, *Phys. Rev. B* 45 (1992) 6234.
201. J.W. Mintmire, B. I. Dunlap, C. T. White, *Phys. Rev. Lett.* 68 (1992) 631.
202. M. Ouyang, J. Huang, C.L. Cheung, C.M. Lieber, *Science* 292 (2001) 702.
203. H. Okimoto, T. Takenobu, K. Yanagi, Y. Miyata, H. Shimotani, H. Kataura, Y. Iwasa, *Adv. Mater.* 22 (2010) 3981.
204. L. Jia, Y. Zhang, J. Li, C. You, E. Xie, *Jour. Appl. Phys.* 104 (2008) 074318.
205. C. Su, A. Lu, Y. Chen, C. Wei, C. Weng, P. Wang, F. Chen, K. Leou, C. Tsai, *J. Phys. Chem. C* 114 (2010) 11588.
206. N. Yoshihara, H. Ago, K. Imamoto, M. Tsuji, T. Ikuta, K. Takahashi, *J. Phys. Chem. C* 113 (2009) 8030.
207. A. Ismach, L. Segev, E. Wachtel, E. Joselevich, *Angew. Chem. Int. Ed.* 43 (2004) 6140.
208. S.J. Kang, C. Kocabas, T. Ozel, M. Shim, N. Pimparkar, M.A. Alam, S.V. Rotkin, J.A. Rogers, *Nat. Nanotechnol.* 2 (2007) 230.
209. Y. Li, R. Cui, L. Ding, Y. Liu, W. Zhou, Y. Zhang, Z. Jin, F. Peng, J. Liu, *Adv. Mater.* 22 (2010) 1508.
210. D. Yuan, L. Ding, H. Chu, Y. Feng, T.P. McNicholas, J. Liu, *Nano Lett.* 8 (2008) 2576.
211. D. Phokharatkul, Y. Ohno, H. Nakano, S. Kishimoto, T. Mizutani, *Appl. Phys. Lett.* 93 (2008) 053112.
212. N. Patil, A. Lin, E.R. Myers, K. Ryu, A. Badmaev, C. Zhou, H.S.P. Wong, S. Mitra, *IEEE Trans. on Nanotechnol.* 8 (2009) 498.
213. S.W. Hong, T. Banks, J.A. Rogers, *Adv. Mater.* 22 (2010) 1.

-
214. Y. Qian, S. Huang, F. Gao, Q. Cai, L. Zhang, W. Hu, *J. Phys. Chem. C* 113 (2009) 6983.
215. N. Yoshihara, H. Ago, M. Tsuji, *J. Phys. Chem. C* 111 (2007) 11577.
216. P.B. Amama, C.L. Pint, L. McJilton, S.M. Kim, E.A. Stach, P.T. Murray, R.H. Hauge, B. Maruyama, *Nano Lett.* 9 (2009) 44.
217. T. Yamada, A. Maign, M. Yudasaka, K. Mizuno, D.N. Futaba, M. Yumura, S. Iijima, K. Hata, *Nano Lett.* 8 (2008) 4288.
218. J. Cui, A. Wang, N.L. Edleman, J. Ni, P. Lee, N.R. Armstrong, T.J. Marks, *Adv. Mater.* 13 (2001) 1476.
219. L. Hu, D.S. Hecht, G. Gruner, *Nano Lett.* 4 (2004) 2513.
220. Y. Zhou, L. Hu, G. Grüner, *Appl. Phys. Lett.* 88 (2006) 123109.
221. Z. Wu, Z. Chen, X. Du, J.M. Logan, J. Sippel, M. Nikolou, K. Kamaras, J.R. Reynolds, D.B. Tanner, A.F. Hebard, A.G. Rinzler, *Science* 305 (2004) 1273.
222. A.A. Green, M.C. Hersam, *Nano Lett.* 8 (2008) 1417.
223. H. Geng, K.K. Kim, K.P. So, Y.S. Lee, Y. Chang, Y.H. Lee, *J. Am. Chem. Soc.* 129 (2007) 7758.
224. M.E. Spotnitz, D. Ryan, H.A. Stone, *J. Mater. Chem.* 14 (2004) 1299.
225. T.V. Sreekumar, T. Liu, S. Kumar, L.M. Ericson, R.H. Hauge, R.E. Smalley, *Chem. Mater.* 15 (2003) 175.
226. Y. Wang, C. Di, Y. Liu, H. Kajiura, S. Ye, L. Cao, D. Wei, H. Zhang, Y. Li, K. Noda, *Adv. Mater.* 20 (2008) 4442.
227. S.J. Kang, C. Kocabas, T. Ozel, M. Shim, N. Pimparkar, M.A. Alam, S.V. Rotkin, J.A. Rogers, *Nat. Nanotechnol.* 2 (2007) 230.

-
228. N. Ishigami, H. Ago, K. Imamoto, M. Tsuji, K. Iakoubovskii, N. Minami, *J. Am. Chem. Soc.* 130 (2008) 9918.
229. S. Kim, S. Ju, J.H. Back, Y. Xuan, P.D. Ye, M. Shim, D.B. Janes, S. Mohammadi, *Adv. Mater.* 20 (2008) 1.
230. J. Hone, M.C. Llaguno, N.M. Nemes, A.T. Johnson, J.E. Fischer, D.A. Walters, M.J. Casavant, J. Schmidt, R.E. Smalley, *Appl. Phys. Lett.* 77(2000) 666.
231. J.E. Fischer, H. Dai, A. Thess, R. Lee, N.M. Hanjani, D.L. Dehaas, R.E. Smalley, *Phys. Rev. B* 55 (1997) 4921.
232. P.B. Amama, M.R. Maschmann, T.S. Fisher, T.D. Sands, *J. Phys. Chem. B* 110 (2006) 10636.
233. L. Durrer, T. Helbling, C. Zenger, A. Jungen, C. Stampfer, C. Hierold, *Sensors and Actuators B* 132 (2008) 485.
234. I. Wako, T. Chokan, D. Takagi, S. Chiashi, Y. Homma, *Chem. Phys. Lett.* 449 (2007) 309.
235. C. Kocabas, S. Hur, A. Gaur, M.A. Meitl, M. Shim, J.A. Rogers, *Small* 1 (2005) 1110.
236. S. Han, X. Liu, C. Zhou, *J. Am. Chem. Soc.* 127 (2005) 5294.
237. J.P. Edgeworth, N.R. Wilson, J.V. Macpherson, *Small* 3 (2007) 860.
238. P. Avouris, *Acc. Chem. Res.* 35 (2002) 1026.
239. J.H. Chen, C. Jang, S.D. Xiao, M. Ishigami, M.S. Fuhrer, *Nat. Nanotechnol.* 3 (2008) 206.
240. S.V. Morozov, K.S. Novoselov, M.I. Katsnelson, F. Schedin, D.C. Elias, J.A. Jaszczak, A.K. Geim, *Phys. Rev. Lett.* 100 (2008) 016602.

-
241. Y.B. Zhang, Y.W. Tan, H.L. Stormer, P.Kim, *Nature* 438 (2005) 201.
242. X. Li, W. Cai, J. An, S. Kim, J. Nah, D. Yang, R. Piner, A. Velamakanni, I. Jung, E. Tutuc, S.K. Banerjee, L. Colombo, R.S. Ruoff, *Science* 324 (2009) 1312.
243. D. Shi, D. E. Resasco, *Chem. Phys. Lett.* 511 (2011) 356.
244. S. Stankovich, D.A. Dikin, G.H.B. Dommett, K.M. Kohlhaas, E.J. Zimney, E.A. Stach, R.D. Piner, S.T. Nguyen, R.S. Ruoff, *Nature* 442 (2006) 282.
245. S. Stankovich, D.A. Dikin, R.D. Piner, K.A. Kohlhaas, A. Kleinhammes, Y. Jia, Y. Wu, S.T. Nguyen, R.S. Ruoff, *Carbon* 45 (2007) 1558.
246. Y.W. Zhu, M.D. Stoller, W.W. Cai, A. Velamakanni, R.D. Piner, D. Chen, R.S. Ruoff, *ACS Nano* 4 (2010) 1227.
247. K.S. Novoselov, A.K. Geim, S.V. Morozov, D. Jiang, Y. Zhang, S.V. Dubonos, I.V. Grigorieva, A.A. Firsov, *Science* 306 (2004) 666.
248. C. Wang, K. Ryu, A. Badmaev, J. Zhang, C. Zhou, *ACS Nano* 5 (2011) 1147.
249. L. Jiao, B. Fan, X. Xian, Z. Wu, J. Zhang, Z. Liu, *J. Am. Chem. Soc.* 130 (2008) 12612.
250. A. Reina, H. Son, L. Jiao, B. Fan, M.S. Dresselhaus, Z. Liu, J. Kong, *J. Phys. Chem. C* 112 (2008) 17741.
251. J. Veres, S. Ogier, G. Lloyd, D. Leeuw, *Chem. Mater.* 16 (2004) 4543.
252. J.H. Park, D.K. Hwang, J. Lee, S. Im, E. Kim, *Thin Solid Films* 515 (2007) 4041.
253. Z. Bao, *Adv. Mater.* 12 (2000) 227.

-
254. M. Halik, H. Klauk, U. Zschieschang, G. Schmid, W. Radlik, W. Weber, *Adv. Mater.* 14 (2002) 1717.
255. J. Veres, S.M. Ogier, S.W. Leeming, D.C. Cupertino, S.M. Khaffaf, *Adv. Funct. Mater.* 13 (2004) 199.
256. T.S. Huang, Y.K. Su, P.C. Wang, *Jap. Jour. Appl. Phys.* 47 (2008) 3185.
257. S.Y. Lee, S.W. Lee, S.M. Kim, W.J. Yu, Y.W. Jo, Y.H. Lee, *ACS Nano* 5 (2011) 2369.
258. J. Vaillancourt, H. Zhang, P. Vasinajindakaw, H. Xia, X. Lu, X. Han, D.C. Janzen, W.S. Shih, C.S. Jones, M. Stroder, M.Y. Chen, H. Subbaraman, R.T. Chen, U. Berger, M. Renn, *Appl. Phys. Lett.* 93 (2008) 243301.
259. H. Murrmann, D. Widmann, *IEEE Transactions on Electron Devices* 16 (1969) 1022.
260. D.N. Futaba, K. Hata, T. Yamada, K. Mizuno, M. Yumura, S. Iijima, *Phys. Rev. Lett.* 95 (2005) 056104.
261. L. Ding, D. Yuan, J. Liu, *J. Am. Chem. Soc.* 130 (2008) 5428.
262. B. Kong, D Jung, S. Oh, C. Han, H. Jung, *J. Phys. Chem. C* 111 (2007) 8377.
263. W. Zhou, X. Bai, E. Wang, S. Xie, *Adv. Mater.* 21 (2009) 4565.
264. G.T. Pham, Y.B. Park, S. Wang, Z. Liang, B. Wang, C. Zhang, P. Funchess, L. Kramer, *Nanotechnol.* 19 (2008) 325705.
265. D. Simien, J.A. Fagan, W. Luo, J.F. Douglas, K. Migler, J. Obrzut, *ACS Nano* 2 (2008) 1879.
266. D. Hecht, L. Hu, G. Grüner, *Appl. Phys. Lett.* 89 (2006) 133112.

-
267. P.E. Lyons, S. De, F. Blighe, V. Nicolosi, L.F.C. Pereira, M.S. Ferreira, J.N. Coleman, *J. Appl. Phys.* 104 (2008) 044302.
268. P.N. Nirmalraj, P.E. Lyons, S. De, J.N. Coleman, J.J. Boland, *Nano Lett.* 9 (2009) 3890.
269. A. Reina, M. Hofmann, D. Zhu, J. Kong, *J. Phys. Chem. C* 111 (2007) 7292.
270. D. Shi, W.D. Tennyson, J.C. Keay, E.S. Sanchez, M.B. Johnson, D.E. Resasco, *Chemical Physics Letters* 525 (2012) 82.
271. A. Monzon, G. Lolli, S. Cosma, S.A. Mohamed, D.E. Resasco. *J. Nanosci. Nanotech.* 8 (2008) 6141.
272. T. Thomson, S.L. Lee, M.F. Toney, C.D. Dewhurst, F.Y. Ogrin, C.J. Oates, S. Sun, *Phys. Rev. B.* 72 (2005) 064441.
273. W.E. Alvarez, F. Pompeo, J.E. Herrera, L. Balzano, D.E. Resasco, *Chemistry of Materials* 14 (2002) 1853.
274. Y. Li, W. Kim, Y. Zhang, M. Rolandi, D. Wang, H. Dai, *J. Phys. Chem. B* 105 (2001) 11424.
275. C. Cheung, A. Kurtz, H. Park, C.M. Lieber, *J. Phys. Chem. B* 106 (2002) 2429.
276. W. Kim, A. Javey, R. Tu, J. Cao, Q. Wang, H. Dai, *Appl. Phys. Lett.* 87 (2005) 173101.
277. M. Dressel, G. Gruner, *Electrodynamics of Solids: Optical Properties of Electrons in Matter*, Cambridge University Press, Cambridge, 2002.
278. Y. Xue, B. Wu, Y. Guo, L. Huang, L. Jiang, J. Chen, D Geng, Y Liu, W Hu, G Yu, *Nano Res.* 4 (2011) 1208.

-
279. Q. Cao, S.H. Hur, Z.T. Zhu, Y.G. Sun, C.J. Wang, M.A. Meitl, M. Shim, J.A. Rogers, *Adv. Mater.* 18 (2006) 304.
280. R. Jackson, S. Graham, *Appl. Phys. Lett.* 94 (2009) 012109.
281. Y. Huang, X. Duan, Y. Cui, C.M. Lieber, *Nano Lett.* 2 (2002) 101.
282. P. Beecher, P. Servati, A. Rozhin, A. Colli, V. Scardaci, S. Pisana, T. Hasan, A. J. Flewitt, J. Robertson, G.W. Hsieh, F.M. Li, A. Nathan, A.C. Ferrari, W.I. Milne, *Jour. Appl. Phys.* 102 043710 (2007).
283. T. Takenobu, N. Miura¹, S.Y. Lu, H. Okimoto, T. Asano, M. Shiraishi, Y. Iwasa, *Appl. Phys. Exp.* 2 025005 (2009).
284. H. Okimoto, T. Takenobu, K. Yanagi, Y. Miyata, H. Kataura, T. Asano, Y. Iwasa, *Jap. Jour. Appl. Phys.* 48 (2009) 06FF03.
285. C. Biswas, Y.H. Lee, *Adv. Funct. Mater.* 21 (2011) 3806.
286. A. Reina, X. Jia, J. Ho, D. Nezich, H. Son, V. Bulovic, M.S. Dresselhaus, J. Kong, *Nano Lett.* 9 (2009) 30 (2009).
287. C.C. Lu, Y.C. Lin, C.H. Yeh, J.C. Huang, P.W. Chiu, *ACS Nano* 6 (2012) 4469.
288. B.C. Huang, M. Zhang, Y. Wang, J. Woo, *Appl. Phys. Lett.* 99 (2011) 032107.
289. http://www.microchem.com/pdf/PMMA_Data_Sheet.pdf
290. J.H. Park, D.K. Hwang, J. Lee, S. Im, E. Kim, *Thin Solid Films* 515 (2007) 4041.
291. V. Derycke, R. Martel, J. Appenzeller, P. Avouris, *Nano Lett.* 1 (2001) 453.

Appendix A: Pd nanoclusters dispersed onto pristine and functionalized single-wall carbon nanotubes as a partial justification for the use of carbon nanotubes as catalyst supports.

This material was a joint effort with Teerawit Prasomsri that was originally published on Chemical Physics Letters 497 (2010) 103–107.

A.1 Abstract

The dispersion of Pd nanoclusters on single-wall carbon nanotubes (SWCNT) can be enhanced by creating defects on the nanotube walls, which lead to a stronger metal–support interaction. The ONIOM (DFT:MM) calculations show that the binding energy of Pd is significantly enhanced when the SWCNT surface is oxygen-functionalized, compared to the case of the pristine SWCNT surface. The electronic interaction of Pd atoms with oxygen at the defect sites results in a stronger bonding. These calculations are consistent with experimental measurements. Microscopy images clearly show that the functionalized SWCNT surface is much more effective than the pristine surface in anchoring Pd nanoclusters.

A.2 Introduction

Carbon nanotubes are being widely used as a support material for supporting metallic nanoparticles for applications in heterogeneous catalysis [1], fuel cells [2,3] and sensors [4–6]. Both multiband single-wall carbon nanotubes (MWCNT and SWCNT) have been found to be effective in stabilizing small metal clusters. Recently, we have developed a novel carbon nanotube–transition metal oxide hybrid (i.e. SWCNT/silica) that simultaneously stabilizes water/oil emulsions and catalyzes

reactions at the interface [7]. This nanohybrid behaves as a solid surfactant (half hydrophilic/half hydrophobic) and can selectively catalyze reactions at each side of the interface in biphasic liquid system such as bio-oils. The two-faced catalytic nanohybrid, so called ‘Janus catalyst’ [8] can be synthesized in such a way that a catalytic function is placed on the hydrophilic side and a different catalytic function on the hydrophobic side. For example, base-catalyzed condensation reactions can occur in the aqueous phase and metal-catalyzed hydrogenation on the organic phase. This combination is particularly relevant in the upgrading of bio-oils to biofuels [7]. It is therefore desirable to tailor the metal-anchoring ability of carbon nanotubes to maximize the dispersion and stability of nanoclusters on the surface of SWCNT by tuning the interaction between the metal clusters and the hydrophobic carbon support. It has been proposed that defect sites or functional groups on carbon nanotubes result in stronger metal–support interactions and consequently higher metal dispersion [9]. For instance, surface chemical modifications of MWCNTs by wet-chemical synthesis methods have been found to be the crucial in depositing Pt particles on MWCNTs [10]. Likewise, oxygen-functionalized sites can be created by acid [11,12] and plasma [9,13] treatments. In this contribution, we combine density functional theory (DFT) calculations and experimental preparations to compare the extent of Pd–nanotube interaction on pristine and oxidized SWCNT.

A.3 Experimental

The SWCNT used in the experimental preparations were synthesized by the CoMoCAT technique [14], and used in the purified form (pristine) or oxygen-

functionalized [15]. The functional groups were introduced by treating the SWCNT with HNO₃ 3M in reflux for 3 h. Following this treatment, the nanotubes were filtered through a vacuum filtration system and washed with an extensive amount of distilled water. The SWCNT collected on the filter paper were finally dried in a vacuum oven overnight at 80°C. For the deposition of Pd nanoclusters, the pristine and functionalized SWCNT were dispersed on two separate dishes, which were then placed together inside a sputtering coater chamber (Hummer VI Triode Sputter Coater). The samples were coated by sputtering at a current of 5 mA for 1 min. The pristine and functionalized SWCNT were characterized by Raman spectroscopy, by using a Jobin Yvon LabRam 600 single-grating spectrometer with a CCD detector instrument and excitation laser wavelength of 633 nm. For transmission electron microscopy (TEM) characterization, the samples were dispersed in isopropanol and sonicated by a horn sonicator (Cole-Parmer), operating at an amplitude of 25% for 10 min before deposition onto the TEM grids. Images were obtained on a JEOL 2000 system operating at an accelerating voltage of 200 kV.

A hybrid quantum mechanics/molecular mechanics (QM/MM) method was used to calculate the optimized structures and energies of the Pd nanoclusters on the pristine and functionalized single-wall carbon nanotubes (SWCNT). This technique has been extensively applied in previous SWCNT studies [16–20]. Two different structures, based on a 265-atom armchair (7, 7) SWCNT, were investigated. In both cases, each C-dangling bond at the edges was terminated with an O atom. In the structure containing a wall defect, the dangling bonds in the defect were also terminated with an O atom. The Pd/SWCNT structures were described at two levels of detail. The Pd₄ cluster and the

nanotube sites of interest (C13 for a perfect site; and C12O3 for a functionalized site) were treated at a higher level. The exchange–correlation hybrid functional B3LYP (Becke, three-parameter, Lee–Yang–Parr) [21–23] with the LANL2DZ (Los Alamos effective core potential) [24,25] was employed to describe the Pd₄ cluster. The 3-21+G(d) basis set [22,23,26] was applied in the case of SWCNT sites. The remaining part of the SWCNT was defined as the lower layer and treated by the universal force field (UFF) [27,28]. The position of atoms in this layer was kept frozen, while the Pd₄ clusters were left free to move to the energetically most favored position [29]. The binding energies between the Pd₄ cluster and SWCNT were computed using the expression:

$$E_b = E_T (\text{Pd}_4/\text{SWCNT}) - E_T (\text{Pd}_4) - E_T (\text{SWCNT})$$

where $E_T (\text{Pd}_4)$ and $E_T (\text{SWCNT})$ are total energies of a free standing Pd cluster and a bare SWCNT, respectively; and $E_T (\text{Pd}_4/\text{SWCNT})$ is the total energy for the optimized configuration with Pd₄ cluster adsorbed on the nanotube. All calculations based on density functional theory (DFT) were performed by using the GAUSSIAN-03 program suit [30].

A.4 Results and discussion

A.4.1 Deposition of Pd on pristine and functionalized CNTs

Oxidization by nitric acid has proven to be a convenient way for grafting oxygenated functional groups, without causing a significant structural damage to the nanotube [15,31,32]. As seen in the Raman spectra (Figure A-1), the sample treated in nitric acid showed a D band at $\sim 1300 \text{ cm}^{-1}$, which is somewhat broader and more

intense than that of the pristine sample, which indicates an increase in the amount of functionalized sites on SWCNT [33], but not large enough to compromise the nature of the nanotubes. In addition, it is observed that the Raman peaks of the functionalized SWCNT have been up-shifted in comparison to the pristine sample. These shifts have been previously attributed to lattice strains incorporated in the nanotube by the presence of the functional groups. The extent of deposition of Pd on the pristine and functionalized nanotubes was measured by treating the two types of substrates under identical Pd vapor exposure conditions (identical sputtering time, position, and current). If different metal distributions are observed, they can only be due to different degrees of Pd–SWCNT interactions. An effective anchoring of Pd atoms from the vapor phase onto the surface would result in a higher concentration of clusters on the surface. By contrast, a weak interaction would not generate nucleation sites for condensation and the deposition would not occur in a selective manner. Indeed, a dramatic difference was observed in the degree of Pd deposition on the two nanotube samples. The effect of the functional groups is evident in the TEM images of Figure A-2, with the functionalized SWCNT (Fig. A-2a) and the pristine SWCNT (Fig. A-2b), which can be compared to the corresponding nanotubes before addition of Pd (Fig. A-2c and d, respectively). The strength of the Pd–SWCNT interaction can also be illustrated by the resistance to the mechanical sonication that both samples are subject before the TEM measurement. Since both samples were sonicated at the same power and for the same amount of time, only those clusters that are effectively attached to the surface remain, while clusters only loosely deposited are ‘shaken off’ during sonication and left in the solvent.

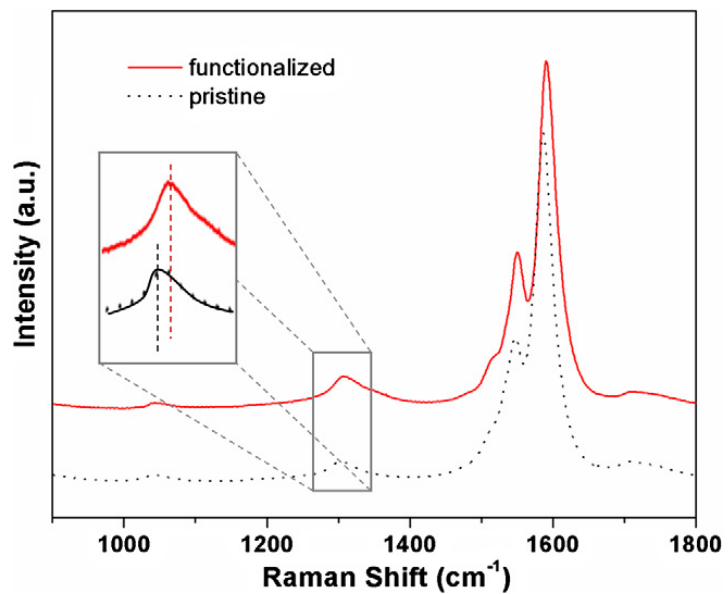


Figure A-1 Raman spectra of pristine (dashed black line) and functionalized (red solid line) SWCNTs. Spectra are normalized with respect to the G-band and shifted vertically for clarity.

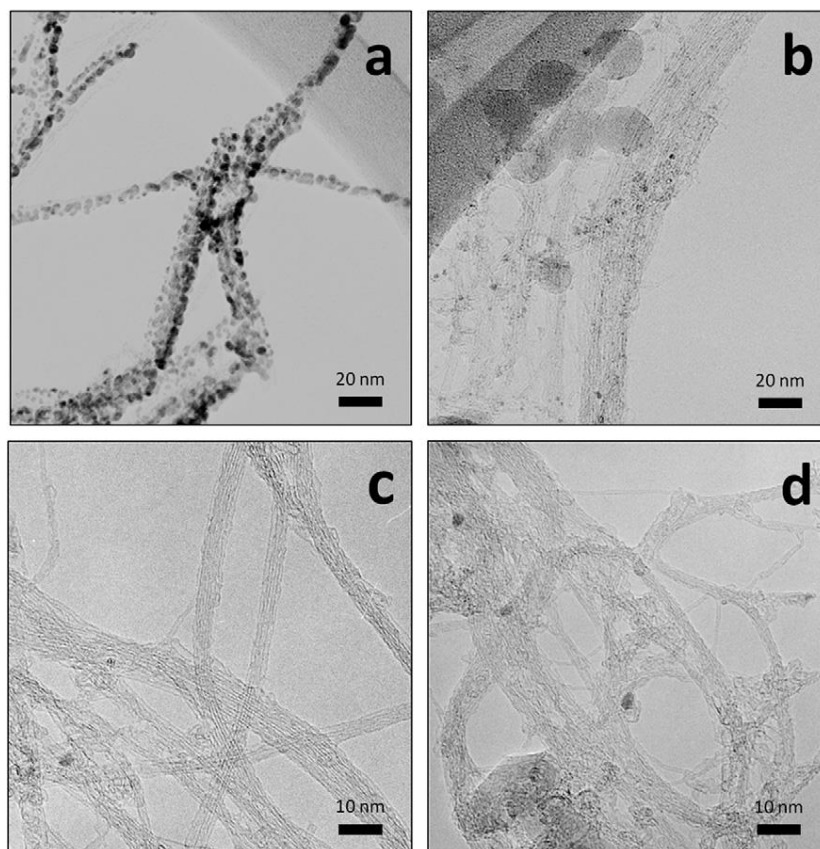


Figure A-2 TEM images of (a) Pd nanoclusters dispersed on functionalized; and (b) pristine SWCNTs. The corresponding SWCNTs before Pd deposition are shown as reference in (c) and (d), respectively.

A.4.2 DFT calculation for Pd₄ adsorption on the pristine and functionalized SWCNT

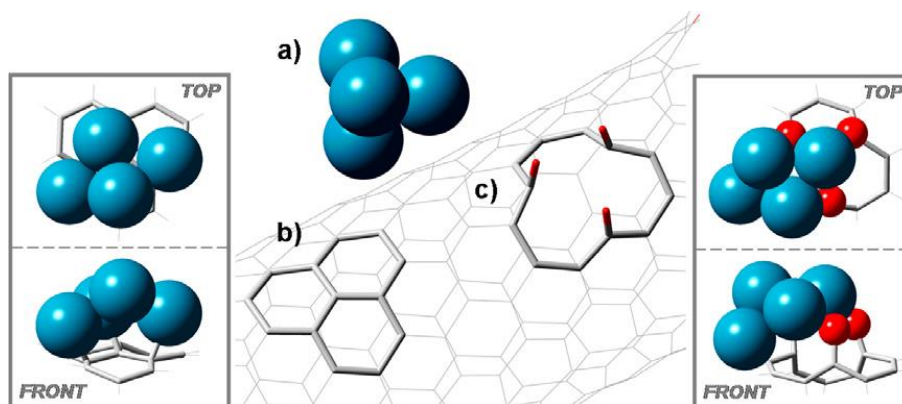


Figure A-3 The structure models for (a) a Pd₄ cluster alone; (b) a perfect site (C13); and (c) a functionalized site (C12O3) on the SWCNT. The corresponding adsorptions of Pd₄ on their sites are shown in boxes.

To simulate the adsorption of a metallic Pd cluster on a SWCNT, a Pd₄ model with envelop-like C_{2v} symmetry was chosen as the representative cluster in this study, as shown in Figure A-3. First, the isolated Pd₄ cluster was energetically optimized at triplet spin multiplicity, since the most stable cluster is obtained for the d⁸ electronic configuration of the metal valence electrons [18,34,35]. Then, the combined Pd₄/SWCNT systems were calculated, but unlike the calculation of the isolated Pd₄ cluster, the Pd₄/SWCNT systems were optimized at the lowest possible multiplicity [17,18]. The SWCNT with the functionalized site that acted as the anchoring place for adsorption was optimized from an initial structure, which had a typical C–C bond length ~1.41 Å and a nanotube diameter of 1 nm. In the optimized structure we observed a slight extension of the C–C bonds (i.e. 1.42–1.44 Å) around the functionalized site, due to the presence of O atoms. The adsorption models of Pd₄ clusters on the pristine and functionalized SWCNT were investigated over the perfect and the oxidized defective sites, respectively. The corresponding optimized geometries are shown in Table A-1. It

is worth noting that the structure of the two resulting Pd₄ clusters is distorted due to the interaction with the support. More specifically, this distortion results from the hybridization of the d orbital of the Pd atoms with the s and p orbitals of the adjacent C atoms [35,36]. The final Pd–C bond distance is ~1.94–2.11 Å, which is slightly shorter than that reported for a larger cluster (Pd₉) deposited on a nanotube [18]. The results on the functionalized SWCNT show some interesting differences. Unlike the pure covalent bonding obtained for the Pd₄/SWCNT_{pristine} system, deposition of Pd on the functionalized site (Pd₄/SWCNT_{func.}) involves a stronger type of interaction. The calculated Pd–O bond length is in the range 1.95–2.12 Å, which agree well with the results from X-ray diffraction (XRD) and extended X-ray absorption fine structure (EXAFS) measurements [37,38]. Formation of oxidized Pd species has been suggested from an X-ray photoelectron spectroscopy (XPS) study of Pd nanoparticles supported on oxygen plasma-treated MWCNT [9]. The calculated energies for the adsorption of Pd₄ on the pristine and functionalized sites are also remarkable different and in line with the type of interactions just described. The binding energy of 2.56 eV for Pd adsorption on the pristine site is similar to that previously calculated [28]. However, the adsorption on the functionalized site increases by more than 70%, to 4.62 eV. This remarkable enhancement in adsorption energy can be ascribed to the modification of the electronic structures of the resulting cluster. For instance, the energy difference between the highest occupied molecular orbital (HOMO) and the lowest unoccupied molecular orbital (LUMO) can be taken as a good indicator of changes in electronic properties and chemical reactivity [39]. We have calculated the HOMO–LUMO energy gap for the pristine and functionalized sites before the adsorption of Pd.

A significant difference was observed between the two cases. The energy gap for the pristine structure is 1.14 eV, which is consistent with previous results [40,41]. It is well known that the energy gap depends on diameter, chirality and even length of the nanotubes [42–45]. For instance, no HOMO–LUMO gaps can be expected from metallic nanotubes of infinite-length. However, in this case, we have only compared the changes in energy gaps caused by the presence of the oxygen atoms in the defect, keeping the other structural parameters constant. These calculations indicate that the presence of oxygen atoms at the functionalized site reduce the HOMO–LUMO gap to 0.82 eV. This reduction can be explained by the higher density of states near the Fermi level, arising from the overlap of the 2p electrons of the O atoms and the p electron system of the nanotube. This phenomenon does not happen in the case of a pristine carbon nanotube, which does not contain functional groups [46,47]. A smaller HOMO–LUMO gap should result in an easier excitation of electrons from the low-lying occupied levels to the upper empty level, which in turn enhances the chemical reactivity towards an adsorbate. That is, the functionalized site with the HOMO–LUMO gap modified by oxygen atom (i.e. a smaller gap) may be responsible for a stronger Pd4/SWCNT_{func.} interaction. Moreover, the HOMO–LUMO gaps of both types of sites decreased upon the adsorption of the Pd cluster (i.e. it was reduced to 0.92 and 0.54 eV for Pd4/SWCNT pristine and Pd4/SWCNT_{func.}, respectively). A similar extent of partial charge transfer, about 0.57–0.60 eV, was observed in both cases, which can be ascribed to the electronic reorganization caused by the interaction of the SWCNT and a high work function metal such as Pd [48,49]. That is, the presence of the 4d electrons of Pd

in the antibonding orbitals of the nanotube leads to an enhancement of the electron density in the nanotube, and, consequently, a smaller energy gap [50].

Table A-1 Pd–Pd, Pd–C and C–O bond lengths of a C_{2v} Pd₄ cluster alone, and the adsorptions of Pd₄ clusters on SWCNTs

Isolated Pd ₄		Pd ₄ /SWNT _{pristine}		Pd ₄ /SWNT _{func}	
Bond	Length (Å)	Bond	Length (Å)	Bond	Length (Å)
Pd1–Pd2	2.58	Pd1–Pd2	2.80	Pd1–Pd2	2.73
Pd1–Pd3	2.84	Pd1–Pd3	2.65	Pd1–Pd3	2.70
Pd1–Pd4	2.58	Pd1–Pd4	2.80	Pd1–Pd4	2.63
Pd2–Pd3	2.58	Pd2–Pd3	2.86	Pd2–Pd3	2.71
Pd3–Pd4	2.58	Pd3–Pd4	2.90	Pd3–Pd4	2.80
		Pd2–C1	2.10	Pd3–O1	1.95
		Pd1–C2	2.11	Pd1–O2	2.12
		Pd4–C3	1.94	Pd4–O3	2.06
				C1–O1	1.42
				C2–O2	1.42
				C3–O3	1.37

A.5 Conclusion

The combination of experimental measurements and DFT calculations of binding energies suggests that the Pd nanoclusters are much more effectively anchored on functionalized than on the pristine SWCNT. The modification of the electronic structure caused by the presence of oxygen atoms is responsible for the enhanced adsorption energy, leads to the formation of Pd–O bonds on the functionalized SWCNT.

Appendix B. The use of activated carbon as catalyst support in aqueous-phase ketonization of acetic acid

This materials is part of a joint effort with Tu N. Pham that was originally published on Journal of Catalysis 295 (2012) 169–178.

B.1 Brief introduction of this work

The ketonization of acetic acid over Ru/TiO₂ and Ru/TiO₂/C catalysts has been accomplished in the liquid phase at temperatures significantly lower than those typically needed for this reaction. The catalysts were prepared by impregnating the activated carbon support with titanium(IV) isopropoxide, followed by slow hydrolysis and calcination in the absence of air. The resulting TiO₂/C powder was further impregnated with Ru(III) chloride, dried, and calcined in air. After an in situ pre-reduction in H₂, the resulting Ru/TiO₂/C exhibited high activity and selectivity to acetone in both organic and aqueous phases at 180°C. By contrast, when the TiO₂/C sample was pre-calcined in air before the addition of Ru, the resulting catalyst showed significantly lower activity, even when it was pre-reduced in situ, and was essentially inactive without pre-reduction. It is believed that surface Ti³⁺ species can be readily formed and favor the ketonization reaction in the presence of liquid water. A combination of techniques including TEM, BET, TPR, XRD, XPS, and EPR was used to characterize the reducibility of the catalysts as well as the formation of and stability of Ti³⁺ sites. It is proposed that the presence of Ru on TiO₂ facilitates the formation of these reduced sites. Furthermore, the hydrophobicity of the carbon support is believed to slow down the typical inhibiting effect of water for reactions catalyzed by reduced Ti³⁺ sites.

B.2 The role of activated carbon as catalyst support

As shown in Figure B-1, the catalytic ketonization activity of Ru/TiO₂/C in water phase is kept much longer than that of Ru/TiO₂. For example, between 2 and 4 h of reaction time, the conversion over Ru/TiO₂ remained unchanged, indicating that the catalyst was no longer active. During the same period of time, the conversion over the Ru/TiO₂/C catalyst increased by more than 50%. That is, the presence of activated carbon seems to improve the tolerance of the catalyst to water, slowing down its deactivation. The special role played by the carbon support in water is further evidenced when we compare the behavior observed when n-hexane was used as a solvent (Figure B-1b). In n-hexane medium, where the effect of water was missing, the Ru/TiO₂ catalyst did not deactivate as fast, and the behavior of the carbon-supported catalyst was not much different from that of the Ru/TiO₂ catalyst. For instance, during the same period of reaction time, 2–4 h, the conversion increased by about 50% on both catalysts. As reported in earlier studies, activated carbon, possessing high porosity and surface area, has been the most widely and effectively used adsorbent for adsorption of organic molecules from aqueous solutions [51-56]. In our case, it is possible that hydrophobic porous structure of the activated carbon may impede the effective wetting of the surface, which may become saturated with organic species, thus preventing the irreversible deactivation by water.

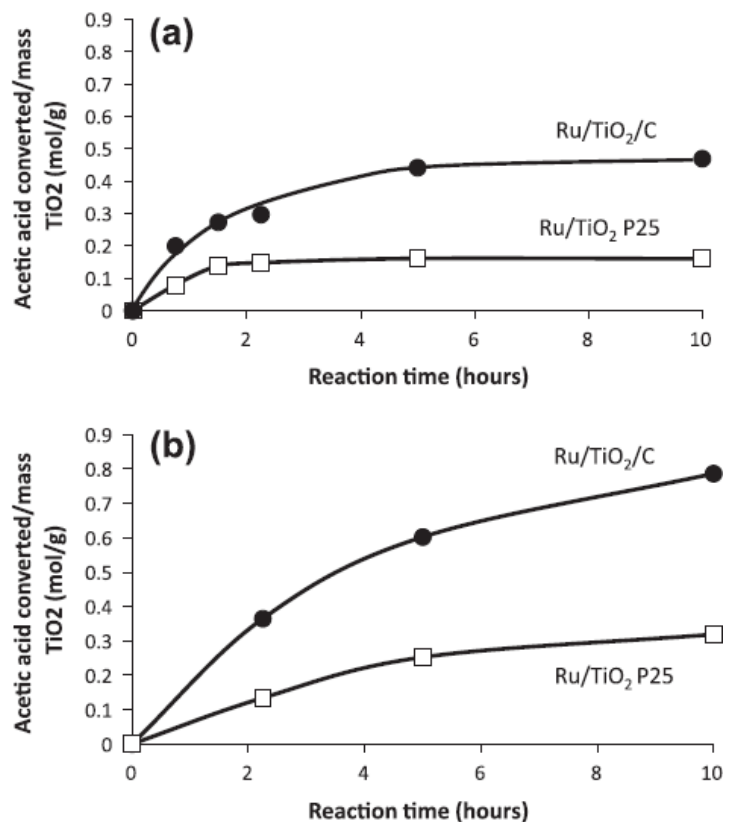


Figure B-1 Catalytic activity of Ru/TiO₂ P25 and Ru/TiO₂/C catalysts for the reactions at 180°C as a function of reaction time in water phase (a) and n-hexane (b). All the catalysts were pre-reduced in 400 psi H₂ at 250°C for 3 h before reaction.

Appendix C. Calculation and fitting in Chapter 1

Fitting product distribution with Anderson-Shulz-Flory (ASF) equation

$$\text{ASF equation: } W_n = n(1 - \alpha)^2 \alpha^{n-1},$$

Where n is carbon number, W_n is weight fraction, and $\alpha = \frac{R_p}{R_p + R_t}$, is the chain growth probability.

The equation was fitted to liquid phase products ($n \geq 5$). Gas phase products were predominated by methane due to the reasons stated in the main context and therefore didn't follow ASF equation tightly. The fitting gave a gas phase weight fraction of 17.8%, in close agreement with the actual fraction of 18.2%. α was 84.3% according to the fitting and it falls in the typical value range for Ru catalyst.

Calculation of catalyst activity and TOF

For the reaction with $H_2/CO = 3.5$ whose results are shown in Figure 3:

$$\text{Initial CO amount} = 22\% \times 600 \text{ psi (initial total pressure)} = 132 \text{ psi} = 0.026 \text{ moles}$$

$$\text{Final CO amount} = 2.09\% \times 250 \text{ psi (final total pressure)} = 5.23 \text{ psi} = 0.001 \text{ moles}$$

$$\text{Ru amount} = \frac{0.2 \text{ g (total mass of catalyst)} \times 3.7\%}{\frac{101.07 \text{ g}}{\text{mol}}} = 7.32 \times 10^{-5} \text{ mol}$$

$$\text{Activity} = \frac{0.026 \text{ mol} - 0.001 \text{ mol}}{12 \text{ h} \times 7.32 \times 10^{-5} \text{ mol}} = 28.1 \text{ mol}(\text{mol Ru})^{-1} \text{h}^{-1}$$

Based on TEM, mean size of Ru particles was 4nm. Assuming spherical shape and using equation dispersion = 1.32/d (nm) (J. Álvarez-Rodríguez, A. Guerrero-Ruiz, I. Rodríguez-Ramos, A. Arcoya-Martín, Catal. Today 2005, 107, 302), dispersion was calculated to be 0.33.

The pressure drop during the first hour was about 60 psi at 200°C. Assuming syngas was reacting at a ratio of H₂/CO = 2, corresponding to CO pressure drop of 20 psi, which was about 2.45 x 10⁻³ mol according to simple ideal gas law.

$$\text{TOF} = \frac{2.45 \times 10^{-3} \text{ mol}}{0.33 \times 7.32 \times 10^{-5} \text{ mol} \times 3600} = 28.2 \times 10^{-3} \text{ s}^{-1}$$

Carbon balance was 82.8%.

For the reaction with H₂/CO = 3.5 whose results are shown in Figure 4:

Initial CO amount = 22% x 600 psi (initial total pressure) = 132 psi = 0.026 moles

Final CO amount = 5.9% x 275 psi (final total pressure) = 16.3 psi = 0.003 moles

$$\text{Ru amount} = \frac{0.15 \text{ g (total mass of catalyst)} \times 3.5\%}{\frac{101.07 \text{ g}}{\text{mol}}} = 5.19 \times 10^{-5} \text{ mol}$$

$$\text{Activity} = \frac{0.026 \text{ mol} - 0.003 \text{ mol}}{6 \text{ h} \times 5.19 \times 10^{-5} \text{ mol}} = 73.9 \text{ mol}(\text{mol Ru})^{-1} \text{h}^{-1}$$

Carbon balance was 95.5%.

Based on TEM, mean size of Ru particles was 1.5 nm. Again, assuming spherical shape and using dispersion = 1.32/d (nm) dispersion was calculated to be 0.88.

The pressure drop during the first hour was about 60 psi at 200°C. Assuming syngas was reacting at a ratio of H₂/CO = 2, corresponding to CO pressure drop of 20 psi, which was about 2.45 x 10⁻³ mol according to simple ideal gas law.

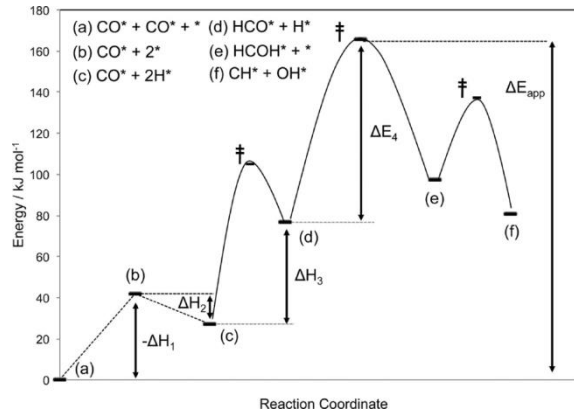
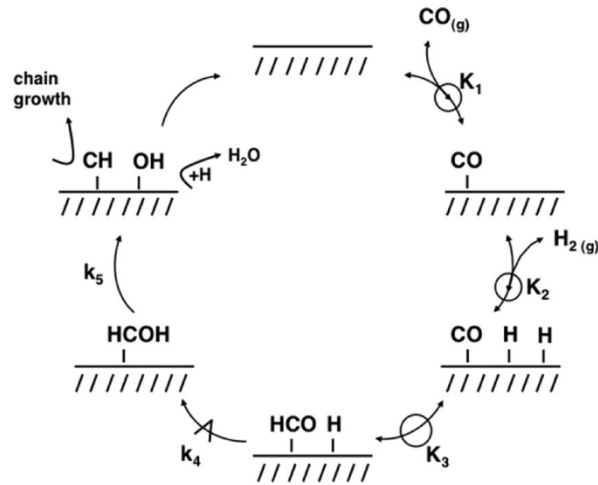
$$\text{TOF} = \frac{2.45 \times 10^{-3} \text{ mol}}{0.88 \times 5.19 \times 10^{-5} \text{ mol} \times 3600} = 14.9 \times 10^{-3} \text{ s}^{-1}$$

Calculation of water vapor during reduction and reaction steps

According to Antoine Equation: $\log_{10}P = A - \frac{B}{C+T}$, where $A = 8.14019$, $B = 1810.94$, $C = 244.485$, $T = 250 \text{ }^\circ\text{C}$ (reduction) and $200 \text{ }^\circ\text{C}$ (reaction), we get $P = 30053.84 \text{ mmHg} = 581 \text{ psi}$ for reduction, and $11639.83 \text{ mmHg} = 225 \text{ psi}$ for reaction.

A rough estimate according to ideal gas law showed that about 0.065 and 0.028 mol of water was needed to sustain these saturation vapor pressures, which was only 8% and 3% of the water present in the vessel during reduction and reaction, respectively.

Appendix D. Kinetic fitting of FTS in water and emulsion phases



Elementary steps of H-assisted FTS (top) and its energy diagram (bottom). Kinetics expression:

$$r_{\text{CO}} = \frac{K_2 K_3 k_4 P_{\text{H}_2}}{K_1 P_{\text{CO}}} = \delta \frac{P_{\text{H}_2}}{P_{\text{CO}}}$$

with

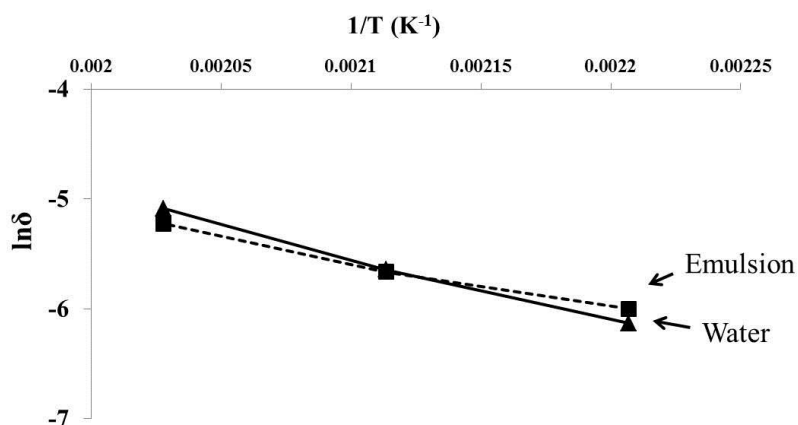
$$\delta = A \exp\left(\frac{-\Delta E_{\text{app}}}{RT}\right)$$

$$= A \exp\left(\frac{-\left(\Delta H_2 + \Delta H_3 + \Delta E_4 - \Delta H_1\right)}{RT}\right)$$

(adapted from Reference 52).

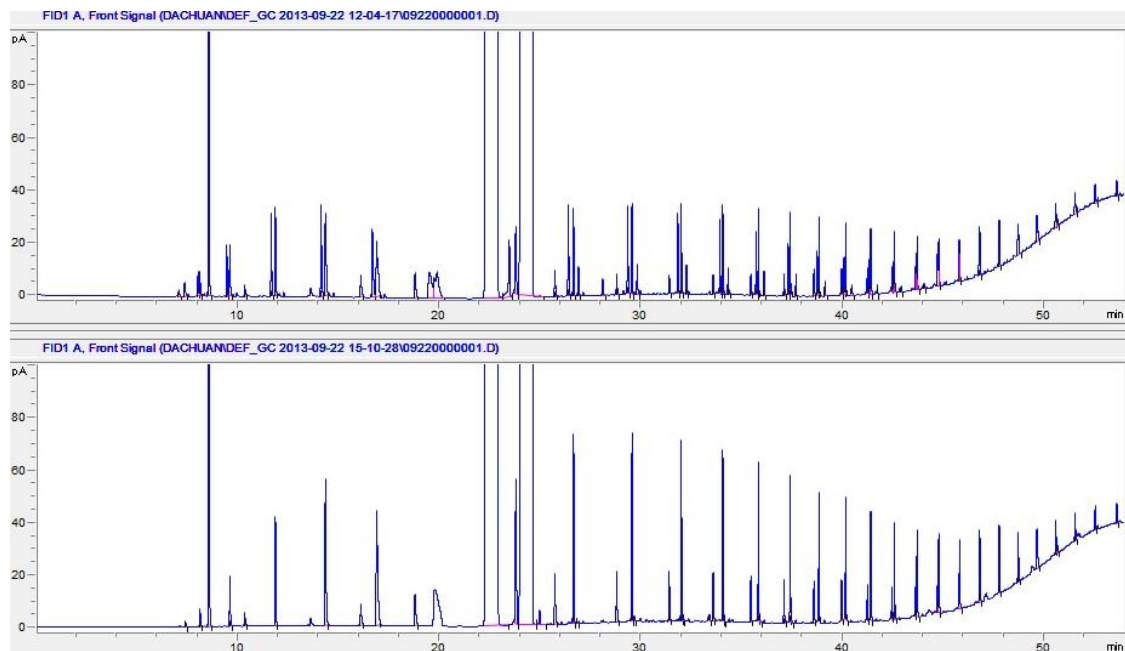
CO conversion rate ($\times 10^{-3}$ mole/h) (excluding WGS)

Temperature \ Solvent	180°C	200°C	220°C
Water	2.20	3.09	4.79
Emulsion	1.93	3.15	5.59

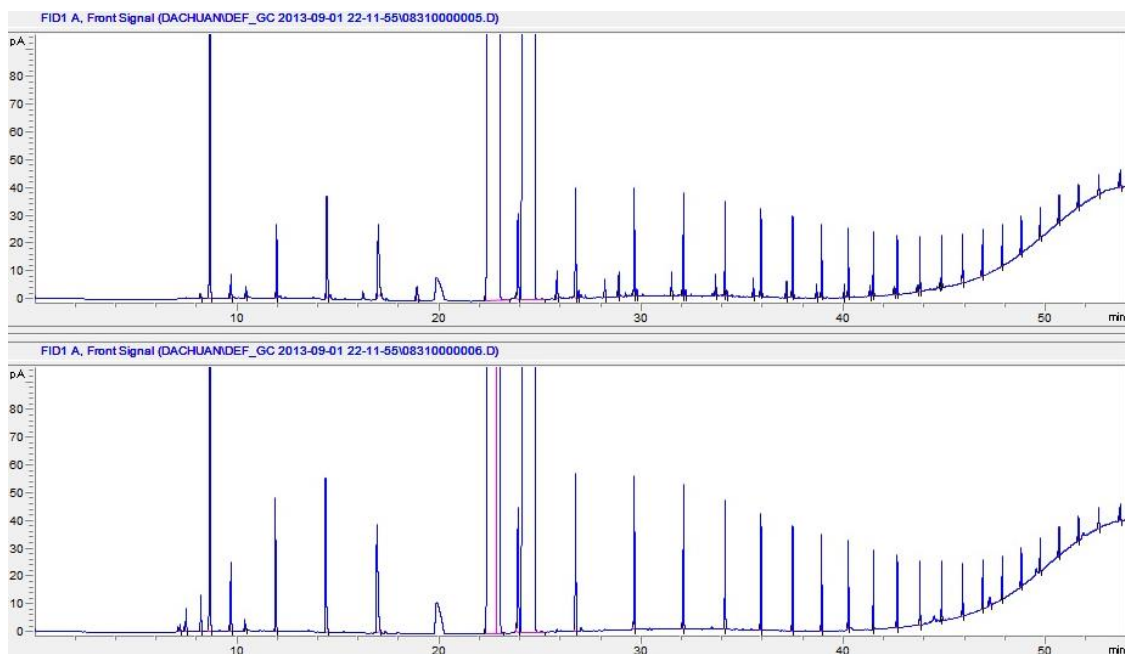


Arrhenius plots of FTS at 180°C, 200°C and 220°C in water and emulsion phases. Reaction was carried out with 50 mg catalyst at 600 psi syngas ($H_2/CO = 3.5$) for 1h, which led to conversion of 8% ~ 24%. Apparent activation energy for water single-phase was calculated to be 35.96 kJ/mol and 48.46 kJ/mol for emulsion, respectively. Constant H_2 and CO partial pressure and absence of mass transfer limitation were assumed.

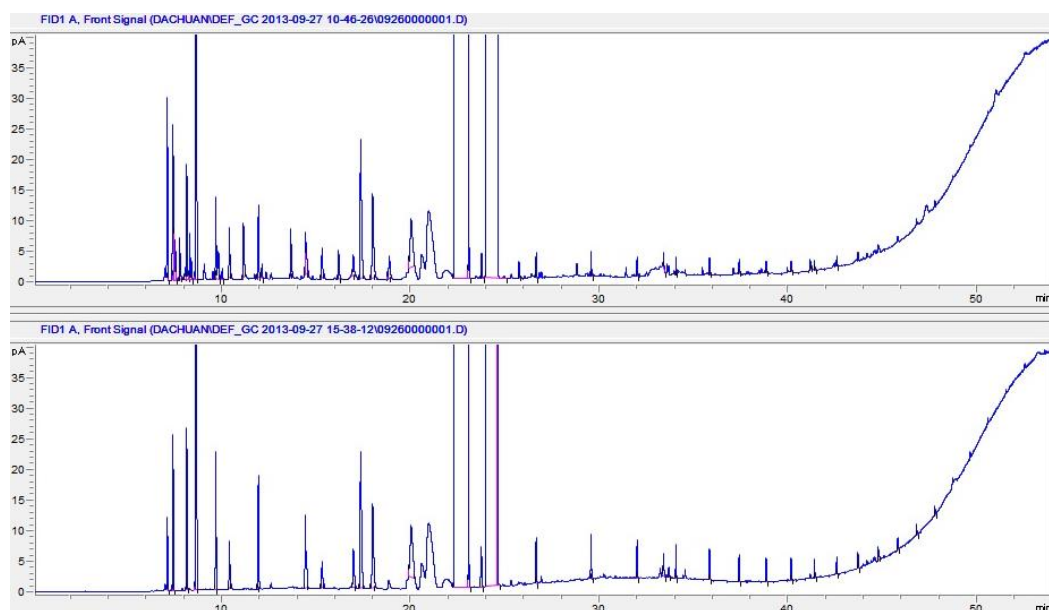
Appendix E. GC chromatographs



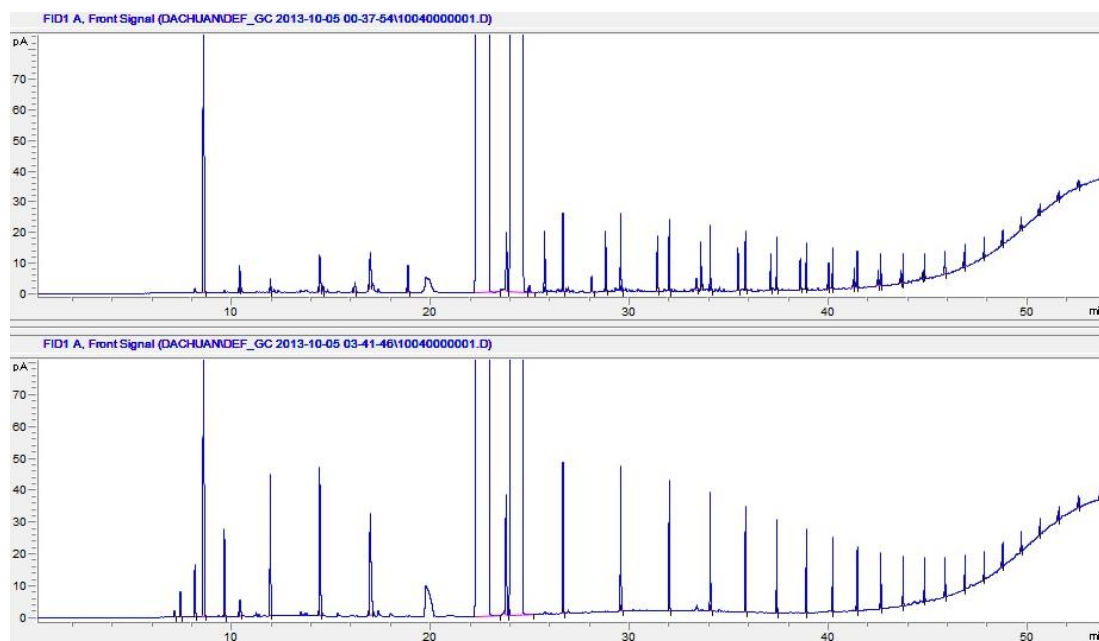
GC chromatographs of products from FTS with silica-supported catalyst in water single-phase at a conversion of 80.2% before (a) and after (b) hydrogenation.



GC chromatographs of products from FTS with nanohybrid-supported catalyst in water single-phase at a conversion of 84.8% before (a) and after (b) hydrogenation.



GC chromatographs of products from FTS with silica-supported catalyst in decalin single-phase at a conversion of 33.5% before (a) and after (b) hydrogenation.



GC chromatographs of products from FTS with carbon-supported catalyst in water single-phase at a conversion of 38.7% before (a) and after (b) hydrogenation.

Appendix F. Optoelectronic performance of CNT films reported in the literature

Process	R_s (Ω/sq)	T%	Reference
Liquid-liquid interface	20000	97%	[59]
Air brush	1000	90%	[60]
Mayer rod or draw- down rod	700/300*	90%	[61]
Filter	1100	88%	[62]
Layer by layer	1620	85%	[63]
Layer by layer	1100	85%	[64]
Air brush	956/472*	85%	[65]
Roll-to-roll	24	83.4%	[66]
Ultrasonic spray	70	81%	[67]
Dip or spray coating	332	80%	[68]
Spray coating	150/80*	80%	[69]
Filter/stamp	150	80%	[70]
Spin-coating	100	80%	[71]
Vacuum filtration	1000/220*	79%	[72]
Vacuum filtration	1300/231**	75%	[73]

* After acid treatment **With sorted metallic SWCNTs

Appendix G. References for Appendix

- [1] P. Serp, M. Corrias, P. Kalck, *Appl. Catal. A-Gen.* 253 (2003) 337.
- [2] J.S. Ye, H.F. Cui, Y. Wen, W.D. Zhang, G.Q. Xu, F.S. Sheu, *Microchim. Acta* 152 (2006) 267.
- [3] G.P. Jin, Y.F. Ding, P.P. Zheng, *J. Power Sources* 166 (2007) 80.
- [4] Z. Siwy, L. Trofin, P. Kohli, L.A. Baker, C. Trautmann, C.R. Martin, *J. Am. Chem. Soc.* 127 (2005) 5000.
- [5] J. Kong, M. Chapline, H. Dai, *Adv. Mater.* 13 (2001) 1384.
- [6] S. Yu, U. Welp, L.Z. Hua, A. Rydh, W.K. Kwok, H. Hau Wang, *Chem. Mater.* 17 (2005) 3445.
- [7] S. Crossley, J. Faria, M. Shen, D.E. Resasco, *Science* 327 (2010) 68.
- [8] D.J. Cole-Hamilton, *Science* 324 (2010) 41.
- [9] A. Felten et al., *Micron* 40 (2009) 74.
- [10] W. Li, C. Liang, W. Zhou, J. Qiu, Z. Zhou, G. Sun, Q. Xin, *J. Phys. Chem. B* 107 (2003) 6292.
- [11] J.P. Singh, X.G. Zhang, Hu-lin Li, A. Singh, R.N. Singh, *Int. J. Electrochem. Sci.* 3 (2008) 416.
- [12] B.C. Satishkumary, E.M. Voglz, A. Govindarajx, C.N.R. Raoyzx, *J. Phys. D: Appl. Phys.* 29 (2009) 3173.
- [13] C. Bittencourt et al., *Surf. Sci.* 601 (2007) 2800.
- [14] D.E. Resasco, W.E. Alvarez, F. Pompeo, L. Balzano, J.E. Herrera, B. Kitiyanan, A. Borgna, *J. Nanoparticle Res.* 4 (2002) 131.
- [15] M.N. Tchoul, W.T. Ford, G. Lolli, D.E. Resasco, S. Arepalli, *Chem. Mater.* 19

- (2007) 5765.
- [16] V. D'Anna, D. Duca, F. Ferrante, G. La Manna, *Phys. Chem. Chem. Phys.* 11 (2009) 4077.
- [17] V. D'Anna, D. Duca, F. Ferrante, G. La Manna, *Phys. Chem. Chem. Phys.* 12 (2010) 1323.
- [18] D. Duca, F. Ferrante, G. La Manna, *J. Phys. Chem. C* 111 (2007) 5402.
- [19] S. Dapprich, I. Komáromi, K.S. Byun, K. Morokuma, M.J. Frisch, *J. Mol. Struct. Theochem.* 461–462 (1999) 1.
- [20] M. Svensson, S. Humbel, R.D.J. Froese, T. Matsubara, S. Sieber, K. Morokuma, *J. Phys. Chem.* 100 (1996) 19357.
- [21] A.D. Becke, *J. Chem. Phys.* 98 (1993) 1372.
- [22] P.J. Stephens, J.F. Devlin, C.F. Chabalowsky, M.J. Frisch, *J. Phys. Chem.* 98 (1994) 11623.
- [23] C. Lee, W. Yang, R.G. Parr, *Phys. Rev. B: Condens. Matter* 37 (1988) 785.
- [24] P.J. Hay, W.R. Wadt, *J. Chem. Phys.* 82 (1985) 270.
- [25] P.J. Hay, W.R. Wadt, *J. Chem. Phys.* 82 (1985) 299.
- [26] A.D.J. Becke, *Chem. Phys.* 98 (1993) 5648.
- [27] A.K. Rappè, C.J. Casewit, K.S. Colwell, W.A. Goddard, W.M. Skiff, *J. Am. Chem. Soc.* 114 (1992) 10024.
- [28] A.K. Rappè, K.S. Colwell, C.J. Casewit, *Inorg. Chem.* 32 (1993) 3428.
- [29] N. Armata et al., *Top. Catal.* 52 (2009) 444.
- [30] M.J. Frisch et al., *GAUSSIAN 03*, GAUSSIAN, Inc., Wallingford, CT, 2004.
- [31] J. Chen, M.A. Hamon, H. Hu, Y. Chen, A.M. Rao, P.C. Eklund, R.C. Haddon

- Science 282 (1998) 95.
- [32] K.A. Worsley, I. Kalinina, E. Bekyarova, R.C. Haddon, J. Am. Chem. Soc. 131 (2009) 18153.
- [33] U.J. Kim, C.A. Furtado, X. Liu, G. Chen, P.C. Eklund, J. Am. Chem. Soc. 127 (2005) 15437.
- [34] C.D. Zeinalipour-Yazdi, A.L. Cooksy, A.M. Efstathiou, Surf. Sci. 602 (2008) 1858.
- [35] A. Maiti, A. Ricca, Chem. Phys. Lett. 395 (2004) 7.
- [36] D.H. Chi et al., Chem. Phys. Lett. 432 (2006) 213.
- [37] S.-J. Kim, S. Lemaux, G. Demazeau, J.-Y. Kim, J.-H. Choy, J. Am. Chem. Soc. 123 (2001) 10413.
- [38] W.B. Li et al., Phys. Scr. T115 (2005) 749.
- [39] K. Fukui, Science 218 (1982) 747.
- [40] M. Baldoni, A. Sgamellotti, F. Mercuri, Org. Lett. 9 (2007) 4267.
- [41] F. Buonocore, F. Trani, D. Ninno, A. Di Matteo, G. Cantele, G. Iadonisi, Nanotechnology 19 (2008) 025711.
- [42] B. Shan, K. Cho, Phys. Rev. Lett. 94 (2005) 236602.
- [43] C.W. Chen, M.H. Lee, Nanotechnology 15 (2004) 480.
- [44] W.S. Su, T.C. Leung, B. Li, C.T. Chan, Appl. Phys. Lett. 90 (2007) 163103.
- [45] B.K. Agrawal, S. Agrawal, R. Srivastava, J. Phys.: Condens. Matter 15 (2003) 6931.
- [46] G. Zhang, W. Duan, G. Zhou, B. Gu, Solid State Commun. 122 (2002) 121.
- [47] H. Zheng, W. Duley, Phys. Rev. B 78 (2008) 045421.

- [48] M. Penza, R. Rossi, M. Alvisi, G. Cassano, M.A. Signore, E. Serra, R. Giorgi, *Sensor. Actuat. B-Chem.* 135 (2008) 289.
- [49] P. Pannopard, P. Khongpracha, M. Probst, J. Limtrakul, *J. Mol. Graph. Model.* 28 (2009) 62.
- [50] P. Tarakeshwar, D.M. Kim, *J. Phys. Chem. B* 109 (2005) 7601.
- [51] A. Shukla, Y.-H. Zhang, P. Dobey, J.L. Margrave, S.S. Shukla, *J. Hazard. Mater.* 95 (2002) 137.
- [52] S. Susarla, G.V. Bhaskar, S.M. Bhamidimarri, *Environ. Technol.* 14 (1993) 159.
- [53] Z. Aksu, E. Kabasakal, *Sep. Purif. Technol.* 35 (2004) 223.
- [54] D. Mohan, S. Chander, *Colloid Surf. A* 177 (2001) 183.
- [55] Z. Aksu, J. Yener, *J. Environ. Sci. Health – A* 34 (1999) 1277.
- [56] D.D. Mohan, V.K. Gupta, S.K. Srivastava, S. Chander, *Colloid Surf. A* 177 (2001) 169.
- [57] J. Álvarez-Rodríguez, A. Guerrero-Ruiz, I. Rodríguez-Ramos, A. Arcoya-Martín, *Catal. Today* 2005, 107, 302
- [58] *J. Am. Chem. Soc.* 2013, 135, 6107–6121
- [59] J. Matsui, K. Yamamoto, T. Miyashita, *Carbon* 47 (2009) 1444.
- [60] M. Kaempgen, G.S. Duesberg, S. Roth, *Appl. Surf. Sci.* 252 (2005) 425.
- [61] B. Dan, G.C. Irvin, M. Pasquali, *ACS Nano* 3 (2009) 835.
- [62] Y. Wang, C. Di, Y. Liu, H. Kajiura, S. Ye, L. Cao, D. Wei, H. Zhang, Y. Li, K. Noda, *Adv. Mater.* 20 (2008) 4442. Also see reference [9] in main text.
- [63] Y.T. Park, A.Y. Ham, J. C. Grunlan, *J. Phys. Chem. C* 114 (2010) 6325.

- [64] X. Yu, R. Rajamani, K.A. Stelson, T. Cui, Surf. and Coatings Tech. 202 (2008) 2002.
- [65] S. Paul, D. Kim, Carbon 47 (2009) 2436.
- [66] C. Feng, K. Liu, J. Wu, L. Liu, J. Cheng, Y. Zhang, Y. Sun, Q. Li, S. Fan, K. Jiang, Adv. Func. Mater. 20 (2010) 885.
- [67] R.C. Tenent, T.M. Barnes, J.D. Bergeson, A.J. Ferguson, B. To, L.M. Gedvilas, M.J. Heben, J.L. Blackburn, Adv. Mater. 21 (2009) 3210.
- [68] S. Paul, Y.S. Kang, J. Yim, K.Y. Cho, D. Kim, Current Applied Physics 10 (2010)101.
- [69] H. Geng, K.K. Kim, K.P. So, Y.S. Lee, Y. Chang, Y.H. Lee, J. Am. Chem. Soc. 129 (2007) 7758. Also see reference [6] in main text.
- [70] Y. Zhou, L. Hu, G. Grüner, Appl. Phys. Lett. 88 (2006) 123109.
- [71] S. Manivannan, J.H. Ryu, J. Jang, C.K. Park, Jour. of Mater. Sci.: Mater. in Electronics. 21 (2010) 595.
- [72] B.B. Parekh, G. Fanchini, G. Eda, M. Chhowalla, Appl. Phys. Lett. 90 (2007) 21913.
- [73] A.A. Green, M.C. Hersam, Nano Lett. 8 2008 1417. Also see reference [5] in main text.